

Cédric Simenel

NUCLEAR QUANTUM MANY-BODY  
DYNAMICS:

*from collective vibrations to heavy-ion collisions*

**Habilitation à Dirriger des Recherches**

Université de Caen - Basse-Normandie

May 3<sup>rd</sup>, 2012

MEMBERS OF THE JURY

Pr.	<b>Francesca</b>	<b>Gulminelli</b>	LPC Caen	(Referee)
Pr.	<b>Joachim</b>	<b>Maruhn</b>	Frankfurt University	
Pr.	<b>Neil</b>	<b>Rowley</b>	IPN Orsay	(Referee)
Pr.	<b>François</b>	<b>Sébille</b>	SUBATECH	(President)
Pr.	<b>Eric</b>	<b>Suraud</b>	Université Paul Sabatier	(Referee)

# Content

<b>Introduction</b>	<b>1</b>
<b>1 Theoretical approach to nuclear quantum dynamics: the time-dependent Hartree-Fock theory and its extensions</b>	<b>5</b>
1.1 Introduction . . . . .	5
1.2 The Balian-Vénéroni variational principle . . . . .	7
1.3 Derivation of the time-dependent Hartree-Fock equation . . . . .	8
1.4 The Balian-Vénéroni prescription for fluctuations and correlations of one-body observables . . . . .	11
1.5 Numerical solution of the TDHF equation . . . . .	15
1.5.1 Numerical method . . . . .	15
1.5.2 The TDHF3D code . . . . .	16
1.6 Perspectives for beyond TDHF calculations . . . . .	20
<b>2 Collective vibrations</b>	<b>23</b>
2.1 Introduction . . . . .	23
2.2 Linear response theory . . . . .	25
2.3 Direct decay of giant resonances . . . . .	27
2.4 Anharmonicity of giant resonances . . . . .	31
2.5 Pairing dynamics . . . . .	34
2.5.1 The TDHFB theory . . . . .	35
2.5.2 Application to pairing vibrations . . . . .	36
2.6 Conclusions and perspectives . . . . .	38
<b>3 Heavy-ion collisions</b>	<b>40</b>
3.1 Motivations . . . . .	40
3.1.1 Unique perspectives brought by the nuclear case to study quantum phenomena . . . . .	41
3.1.2 Production of specific nuclear systems: case of the heaviest nuclei . . . . .	41

3.2	Fusion in medium mass systems . . . . .	44
3.2.1	Fusion of spherical nuclei: the example of the $^{16}\text{O}+^{208}\text{Pb}$ system . . . . .	44
3.2.2	Fusion barriers with a deformed nucleus . . . . .	50
3.2.3	Charge equilibration in fusion . . . . .	51
3.3	Transfer reactions . . . . .	54
3.4	Deep-Inelastic Collisions . . . . .	58
3.5	Fusion and quasi-fission in heavy systems . . . . .	62
3.5.1	TDHF calculations of fusion hindrance . . . . .	63
3.5.2	Search for fusion-evaporation events in the $^{124}\text{Sn}+^{136}\text{Xe}$ reaction . . . . .	64
3.5.3	Quasi-fission: interplay between shells and isospin . . . . .	65
3.5.4	TDHF calculations of the $^{40}\text{Ca}+^{238}\text{U}$ reaction . . . . .	69
3.6	Actinide collisions . . . . .	71
3.7	Conclusion and perspectives . . . . .	74
	<b>Conclusion</b>	<b>77</b>
	<b>A TDHF approach from the standard variational principle</b>	<b>79</b>
	<b>B Galilean invariance of the TDHF equation</b>	<b>82</b>
	B.1 Revisiting the Thouless-Valatin demonstration . . . . .	82
	B.2 Case of a full Skyrme field . . . . .	85
	<b>List of Publications</b>	<b>92</b>
	<b>Bibliography</b>	<b>109</b>

# Acknowledgements

First of all, I would like to thank the members of the jury panel of my Habilitation to Supervise Research:

- the president of the jury, François Sébille,
- the referees, Francesca Gulminelli, Neil Rowley, and Eric Suraud.
- the examiners, Joachim Maruhn and Francis Hanappe<sup>1</sup>.

In particular, I deeply thank Francesca for her help with administrative procedures at the University of Caen.

I thank the SPhN directors, N. Alamanos, M. Garçon and H. Goutte, as well as the SPhN deputy director, F. Auger, and the nuclear structure group leaders, R. Dayras and W. Korten for their constant support during all these years spent at Saclay.

Motivating long term collaborations on nuclear dynamics with Ph. Chomaz, D. Lacroix and B. Avez are acknowledged.

These studies would not have been possible without the work of P. Bonche, who is the main author of the TDHF3D code and was one of the principal contributors to this field.

An essential part of the work presented in this report as been carried out with the help of students without whom it would have been difficult, if not impossible, to investigate this field in deep details. B. Avez, C. Golabek, D. J. Kedziora and A. Wakhle are thanked for their important contributions.

Advances in nuclear dynamics strongly benefit from the work of nuclear structure theoreticians, and collaborations with M. Bender, K. Bennaceur, and T. Duguet are acknowledged.

Collaborations with experimentalists are crucial to this field. In particular, I would like to thank my colleagues from the nuclear structure group at Saclay: A. Corsi, A. Gillibert, W. Korten, V. Lapoux, A. Obertelli, E. Pollacco, M.-D. Salsac, B. Sulignano, Ch. Theisen, M. Zielinska. I would also like to thank M. Dasgupta and D. J. Hinde who gave me the opportunity to work with them at Canberra for 1.5 year. I am grateful to the "fusion boys" (M. Evers, D.-H. Luong, A. Wakhle, R. du Rietz, R. Rafiei...) for their warm welcome and motivating discussions.

This work would not have been possible without numerous scientific exchanges with both theoreticians and experimentalists. In particular, discussions with E. Ackad, G. Adamian, N. Antonenko, S. Ayik, Ch. Beck, A. Cole, S. Courtin, W.

---

<sup>1</sup>Francis Hanappe could not be present at the oral defense due to personal reasons.

Greiner, G. de France, F. Haas, Y. Iwata, D. Jacquet, J. Meyer, M. Morjean, V. de la Mota, A. Navin, F. Nunes, M.-G. Porquet, Ph. Quentin, M.-D. Salsac, P. Schuck, S. Umar, P.D. Stevenson, M. Vénéroni, and R. Zeggens are acknowledged.

The help provided by Danielle, Isabelle, Valérie and Petra during these years has been greatly appreciated.

It is difficult not to forget someone, so my last acknowledgement is for those who have worked, discussed, and exchanged ideas with me and who are not listed above. Please don't be offended but blame my poor memory.

# Introduction

This report gives a summary of my research on nuclear dynamics during the past ten years.

The choice of this field has been motivated by the desire to understand the physics of complex systems obeying quantum mechanics. In particular, the interplay between collective motion and single-particle degrees of freedom is a source of complex and fascinating behaviours.

For instance, giant resonances are characterised by a collective vibration of many nucleons, but their decay may occur by the emission of a single nucleon. Another example could be taken from the collision of nuclei where the transfer of few nucleons may have a strong impact on the formation of a compound system is non trivial.

To describe these complex systems, one needs to solve the quantum many-body problem. The description of the dynamics of composite systems can be very challenging, especially when two such systems interact.

An important goal of nuclear physics is to find a unified way to describe the dynamics of nuclear systems. Ultimately, the same theoretical model should be able to describe vibrations, rotations, fission, all the possible outcomes of heavy-ion collisions (elastic and inelastic scattering, particle transfer, fusion, and multifragmentation), and even the dynamics of neutron star crust.

This desire for a global approach to nuclear dynamics has strongly influenced my research activities. In particular, all the numerical applications presented in this report have been obtained from few numerical codes solving equations derived from the same variational principle.

Beside the quest for a unified model of nuclear dynamics, possible applications of heavy-ion collisions such as the formation of new nuclei is also a strong motivation for the experimental and theoretical studies of reaction mechanisms.

This report is not a review article, but should be considered as a reading guide of the main papers my collaborators and myself have published. It also gives the opportunity to detail some aspects which are usually not discussed in papers, such as the development of numerical codes.

Advances in science often involve strong collaborations between experimentalists

and theoreticians. This is particularly true in the field of nuclear reaction mechanisms. Although this report presents essentially theoretical works, some experimental studies of reaction mechanisms are also discussed.

Formalism and code development are presented in chapter 1. Studies of collective vibrations are then collected in chapter 2, while heavy-ion collisions are investigated in chapter 3.

# Chapter 1

## Theoretical approach to nuclear quantum dynamics: the time-dependent Hartree-Fock theory and its extensions

### 1.1 Introduction

The quantum many-body problem is common to many theoretical fields. It aims at describing the structure and dynamics of interacting particles. Electrons, atoms, molecules and nucleons are usual constituents of quantum many-body systems.

In the non-relativistic regime, these systems obey the Schrödinger equation.

$$i\frac{d|\Psi(t)\rangle}{dt} = \hat{H}|\Psi(t)\rangle, \quad (1.1)$$

where  $|\Psi(t)\rangle$  describes the state of the many-body system and  $\hat{H}$  is the microscopic Hamiltonian. We use the notation  $\hbar \equiv 1$ . This equation can be solved exactly for simple cases only. Generally, one has to rely on some approximations.

Variational principles offer an elegant starting point to build such approximations. Indeed, they ensure an optimization of the equations of motion under the approximation that the variational space is limited to a sub-space of the full Hilbert (or Fock) space. Of course, without any restriction of the variational space, it is required that the chosen variational principle allows to recover the Schrödinger equation. However, their usefulness appears when restricting the variational space. Then, the validity of the approximation relies entirely on the choice of the variational space. In one hand, the latter has to be small enough so that the problem is numerically tractable. In the other hand, the variational space should contain

the relevant degrees of freedom to allow for a realistic description of the physical processes.

Although the Schrödinger equation is unique, different variational principles have been developed in the past. One of the mostly used is based on the action

$$S[t_0, t_1; \Psi(t)] = \int_{t_0}^{t_1} dt \langle \Psi(t) | \left( i \frac{d}{dt} - \hat{H} \right) | \Psi(t) \rangle. \quad (1.2)$$

The variational principle  $\delta S = 0$  is applied with the boundary conditions  $\delta \Psi(t_0) = \delta \Psi(t_1) = 0$ . If  $\Psi$  is allowed to span the entire Hilbert space, one recovers the Schrödinger equation.

In most practical applications, mean-field models are considered in a first approximation, and, eventually, serve as a basis for beyond-mean-field approaches [40, LAC04]. To construct such a mean-field theory from the above variational principle, one restricts the variational space by assuming that the  $N$  particles (we consider fermions) are independent. In this case, they may be described by a Slater determinant

$$|\phi\rangle = \prod_{i=1}^N \hat{a}_i^\dagger |-\rangle, \quad (1.3)$$

where  $\hat{a}_i^\dagger$  creates a particle in the state  $|\varphi_i\rangle$  when it is applied to the particle vacuum  $|-\rangle$ . In such a state, all the information is contained in the one-body density-matrix  $\rho$  associated to the single-particle operator

$$\hat{\rho} = \sum_{i=1}^N |\varphi_i\rangle \langle \varphi_i|. \quad (1.4)$$

Solving the variational principle where the action defined in Eq. 1.2 is required to be stationary in the subspace of Slater determinants  $|\phi\rangle$  with fixed boundary conditions at times  $t_0$  and  $t_1$  leads to (see appendix A)

$$i \frac{\partial \rho}{\partial t} = [h[\rho], \rho], \quad (1.5)$$

where  $h[\rho]$  is the Hartree-Fock (HF) single-particle Hamiltonian with matrix elements

$$h_{\alpha\beta} = \frac{\delta \langle \phi | \hat{H} | \phi \rangle}{\delta \rho_{\beta\alpha}}, \quad (1.6)$$

and

$$\rho_{\alpha\beta} = \langle \varphi_\alpha | \hat{\rho} | \varphi_\beta \rangle = \langle \phi | \hat{a}_\beta^\dagger \hat{a}_\alpha | \phi \rangle. \quad (1.7)$$

Eq. 1.5 is the time-dependent Hartree-Fock (TDHF) equation. It was obtained by Dirac in 1930 [Dir30]. It provides a self-consistent mean-field evolution where

the interaction between the particles is replaced by a one-body mean-field potential generated by all the particles. It is, then, assumed that each particle evolves independently in this potential.

Several other variational principles have been proposed, depending on the physics one wants to address. For instance, Blaizot and Ripka introduced in 1981 a variational principle appropriate to the calculation of transition amplitudes [BR81]. Inspired by this work, Balian and Vénéroni (BV) presented the same year their variational principle for the expectation value of an observable [BV81]. In the latter, both the state of the system and the observable of interest are allowed to vary in their own variational space.

In particular, the BV variational principle allows a more transparent interpretation of the TDHF theory [BV81]: it is shown that the TDHF equation 1.5 is optimized for the *expectation value of one-body observables*. TDHF calculations are indeed successful to predict such quantities (several examples will be presented and references to other works will be provided in the following chapters). It also explains why TDHF fails to reproduce other quantities such as fluctuations of one-body operators [KDMR<sup>+</sup>77, DMRKN78, DDP79], which are outside the variational space used to derive the TDHF equation. In fact, to predict such fluctuations, Balian and Vénéroni proposed a prescription also based on their variational principle, but with a different variational space for the observable evolution [BV84, BV92].

## 1.2 The Balian-Vénéroni variational principle

The BV variational principle has been applied to different problems in nuclear physics [TV85, MK85, BF85, ZPG88, BS08, Bro09, 27], hot Fermi gas [MV91],  $\phi^4$ -theory [Mar95, Mar99], and Boson systems [BF99, BB10]. The first realistic application of the BV prescription to fragment mass and charge distributions in heavy-ion collisions are reported in Ref. [27] and will be discussed in section 3.4. The importance of the BV variational principle for the interpretation of the TDHF theory, which will be thoroughly discussed and applied in the following chapters, as well as the derivation of the BV prescription for fluctuations and correlations of one-body observables, justify the more detailed discussion in this section.

Let us first define two variational quantities:  $\hat{D}(t)$ , describing the state of the system, and  $\hat{A}(t)$ , describing the evolution of the observable in the Heisenberg picture. The application of the BV variational principle requires two boundary conditions:

$$\hat{D}(t_0) = \hat{D}_0, \tag{1.8}$$

where the initial state of the system  $\hat{D}_0$  is assumed to be known, and

$$\hat{A}(t_1) = \hat{A}_1, \quad (1.9)$$

where  $\langle \hat{A}_1 \rangle$  is the final expectation value we want to compute at  $t_1 > t_0$ .

The action-like quantity defined by Balian and Vénéroni reads [BV81]

$$J = \text{Tr} \left[ \hat{A}(t_1) \hat{D}(t_1) \right] - \int_{t_0}^{t_1} dt \text{Tr} \left[ \hat{A}(t) \left( \frac{d\hat{D}(t)}{dt} + i [\hat{H}(t), \hat{D}(t)] \right) \right]. \quad (1.10)$$

We see that, imposing  $\delta_A J = 0$ , where  $\delta_A$  induces small variations of  $\hat{A}(t)$ , leads to the Liouville-Von Neumann equation

$$i \frac{d\hat{D}(t)}{dt} = [\hat{H}, \hat{D}(t)] \quad (1.11)$$

which is fully equivalent to the Schrödinger equation.

To get Eq. 1.11, we first note that, according to the boundary condition in Eq. 1.9,  $\hat{A}(t_1)$  is fixed and we get

$$\delta_A J = - \int_{t_0}^{t_1} dt \text{Tr} \left[ \delta_A \hat{A}(t) \left( \frac{d\hat{D}(t)}{dt} + i [\hat{H}(t), \hat{D}(t)] \right) \right].$$

To be equal to zero for any variation of  $\hat{A}$ , the term inside the brackets must be zero, giving Eq. 1.11.

Variations of  $\hat{D}(t)$  should also be considered. It is easier to first rewrite Eq. 1.10 as

$$J = \text{Tr} \left[ \hat{A}(t_0) \hat{D}(t_0) \right] + \int_{t_0}^{t_1} dt \text{Tr} \left[ \hat{D}(t) \left( \frac{d\hat{A}(t)}{dt} + i [\hat{H}(t), \hat{A}(t)] \right) \right]. \quad (1.12)$$

To get Eq. 1.12 we integrate by part the  $\int dt \hat{A} \partial_t \hat{D}$  term in Eq. 1.10 and we use the relation  $\text{Tr}(\hat{A}[\hat{H}, \hat{D}]) = -\text{Tr}(\hat{D}[\hat{H}, \hat{A}])$ .

Equivalently to Eq. 1.11, with the boundary condition in Eq. 1.8, requiring  $\delta_D J = 0$  leads to

$$i \frac{d\hat{A}(t)}{dt} = [\hat{H}, \hat{A}(t)], \quad (1.13)$$

which is also equivalent to the Schrödinger equation, and is expressed in the Heisenberg picture.

### 1.3 Derivation of the time-dependent Hartree-Fock equation

The TDHF theory is obtained under the approximation that  $\hat{A}(t)$  is constrained to the one-body operator space and that  $\hat{D}(t)$  is an independent particle state. As a

result, TDHF is optimized for the expectation value of one-body operators only. In principle, it should not be applied to compute other quantities, such as expectation values of two-body operators, which are outside the variational space of  $\hat{A}(t)$ .

Thus, the variation  $\delta_A$  has to leave  $\hat{A}$  in the space of one-body operators. As we consider arbitrary variations, we can choose

$$\delta_A \hat{A}(t) \equiv \hat{a}_\alpha^\dagger \hat{a}_\beta \text{ for } t_0 \leq t < t_1 \quad (1.14)$$

and  $\delta \hat{A}(t_1) = 0$  due to the boundary condition in Eq. 1.9. Requiring  $\delta_A J = 0$ , we get from Eq. 1.10

$$\text{Tr} \left[ \hat{a}_\alpha^\dagger \hat{a}_\beta \left( \frac{d\hat{D}}{dt} + i[\hat{H}, \hat{D}] \right) \right] = 0. \quad (1.15)$$

In addition, the state of the system is constrained to be an independent particle state. The variational space for  $\hat{D}(t)$  is then defined by  $\hat{D}(t) = |\phi(t)\rangle\langle\phi(t)|$  where  $|\phi(t)\rangle$  is a Slater determinant. Introducing the one-body density matrix of a Slater determinant from Eq. 1.7, we get

$$i \frac{d\rho_{\beta\alpha}(t)}{dt} = \langle\phi(t)| \left[ \hat{a}_\alpha^\dagger \hat{a}_\beta, \hat{H} \right] |\phi(t)\rangle. \quad (1.16)$$

Consider a Hamiltonian of the form

$$\hat{H} = \sum_{ij} t_{ij} \hat{a}_i^\dagger \hat{a}_j + \frac{1}{4} \sum_{ijkl} \bar{v}_{ijkl} \hat{a}_i^\dagger \hat{a}_j^\dagger \hat{a}_l \hat{a}_k \quad (1.17)$$

where matrix elements associated to the kinetic energy and to the anti-symmetric two-body interaction are given, respectively, by

$$t_{ij} = \frac{1}{2m} \langle i | \hat{p}^2 | j \rangle \quad \text{and} \quad (1.18)$$

$$\bar{v}_{ijkl} = v_{ijkl} - v_{ijlk}. \quad (1.19)$$

Reporting the Hamiltonian expression (Eq. 1.17) in Eq. 1.16, we get

$$i \frac{d\rho_{\beta\alpha}}{dt} = \sum_{kl} t_{kl} \langle [\hat{a}_\alpha^\dagger \hat{a}_\beta, \hat{a}_k^\dagger \hat{a}_l] \rangle + \frac{1}{4} \sum_{klmn} \bar{v}_{klmn} \langle [\hat{a}_\alpha^\dagger \hat{a}_\beta, \hat{a}_k^\dagger \hat{a}_l^\dagger \hat{a}_n \hat{a}_m] \rangle \quad (1.20)$$

where the time variable has been dropped and  $\langle \dots \rangle$  denotes the expectation value on  $|\phi(t)\rangle$  to simplify the notation. Eq. 1.20 leads to the TDHF equation

$$i \frac{d\rho_{\beta\alpha}}{dt} = [h[\rho], \rho]_{\beta\alpha}. \quad (1.21)$$

The single-particle Hartree-Fock Hamiltonian reads

$$h[\rho] = t + U[\rho] \quad (1.22)$$

with the self-consistent mean-field

$$U[\rho]_{ij} = \sum_{kl} \bar{v}_{ijkl} \rho_{lk}. \quad (1.23)$$

To show the equivalence between Eq. 1.20 and the TDHF equation, let us start with the term associated to the kinetic energy:

$$\begin{aligned} \langle [\hat{a}_i^\dagger \hat{a}_j, \hat{a}_k^\dagger \hat{a}_l] \rangle &= \langle \hat{a}_i^\dagger \hat{a}_j \hat{a}_k^\dagger \hat{a}_l \rangle - \langle \hat{a}_k^\dagger \hat{a}_l \hat{a}_i^\dagger \hat{a}_j \rangle \\ &= \delta_{jk} \langle \hat{a}_i^\dagger \hat{a}_l \rangle - \langle \hat{a}_i^\dagger \hat{a}_k^\dagger \hat{a}_j \hat{a}_l \rangle - \delta_{il} \langle \hat{a}_k^\dagger \hat{a}_j \rangle + \langle \hat{a}_k^\dagger \hat{a}_i^\dagger \hat{a}_l \hat{a}_j \rangle \\ &= \delta_{jk} \rho_{li} - \delta_{il} \rho_{jk}. \end{aligned}$$

Using the Wick theorem and Eq. 1.7, the kinetic energy term reduces to

$$\sum_{kl} t_{kl} \langle [\hat{a}_i^\dagger \hat{a}_j, \hat{a}_k^\dagger \hat{a}_l] \rangle = \sum_k (t_{jk} \rho_{ki} - t_{ki} \rho_{jk}).$$

For the two-body interaction, we need the expectation value of the commutator

$$\begin{aligned} \langle [\hat{a}_i^\dagger \hat{a}_j, \hat{a}_k^\dagger \hat{a}_l^\dagger \hat{a}_n \hat{a}_m] \rangle &= \langle \hat{a}_i^\dagger \hat{a}_j \hat{a}_k^\dagger \hat{a}_l^\dagger \hat{a}_n \hat{a}_m \rangle - \langle \hat{a}_k^\dagger \hat{a}_l^\dagger \hat{a}_n \hat{a}_m \hat{a}_i^\dagger \hat{a}_j \rangle \\ &= \langle \hat{a}_i^\dagger \hat{a}_j^\dagger \hat{a}_n \hat{a}_m \rangle \delta_{jk} - \langle \hat{a}_i^\dagger \hat{a}_k^\dagger \hat{a}_n \hat{a}_m \rangle \delta_{jl} + \langle \hat{a}_i^\dagger \hat{a}_k^\dagger \hat{a}_l^\dagger \hat{a}_j \hat{a}_n \hat{a}_m \rangle \\ &\quad - \langle \hat{a}_k^\dagger \hat{a}_l^\dagger \hat{a}_n \hat{a}_j \rangle \delta_{mi} + \langle \hat{a}_k^\dagger \hat{a}_l^\dagger \hat{a}_m \hat{a}_j \rangle \delta_{ni} - \langle \hat{a}_k^\dagger \hat{a}_l^\dagger \hat{a}_i^\dagger \hat{a}_n \hat{a}_m \hat{a}_j \rangle. \end{aligned}$$

The two terms with 6 annihilation/creation operators cancel out and we get

$$\begin{aligned} \langle [\hat{a}_i^\dagger \hat{a}_j, \hat{a}_k^\dagger \hat{a}_l^\dagger \hat{a}_n \hat{a}_m] \rangle &= (\rho_{mi} \rho_{nl} - \rho_{ml} \rho_{ni}) \delta_{jk} + (\rho_{mk} \rho_{ni} - \rho_{mi} \rho_{nk}) \delta_{jl} \\ &\quad + (\rho_{jl} \rho_{nk} - \rho_{jk} \rho_{nl}) \delta_{mi} + (\rho_{jk} \rho_{ml} - \rho_{jl} \rho_{mk}) \delta_{ni} \end{aligned}$$

Altogether, the two-body interaction contribution reduces to

$$\begin{aligned} \frac{1}{4} \sum_{klmn} \bar{v}_{klmn} \langle [\hat{a}_i^\dagger \hat{a}_j, \hat{a}_k^\dagger \hat{a}_l^\dagger \hat{a}_n \hat{a}_m] \rangle &= \frac{1}{2} \sum_{klm} [\bar{v}_{jklm} (\rho_{li} \rho_{mk} - \rho_{lk} \rho_{mi}) + \bar{v}_{klim} (\rho_{jl} \rho_{mk} - \rho_{jk} \rho_{ml})] \\ &= \sum_{klm} [\bar{v}_{jklm} (\rho_{li} \rho_{mk}) - \bar{v}_{klim} (\rho_{jk} \rho_{ml})] \\ &= \sum_k (U[\rho]_{jk} \rho_{ki} - U[\rho]_{ki} \rho_{jk}) \end{aligned}$$

where we have used  $\bar{v}_{klmn} = -\bar{v}_{klnm} = -\bar{v}_{lkmn}$ . Gathering the kinetic and interaction terms gives

$$i \frac{d\rho_{\beta\alpha}}{dt} = \sum_k [(t_{\beta k} + U_{\beta k}[\rho]) \rho_{k\alpha} - (t_{k\alpha} + U_{k\alpha}[\rho]) \rho_{\beta k}] = [h[\rho], \rho]_{\beta\alpha}.$$

We see that the TDHF equation is obtained by solving the BV variational principle with the variational spaces restricted to Slater determinants for the state of the system and to one-body operators for the observable. It is interesting to see that only the variation of  $\hat{A}$  is needed to get the TDHF equation. In addition, solving the TDHF equation allows to compute any one-body observables, and the equation does not depend on the final time  $t_1$  entering the BV action. These properties are specific to the TDHF case. In general, the resulting equations of motion are obtained from

both the variation of  $\hat{A}$  and  $\hat{D}$ , and the results are valid for only one observable  $\hat{A}_1$  and one final time  $t_1$ .

We recall that the TDHF equation is optimized for the expectation value of one-body operators and should not be used, in principle for other purposes. In particular, two-body operators and fluctuations of one-body operators are outside the variational space. In the next section, we solve the BV variational principle in order to compute such fluctuations. (The case of more general two-body operators would be more complicated and the resulting equations of motions are not expected to be easily solvable numerically.)

## 1.4 The Balian-Vénéroni prescription for fluctuations and correlations of one-body observables

Let  $\hat{X}$  and  $\hat{Y}$  be two observables. Their correlation in the state  $|\Psi\rangle$  is defined as

$$\sigma_{XY} = \sqrt{\frac{1}{2} \left( \langle \hat{X}\hat{Y} \rangle + \langle \hat{Y}\hat{X} \rangle \right) - \langle \hat{X} \rangle \langle \hat{Y} \rangle}. \quad (1.24)$$

The case  $\hat{X} = \hat{Y}$  defines the fluctuations of  $\hat{X}$ :

$$\sigma_{XX} \equiv \sigma_X = \sqrt{\langle \hat{X}^2 \rangle - \langle \hat{X} \rangle^2}. \quad (1.25)$$

If  $\hat{X}$  and  $\hat{Y}$  are one-body operators, we see that  $\sigma_{XY}^2$  includes the expectation value of the *square* of a one-body operator, which contains a two-body contribution. Indeed,

$$\hat{X}\hat{Y} = \sum_{\alpha\beta} X_{\alpha\beta} \hat{a}_\alpha^\dagger \hat{a}_\beta \sum_{\mu\nu} Y_{\mu\nu} \hat{a}_\mu^\dagger \hat{a}_\nu = \sum_{\alpha\beta\mu\nu} X_{\alpha\beta} Y_{\mu\nu} (\delta_{\beta\mu} \hat{a}_\alpha^\dagger \hat{a}_\nu - \hat{a}_\alpha^\dagger \hat{a}_\mu^\dagger \hat{a}_\beta \hat{a}_\nu).$$

The last term is clearly of a two-body nature.

Correlations and fluctuations of one-body operators are then outside the range of applicability of the TDHF theory.

One possibility would be to solve the BV variational principle with a variational space for the observable which is composed of the square of one-body operators [Flo82]. This approach, however, leads to complicated equations of motion due to an intricate coupling between the evolution of the observable  $\hat{A}(t)$  and of the state  $\hat{D}(t)$ .

Fluctuations and correlations of one-body operators  $\hat{Q}_i = \sum_{\alpha\beta} Q_{i\alpha\beta} \hat{a}_\alpha^\dagger \hat{a}_\beta$  can also be computed from the expectation value of

$$\hat{A}_1 \equiv e^{-\sum_i \varepsilon_i \hat{Q}_i} \quad (1.26)$$

in the limit  $\varepsilon_i \rightarrow 0$ . Indeed, we have

$$\ln \langle \hat{A}_1 \rangle = - \sum_i \varepsilon_i \langle \hat{Q}_i \rangle + \frac{1}{2} \sum_{ij} \varepsilon_i \varepsilon_j C_{ij} + O(\varepsilon^3), \quad (1.27)$$

where

$$C_{ij} = \frac{1}{2} \left( \langle \hat{Q}_i \hat{Q}_j \rangle + \langle \hat{Q}_j \hat{Q}_i \rangle \right) - \langle \hat{Q}_i \rangle \langle \hat{Q}_j \rangle = \sigma_{Q_i Q_j}^2. \quad (1.28)$$

Let us show it for  $\hat{A}_1 = e^{-\varepsilon_1 \hat{Q}_1 - \varepsilon_2 \hat{Q}_2}$ . Writing  $f(\varepsilon_1, \varepsilon_2) = \ln \langle \hat{A}_1 \rangle$  up to second order in  $\varepsilon$ , we get

$$f(\varepsilon_1, \varepsilon_2) \simeq \ln \left[ 1 - \varepsilon_1 \langle \hat{Q}_1 \rangle - \varepsilon_2 \langle \hat{Q}_2 \rangle + \frac{1}{2} \left( \varepsilon_1^2 \langle \hat{Q}_1^2 \rangle + \varepsilon_2^2 \langle \hat{Q}_2^2 \rangle + \varepsilon_1 \varepsilon_2 (\langle \hat{Q}_1 \hat{Q}_2 \rangle + \langle \hat{Q}_2 \hat{Q}_1 \rangle) \right) \right].$$

Using  $\ln(1-x) \simeq -x - \frac{x^2}{2}$ , we get

$$\begin{aligned} f(\varepsilon_1, \varepsilon_2) &\simeq \left[ -\varepsilon_1 \langle \hat{Q}_1 \rangle - \varepsilon_2 \langle \hat{Q}_2 \rangle + \frac{1}{2} \left( \varepsilon_1^2 \langle \hat{Q}_1^2 \rangle + \varepsilon_2^2 \langle \hat{Q}_2^2 \rangle + \varepsilon_1 \varepsilon_2 (\langle \hat{Q}_1 \hat{Q}_2 \rangle + \langle \hat{Q}_2 \hat{Q}_1 \rangle) \right) \right] \\ &\quad - \frac{1}{2} \left( \varepsilon_1 \langle \hat{Q}_1 \rangle + \varepsilon_2 \langle \hat{Q}_2 \rangle \right)^2 \\ &= -\varepsilon_1 \langle \hat{Q}_1 \rangle - \varepsilon_2 \langle \hat{Q}_2 \rangle + \frac{\varepsilon_1^2}{2} C_{11} + \frac{\varepsilon_2^2}{2} C_{22} + \varepsilon_1 \varepsilon_2 C_{12}. \end{aligned}$$

The linear and quadratic dependence in  $\varepsilon$  of  $\ln \langle \hat{A}_1 \rangle$  then lead to the expectation values and fluctuations/correlations of the one-body observables  $\hat{Q}_i$ , respectively.

In Ref. [BV84], Balian and Vénéroni applied their variational principle with a variational space for the observable parametrised by

$$\hat{A}(t) = e^{-\hat{L}(t)} = e^{-\sum_{\alpha\beta} L_{\alpha\beta}(t) \hat{a}_\alpha^\dagger \hat{a}_\beta}. \quad (1.29)$$

The density matrix can be constrained to be an independent particle state of the form

$$\hat{D}(t) = |\phi(t)\rangle \langle \phi(t)|, \quad (1.30)$$

where  $|\phi(t)\rangle$  is a Slater determinant. In fact, the original derivation of Balian and Vénéroni [BV92] involves more general mean-field states of the form

$$\hat{D}(t) = e^{-m(t) - \hat{M}(t)} = e^{-m(t) - \sum_{\alpha\beta} M_{\alpha\beta}(t) \hat{a}_\alpha^\dagger \hat{a}_\beta}. \quad (1.31)$$

The particular case of a Slater determinant can be obtained with this parametrisation by letting the eigenvalues of the matrix  $M(t)$  tend to  $\pm\infty$ , with the normalization factor  $m(t)$  also tending to  $+\infty$  in such a way as to keep the norm  $z(t) = \text{Tr}(\hat{D}(t))$  equal to 1 [BV85]. In this case, the Slater determinant  $|\Phi(t)\rangle$  is built from the eigenvectors of  $M(t)$  associated with the eigenvalues  $-\infty$ .

Comparing Eqs. 1.29 and 1.31, we see that both variational spaces for the state and the observable are similar, being both composed of exponentials of one-body operators.

The resolution of the BV variational principle with this choice of variational spaces and assuming the boundary conditions given in Eqs. 1.8 and 1.9 is rather tedious. It is given in details in Refs. [BV92, Bro09].

Expanding the one-body density matrix in terms of  $\varepsilon$ ,

$$\rho(t) = \rho^{(0)}(t) + \sum_i \varepsilon_i \rho_i^{(1)}(t) + \dots, \quad (1.32)$$

the main results read:

- The expectation value of  $\hat{Q}_i$  is given by

$$\langle \hat{Q}_i \rangle(t_1) = \text{tr}(\rho^{(0)}(t_1)Q_i) \quad (1.33)$$

where  $\rho^{(0)}$  is given by the TDHF equation 1.5 with the boundary condition

$$\rho_{\alpha\beta}^{(0)}(t_0) = \text{Tr}(\hat{D}_0 \hat{a}_\beta^\dagger \hat{a}_\alpha) \quad (1.34)$$

and  $\hat{D}_0$  is the initial density matrix.

- The fluctuations/correlations  $\sigma_{Q_i Q_j}$  obey

$$\sigma_{Q_i Q_j}^2(t_1) = C_{ij}(t_1) = C_{ij}^{TDHF}(t_1) - \text{tr}(\rho_j^{(1)}(t_1)Q_i) \quad (1.35)$$

where

$$C_{ij}^{TDHF}(t_1) = \frac{1}{2} \text{tr}(\rho^{(0)}(t_1)[Q_i, Q_j]) + \text{tr}[Q_i \rho^{(0)}(t_1) Q_j (1 - \rho^{(0)}(t_1))] \quad (1.36)$$

are the (square of the) fluctuations/correlations obtained from the standard TDHF approach.

Eq. 1.35 gives fluctuations and correlations which differ from the standard TDHF result. This is not surprising as fluctuations/correlations of one-body operators are outside the range of application of the TDHF theory, while Eq. 1.35 is optimized for these quantities.

The additional term in Eq. 1.35 involves  $\rho^{(1)}$ , i.e., the part of the one-body density matrix which is linear in  $\varepsilon$ . However, the equation of motion for the latter is not trivial. Fortunately, for a Slater determinant, Eq. 1.35 can be re-written so that it is easier to implement. The final result reads [BV92, Bro09]

$$C_{ij}(t_1) = \lim_{\varepsilon_i, \varepsilon_j \rightarrow 0} \frac{1}{2\varepsilon_i \varepsilon_j} \text{tr}[(\rho^{(0)}(t_0) - \eta_i(t_0, \varepsilon_i))(\rho^{(0)}(t_0) - \eta_j(t_0, \varepsilon_j))], \quad (1.37)$$

where the single-particle matrices  $\eta(t, \varepsilon)$  obey the TDHF equation 1.5 with a boundary condition defined at the final time  $t_1$ :

$$\eta_j(t_1, \varepsilon_j) = e^{i\varepsilon_j Q_j} \rho^{(0)}(t_1) e^{-i\varepsilon_j Q_j}. \quad (1.38)$$

The fluctuations  $\sigma_{Q_i} = \sqrt{C_{ii}}$  are determined by taking  $Q_i = Q_j$ , leading to

$$C_{ii} = \lim_{\varepsilon_i \rightarrow 0} \frac{1}{2\varepsilon_i^2} \text{tr}[(\rho^{(0)}(t_0) - \eta_i(t_0, \varepsilon_i))^2], \quad (1.39)$$

with the boundary condition of Eq. 1.38.

Eq. 1.38 imposes to solve the TDHF equation first for  $\rho^{(0)}(t)$  forward in time, and then for  $\eta(t)$  backward in time. Numerical applications solving Eq. 1.39 with

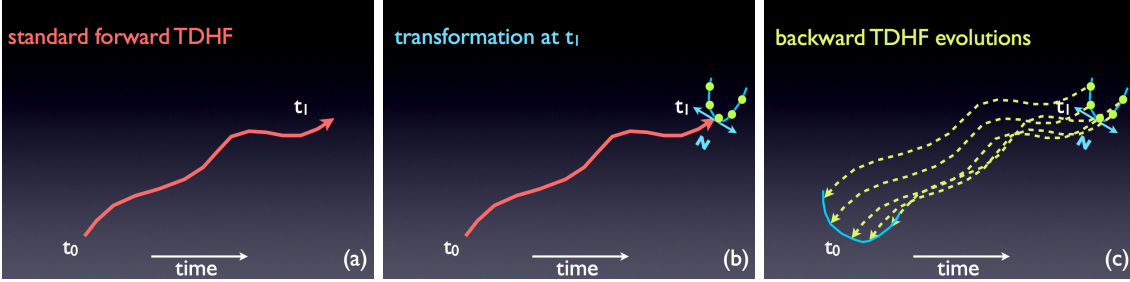


Figure 1.1: Schematic illustration of the main numerical steps to compute the fluctuation of the one-body observable  $\hat{N}$  (e.g., neutron numbers in one fragment following a heavy-ion collision). (a) We perform a standard TDHF evolution from  $t_0$  to  $t_1$ . (b) The transformation given in Eq. 1.38 is performed on the one-body density matrix at time  $t_1$  with several (small) values of  $\epsilon$ . (c) Backward TDHF evolutions from  $t_1$  to  $t_0$  are performed for each  $\epsilon$  and the resulting one-body density matrices at time  $t_0$  are used to compute the (square of the) fluctuations from Eq. 1.39.

the boundary condition given in Eq. 1.38 are detailed in [TV85, MK85, BF85, BS08, Bro09, 27]. In practice, several (typically  $\sim 5$  in [27]) backward TDHF trajectories with different but small values of  $\epsilon$  are performed to compute the limit in Eq. 1.39. Fig. 1.1 gives a schematic illustration of the numerical technique. In Ref. [27], Eq. 1.37 is also solved. It is used to compute the correlations between proton and neutron numbers in fragments following deep-inelastic collisions in addition to their fluctuations (see section 3.4).

It is important to note that, although Eqs. 1.37 and 1.39 are rather easy to solve numerically with a slightly modified TDHF code, they only provide the fluctuations/correlations for a specific choice of  $\hat{Q}_i$  and  $\hat{Q}_j$  at the time  $t_1$ . Another choice of operator(s) and/or final time imply to compute numerically another set of backward TDHF evolutions. This was not the case for the calculation of expectation values of one-body observables which only requires one forward TDHF evolution. Indeed, solving the TDHF equation is an initial value problem and the resulting one-body density matrix can be used to compute any one-body observable (i.e., the TDHF equation depends neither on  $t_1$  nor on  $\hat{Q}_i$ ). As a result, the determination of fluctuations and correlations of one-body observables from the BV variational principle is much more computational time consuming than standard TDHF calculations of their expectation values.

## 1.5 Numerical solution of the TDHF equation

As we saw in the previous sections, the calculations of both expectation values and fluctuations/correlations of one-body observables imply to determine the time evolution of the one-body density matrix with the TDHF equation 1.5. Few numerical codes solving the TDHF equation in three dimensions with a full Skyrme energy density functional (EDF) including spin-orbit terms [Sky56, CBH<sup>+</sup>98] are now available [KOB97, MRS<sup>+</sup>05, NY05, UO05, SFdlM09]. They were used in many studies of giant resonance properties [32, 9, SSRSN04, NY05, UO05, RGM07, BS08, 33, SBMR11, 3, SLBW], neutron star crust properties [SFdlM09, SdlMF11], and nuclear reactions [KOB97, 34, 35, MRSS06, UO06c, UO06b, UO06d, UO06a, GMR07, 36, UO07, GMRH08, 28, UOM08, UO08, WL08, AWL09, AL09, 13, UOMR09, UO09a, UO09b, WL09, WAL09, IOMI09, UMIO10, UOMR10, 18, 26, OUMR10, IOMI10a, IOMI10b, LMR11, 27, IM11, YALW11, 11, 39, 21, UOMR12].

### 1.5.1 Numerical method

All these applications were performed on a three-dimensional cartesian grid using a time iterative method. Algorithms and numerical techniques are detailed in [40]. We give here a summary of the main steps which are usually followed to treat the collision of two nuclei:

1. Static Hartree-Fock (HF) calculations are performed to determine the initial condition where the nuclei are usually assumed to be in their HF ground state.
2. The nuclei are placed in a larger box, avoiding any overlap of the HF solutions. This latter condition allows to construct a single Slater determinant from the two initial HF states.
3. A Galilean boost<sup>1</sup> is applied at the initial time assuming that the nuclei followed a Rutherford trajectory prior to this time.
4. The TDHF equation is solved iteratively in time and expectation values of one-body observables are eventually computed at each time step to get their time evolution.

---

<sup>1</sup>In case of a single nucleus, for instance to study its response to a specific excitation, the Galilean boost is replaced by the appropriate velocity boost generating the excitation (examples are given in chapter 2). Alternatively, one can start with a constrained Hartree-Fock (CHF) solution obtained with an external constraint in the HF calculation. The response to the excitation is then studied by relaxing the constraint in the TDHF calculation [BF79].

Of course, variations of the main numerical steps described above are possible. For instance, one can question the validity of the assumption that the nuclei are in their HF ground state at initial time. In particular, heavy nuclei generate strong Coulomb fields which may induce long range excitations of the collision partner<sup>2</sup> (see, e.g., Ref. [35]).

### 1.5.2 The TDHF3D code

All three-dimensional calculations presented in this report are performed with the TDHF3D code. The TDHF3D code was initially developed by Paul Bonche and a first application of this code was presented at the FUSION97 conference [KOB97]. The responsibility for testing, debugging, and further improving the code was transferred to me at the start of my PhD in 2000. The TDHF3D code is now used by several teams [34, 32, 9, 35, 30, 36, 28, 13, 33, 18, 26, 27, 11, 21, 39, WL08, AWL09, AL09, 13, WL09, WAL09, IOMI09, IOMI10a, IOMI10b, IM11, YALW11, SLBW].

#### Initial HF states

The initial condition uses HF solutions of a specific version of the EV8 code [BFH05]. In this version, the EV8 code solves the static HF equation without pairing.

Initially, this code neglected all center of mass corrections to the kinetic energy, while usual Skyrme EDF take at least the one-body part of these corrections into account [CBH<sup>+</sup>98]. Neglecting these corrections allows a consistent treatment of both nuclei in case of a collision. Indeed, these corrections are explicitly dependent on the number of nucleons  $A_i$  of the collision partner  $i$  and would induce a different treatment of the single-particle wave-functions depending on which nucleus they come from. One can then either include these corrections in the static HF calculations and neglect them in the TDHF evolution. However, in this case, the consistency between the calculations of the structure and the dynamics is lost. The other possibility, which is used here, is to drop these corrections at the HF level. It is then necessary to use Skyrme EDF which have been fitted *without* these corrections. This is the case of the SLy4*d* parametrisation [KOB97] which is widely used in this report. Apart from the one-body correction to the center of mass kinetic energy, the SLy4*d* is fitted with the same protocol as the SLy4 parametrisation [CBH<sup>+</sup>98]. (The *d* stands for "dynamics".)

In the case of a single nucleus, the calculations are usually performed in the intrinsic frame and removing the center of mass corrections to the kinetic energy is not mandatory. I then introduced an option in both static and dynamical codes to take into account these corrections for, e.g., a systematic comparison of vibrational spectra obtained with different available parametrisations of

---

<sup>2</sup>The treatment of initial Coulomb polarisation has been included as an option in the TDHF3D code (see sec. 1.5.2).

the Skyrme EDF.

## Numerical approximations and algorithm

Most of the numerical approximations and techniques used in the TDHF3D code are the same as in the EV8 code published in Ref. [BFH05]. This is the case, for instance for spatial derivatives which are calculated by seven and nine points finite-difference formulae for the first and second derivatives, respectively. With these approximations, a good convergence of HF energies is obtained with a regular mesh spacing  $\Delta x = 0.8$  fm. Smaller meshes (e.g.,  $\Delta x = 0.6$  fm) are sometimes used to test the Galilean invariance of the TDHF calculations. The largest sizes of the grid which have been used for, e.g., non-central actinide collisions, are of the order of  $100 \times 100 \times 32/2$  points with  $\Delta x = 0.8$  fm. The  $1/2$  factor comes from the fact that, in its present form, the code contains a plane of symmetry (the collision plane).

The code contains all the odd and even terms of standard Skyrme EDF, similar to the "cranking" calculations for rotating even-even nuclei described in [BFH87]. The inclusion of odd terms is indeed crucial for a proper description of translational motion and to avoid spurious excitations [MRSS06]. As a result, the TDHF3D code contains no degeneracy of single-particle wave-functions. This means that up to  $\sim 500$  (for, e.g., two actinides) wave-functions are evolved in time.

Due to the self-consistency of the mean-field, the TDHF equation needs to be solved iteratively in time with a small time step increment  $\Delta t$ . Over small time intervals  $[t, t + \Delta t]$ , the Hamiltonian is assumed to be constant. However, to conserve energy, the numerical algorithm should be symmetric with respect to time-reversal operation. This implies to consider the Hamiltonian value at time  $t + \frac{\Delta t}{2}$  for the evolution of single-particle wave-functions from  $t$  to  $t + \Delta t$  [BKN76]<sup>3</sup>

$$|\nu(t + \Delta t)\rangle \approx e^{-i\frac{\Delta t}{\hbar}\hat{h}(t+\frac{\Delta t}{2})} |\nu(t)\rangle. \quad (1.40)$$

A schematic illustration of the real time propagation could be written as:

$$\begin{array}{ccccc} \{|\nu_1^{(n)}\rangle \cdots |\nu_N^{(n)}\rangle\} & \Rightarrow & \rho^{(n)} & \Rightarrow & \hat{h}^{(n)} \equiv \hat{h}[\rho^{(n)}] \\ & & & & \Downarrow \\ & \uparrow & & & |\tilde{\nu}_i^{(n+1)}\rangle = e^{-i\frac{\Delta t}{\hbar}\hat{h}^{(n)}} |\nu_i^{(n)}\rangle \\ |\nu_i^{(n+1)}\rangle = e^{-i\frac{\Delta t}{\hbar}\hat{h}^{(n+\frac{1}{2})}} |\nu_i^{(n)}\rangle & & & & \Downarrow \\ & \uparrow & & & \tilde{\rho}^{(n+1)} \\ \hat{h}^{(n+\frac{1}{2})} \equiv \hat{h} \left[ \rho^{(n+\frac{1}{2})} \right] & \Leftarrow & \rho^{(n+\frac{1}{2})} = \frac{\rho^{(n)} + \tilde{\rho}^{(n+1)}}{2} & \Leftarrow & \end{array}$$

where  $|\nu^{(n)}\rangle$  corresponds to an approximation of  $|\nu(t_n = n\Delta t)\rangle$ . In this algorithm, starting from the density at time  $t$ , a first estimate of the density at time  $t +$

<sup>3</sup>This algorithm is similar to a Runge-Kutta method.

$\Delta t$ , denoted by  $\tilde{\rho}^{(n+1)}$  is obtained. The Hamiltonian used in the propagator is computed using the average density obtained from  $\rho^{(n)}$  and  $\tilde{\rho}^{(n+1)}$ . Then, the new density at time  $t + \Delta t$  is obtained using this Hamiltonian. An approximate form of the exponential is generally used which in some cases, breaks the unitarity, and orthonormalization of the single particle states must be controlled. In practice, with  $\Delta x = 0.8$  fm, good convergence is generally obtained with a time step  $\Delta t = 1.5 \times 10^{-24}$  s. Note that typical collision times are usually smaller than  $\sim 10^{-20}$  s (see, e.g., Ref. [13]), corresponding to less than  $10^4$  time iterations.

### Numerical test: the case of Galilean invariance

One requirement of TDHF codes is to obey Galilean invariance. In appendix B, it is shown, using a translational and Galilean invariant Hamiltonian, that a system in translational motion with a velocity  $v$  and a total momentum  $Ap$  is solution of the TDHF equation only if its density is constant in space (which is irrelevant for finite nuclei) or if  $p = mv$ .

A density dependent effective interaction, such as the Skyrme effective interaction, explicitly breaks translational invariance. In appendix B, we show, however, that a TDHF solution with a Skyrme EDF (and no external potential) is Galilean invariant if the rearrangement potential<sup>4</sup> is properly taken into account.

As mentioned before, an application of a preliminary version of the code was published in Ref. [KOB97]. This version, however, was breaking Galilean invariance. It can be seen from Fig. 1.2 showing the time evolution of the distance between the two fragment centers of mass in the  $^{16}\text{O}+^{16}\text{O}$  central collision at  $E_{c.m.} = 8.8$  MeV. The dashed blue line, extracted from [KOB97], shows a fusion trajectory, while the correct TDHF solution leads to a re-separation of the fragments (solid red line).

Applying a Galilean boost  $e^{ik\hat{x}}$ , with  $k = \sqrt{2mE}/\hbar$ , on the single particle states is expected to induce a velocity  $v = \hbar k/m$  along  $x$ . The observed velocity was higher than  $v$ , corresponding to higher kinetic energies than expected. This was due to a bug in the coding of the effective mass dependent parts of the mean-field. After correction of this bug, the code produces correct initial velocities following the initial Galilean boost.

The correction of this bug was crucial for quantitative predictions of reaction properties like, e.g., fusion barriers [28].

### Recent and future improvements of the TDHF3D code

Several features have been added to the TDHF3D code which are listed below:

---

<sup>4</sup>The rearrangement potential is the part of the single particle HF Hamiltonian  $h[\rho]$  coming from the density dependence of the effective interaction. It reads  $h^r[\rho]_{ij} = \langle \frac{\delta v[\rho]}{\delta \rho_{ji}} \rangle$ .

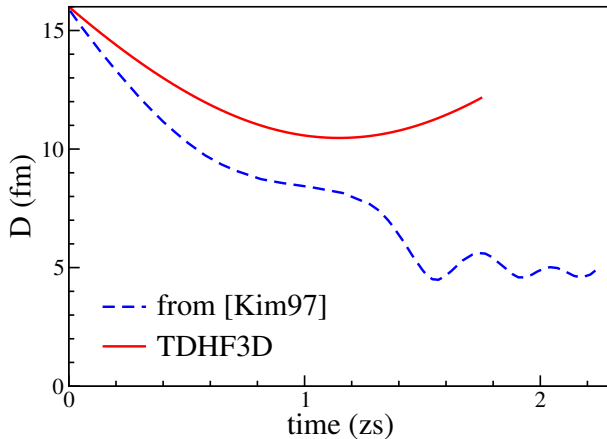


Figure 1.2: Time evolution of the distance  $D$  between the two fragment centers of mass in the  $^{16}\text{O}+^{16}\text{O}$  central collision at  $E_{c.m.} = 8.8$  MeV. The dashed blue line is adapted from [KOB97]. The solid red line is obtained with the present version of the TDHF3D code.

1. *Multipole boosts.* Isovector (IV) and isoscalar (IS) monopole, IV dipole, IS quadrupole, and IS octupole boosts are used to investigate the response of a single nucleus under these excitations [32, 9, 33].
2. *Polarisation of a single nucleus in the Coulomb field of a static or moving (following a Rutherford trajectory) collision partner [35, 30].* The resulting polarised wave-functions can be used to construct the initial condition for a heavy-ion collision. The assumption that the collision partners are in their HF ground state at initial time can then be replaced by the assumption that the nuclei are initially polarized by the Coulomb field of their collision partner.
3. *Possibility to use Skyrme EDF with two density dependences.* This has been done to investigate how different splittings of neutron and proton effective masses with isospin asymmetry affect giant resonances. This ongoing study is performed with recent parametrisations of Skyrme EDF with two density-dependent terms [LBDM06].
4. *Space translation and rotation.* By default, the center of mass of the nucleus is in the center of a cell of the mesh. Space translation is used to move the center of mass anywhere in the cell. Similarly, the deformation axis of a nucleus are, by default, along the  $x$ ,  $y$ , and  $z$  axis only. The space rotation allows to generate any orientation in the  $(x, y)$  plane. This is used to investigate the role of the orientation on the reaction mechanism [30]. The routines use Lagrange mesh and were adapted from the PROMESSE code of M. Bender and collaborators [VHB00].

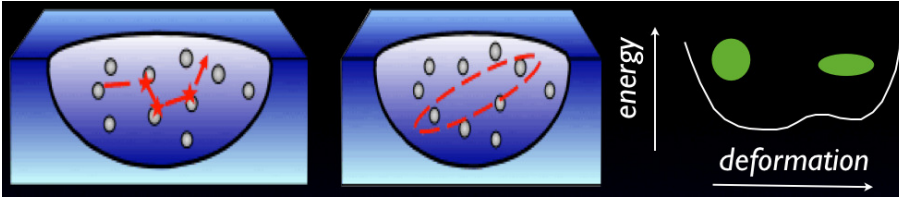


Figure 1.3: (courtesy of D. Lacroix). Illustration of the different kinds of correlations. From left to right: in medium particle-particle collisions, pairing correlations, and large amplitude dynamical correlations.

5. *Calculation of nucleus-nucleus potentials in the frozen approximation.* Nucleus-nucleus potentials are computed from the Skyrme EDF by translating the nuclei in their HF state ("frozen" density) [29]. This feature is used to compare, e.g., TDHF fusion thresholds with the barrier heights of these potentials. The associated code is called FROZEN3D.
6. *Neutron and proton distributions in final fragments.* Probability distributions for  $N$  and  $Z$  of the final fragments are computed at the TDHF level from a particle-number projection technique [26].
7. *Backward evolutions.* This allows to compute fluctuations and correlations of one-body observables from the BV variational principle [27].

Other improvements of the code are ongoing. The first one is to include the full tensor interaction including time-odd terms in a way similar to the recent work presented in Ref. [HHB12]. In particular, the tensor force is expected to increase the dissipation in heavy-ion collisions [IM11], in a way similar to what happens with the spin-orbit term [USR86].

Another important improvement of the code will be to remove the plane of symmetry (collision plane) in order to allow all possible geometries in the entrance channel. This is crucial to determine cross-sections from non-central collisions involving at least one axially-deformed nucleus. Indeed, in addition to an integration over impact parameters, one has to consider all possible orientations of the deformed collision partner(s). This is possible only with 3D unrestricted TDHF codes (i.e., without symmetry assumptions) [UO06c, MRSS06].

## 1.6 Perspectives for beyond TDHF calculations

The TDHF theory is a microscopic quantum mean-field approach of independent particles. Extensions of the TDHF theory, sometimes called "beyond-mean-field

theories”, include correlations which are not present at the TDHF level. These correlations are typically of three kinds illustrated in Fig. 1.3:

- *In medium particle-particle collisions.* In a first approximation, this collision term can be neglected thanks to the Pauli blocking. However, in violent collisions (e.g., central collisions at energies well above the barrier), where the Pauli principle is less efficient to block collisions between nucleons of the two colliding fragments, this term is expected to affect the dynamics. This term is also responsible for the thermalisation of the compound nucleus and for the spreading width of giant resonances.
- *Pairing correlations.* They generate a superfluid phase in nuclei. They have a strong effect on the structure of mid-shell nuclei (e.g., odd-even mass staggering) and in transfer reactions where they favour the transfer of paired nucleons.
- *Large amplitude dynamical correlations.* Unlike a single Slater determinant which is usually localised in a potential energy surface (PES), the correlated state may be described by a configuration mixing of localised states across the entire PES. A typical example in nuclear structure is the zero point motion along a collective coordinate. These correlations allow also for the state to be in a classically forbidden region of the PES, and, then, are necessary to treat quantum tunnelling of the many-body wave function, e.g. in sub-barrier fusion.

The Balian-Vénéroni prescription discussed before is an example where fluctuations and correlations of specific observables, not included at the TDHF level, are described dynamically. In the classification used above, the included correlations belong to the class of dynamical correlations, although, in this case, they are of small amplitude nature. In fact, the fluctuations obtained in Eq 1.39 are those included in the time-dependent random phase approximation (TDRPA) which is obtained assuming small fluctuations of the density matrix around the average evolution [BV92, Ayi08].

A possible extension of TDHF including dynamical correlations of large amplitude involves the path integral technique with the stationary phase approximation (SPA) [Neg82]. The SPA assumes that the path integral is dominated by the classical action (for a single particle), or, equivalently, by the TDHF action for a many-fermion system. The method provides an elegant way to include fluctuations around the mean-field trajectory. Unlike the BV prescription, however, these fluctuations are not limited to a small amplitude limit. This approach leads to a self-consistent eigenvalue problem in four space-time dimensions. It is in fact similar to a HF eigenvalue problem with time as an additional dimension. In case of a vibrational

motion, the problem involves the (difficult) task to find periodic solutions of the TDHF equations. Another important possible application of this path integral approach is to treat quantum tunnelling of the many-body wave function through a barrier. In this case, quantum many-particle closed trajectories in imaginary time need to be found. Up to now, realistic applications in imaginary time have faced the difficulties brought by the limitations of computational power, and only simple cases, such as the spontaneous fission of the  $^8\text{Be}$  in two  $\alpha$  have been studied [Neg82]. However, the recent increase of computational power, and the strong interests in understanding deep-sub-barrier fusion [DHDT<sup>+</sup>07], should lead to a revival of these techniques.

Other examples of beyond-mean-field approaches, such as the time-dependent Hartree-Fock-Bogoliubov (TDHFB) theory, the time-dependent density-matrix (TDDM) theory, the extended and stochastic TDHF theories, and stochastic mean-field (SMF) based on functional integrals are discussed in Ref. [40]. Table 1.1 gives a summary of these approaches. Numerical applications of the three first theories (i.e., TDHF, BV, and TDHFB) are presented in this work.

<i>Name</i>	<i>Approximation</i>	<i>Variational space</i>	<i>Associated observables</i>
TDHF	mean-field (m.-f.)	indep. part.	one-body
BV prescription	m.-f.+ small ampl. fluctuations	indep. part	one-body +fluctuations
Path integrals	m.-f.+ fluctuations	indep. part.	one-body +fluctuations
TDHF-Bogoliubov	m.-f. + pairing	indep. quasipart.	generalized one-body
Extended-TDHF	m.-f. + collision (dissipation)	correlated states	one-body
Stochastic-TDHF	m.-f. + collision (dissipation+fluctuations)	correlated states	one-body
Time-dependent density matrix	m.-f. + two-body correlations	correlated states	one- and two-body
Stochastic m.-f. (Functional integrals)	Exact (within statistical errors)	correlated states	all

Table 1.1: The TDHF approach and several possible extensions.

# Chapter 2

## Collective vibrations

### 2.1 Introduction

A particular interest in strongly interacting systems is their ability to present disorder or chaos, and, in the same excitation energy range, well-organized motion. Atomic nuclei are known to show both behaviors [BM75]. In particular, they exhibit a large variety of vibrations, from low-lying collective modes to giant resonances (GR) with excitation energy usually above the particle emission threshold [HvdW01].

Baldwin and Klaiber observed the isovector giant dipole resonance (GDR) in photofission of uranium nuclei [BK47], interpreted as a vibration of neutrons against protons [GT48]. Other kinds of GR have been discovered, such as the isoscalar giant quadrupole resonance (GQR) associated with an oscillation of the shape between a prolate and an oblate deformation [FT72], and the isoscalar giant monopole resonance (GMR) corresponding to a breathing mode [MWC<sup>+</sup>76, HvdBI<sup>+</sup>77, YRM<sup>+</sup>77].

GR are usually associated with the first phonon of a small-amplitude harmonic motion. In the harmonic picture, it corresponds to a coherent sum of one particle-one hole ( $1p1h$ ) states [BM75]. GR are usually unbound and may decay by particle ( $p, n, d, \alpha, \gamma\dots$ ) emission, leading to an escape width in the GR spectra. The escape width is then due to a coupling of the correlated  $1p1h$  states to the continuum. Other contributions to the width of GR are the Landau damping and the spreading width. Landau damping occurs due to a one-body coupling to non-coherent  $1p1h$  states [PN66]. Such coupling is enhanced by the high density of states in the continuum. The spreading width is due to the residual interaction coupling  $1p1h$  states to  $2p2h$  states. The  $2p2h$  states can also couple to  $3p3h$  states and more complex  $nph$  configurations until an equilibrated system is reached. These contributions to the GR width are illustrated in Fig. 2.1.

The proof of the vibrational nature of GR came with the observation of their two- and three-phonon states [CF95, ABE98, Sca04]. Multiphonon studies also

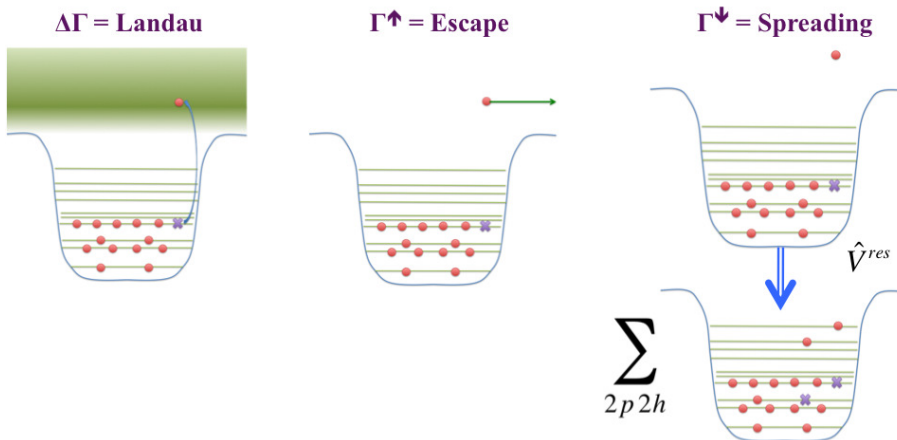


Figure 2.1: Illustration of the three contributions to the width of the GR (see text). (left) Landau damping due to coupling to incoherent  $1p1h$  states. (middle) Escape width due to direct decay. (right) Spreading width due to coupling to  $2p2h$  states.

provided a good test to the harmonic picture. In particular, anharmonicity was found in an abnormally large excitation probability of these states [CF95]. The coupling between different phonon states is predicted to be an important source of this anharmonicity [VCC<sup>+</sup>95, BD97, 32, FCA<sup>+</sup>03, 9, 33, LCA<sup>+</sup>06].

Coherent motion of fermions such as collective vibrations in nuclei can be modeled by time-dependent mean-field approaches like the TDHF theory. In fact, in its linearized version, TDHF is equivalent to the Random Phase Approximation (RPA) [RS80] which is the basic tool to understand the collective vibrations in terms of independent phonons. In particular, time evolution of one-body (collective) observables, which can be estimated using a TDHF code (i.e., neglecting part of the residual interaction), contains relevant informations on the vibration properties, such as their energy spectra.

Direct decay contributing to the escape width can be studied within the continuum-(Q)RPA model<sup>1</sup> [KBFS74, LG76, KLLT98, Mat01, HS01, KSGVG02]. GR direct decay can also be investigated within the TDHF framework [CGS87, PMB88, 3, SLBW]. Indeed, the TDHF theory is able to treat such process as it allows for the evaporation of unbound components of the single particle wave-functions. Due to its one-body nature, Landau damping is also included in RPA and TDHF. However, they do not contain the residual interaction responsible for the spreading width.

An interesting feature of TDHF applications is that they are not limited to small amplitude vibrations, unlike RPA, allowing for investigations of non linear effects in collective motions. In particular, couplings between collective modes, which is a possible source of the anharmonicity discussed above, has been investigated [32, 9,

<sup>1</sup>The quasiparticle-RPA (QRPA) is an extension of the RPA including pairing correlations.

33].

Recently, TDHF codes have been extended to study the role of pairing correlations on collective vibrations at the BCS level [ENI<sup>+</sup>10, SLBW] and within the TDHFB theory. Indeed, TDHFB calculations with full Skyrme EDF are now possible in spherical symmetry [4], and more recently in three dimensions [SBMR11].

In this chapter, we first briefly introduce the linear response theory. For an illustrative purpose, applications of the latter to both low-lying vibrational states and GR are given within the TDHF framework. These standard applications to the linear response theory are followed by an investigation of the direct decay by nucleon emission and its link to the GR microscopic structure. Then, non-linearities in collective vibrations are studied to investigate a possible source of anharmonicity in GR multiphonon spectra. In the last application, we come back to the linear response theory and study pairing vibrations with a TDHFB code recently developed by B. Avez during his PhD. Finally we conclude this chapter and present some perspectives to the study of collective vibrations.

## 2.2 Linear response theory

The linear response theory has been widely used with TDHF to study collective vibrations in nuclei [BF79, SV79, USR86, CGS87, PMB88, CUS96, 32, NY05, UO05, MRS<sup>+</sup>05, AS05, RGM07, SARM07].

In this theory, one computes the time evolution of an observable  $Q(t)$  after an excitation induced by a small boost on the ground state  $|\Psi_0\rangle$

$$|\Psi(0)\rangle = e^{-i\epsilon\hat{Q}/\hbar}|\Psi_0\rangle.$$

The response  $Q(t)$  to this excitation can be decomposed into various frequencies  $\omega$ , giving the strength function

$$\begin{aligned} R_Q(\omega) &= \frac{-\hbar}{\pi\epsilon} \int_0^\infty dt Q(t) \sin(\omega t). \\ &= \sum_\alpha |\langle\alpha|\hat{Q}|\Psi_0\rangle|^2 \delta(\omega - \omega_\alpha) \end{aligned} \quad (2.1)$$

where  $\langle\alpha|\hat{Q}|\Psi_0\rangle$  is the transition amplitude between the ground state and the eigenstate  $|\alpha\rangle$  of the Hamiltonian and  $\hbar\omega_\alpha$  is their energy difference.

Fig. 2.2 gives an example for the octupole modes in  $^{208}\text{Pb}$ . An octupole boost is applied at initial time on the HF ground state of  $^{208}\text{Pb}$ . The latter has spin-parity  $J^\pi = 0^+$  and the boost induces a transition with  $\Delta L = 3$ , exciting vibrational states with  $J^\pi = 3^-$ . We can see on the left panel of Fig. 2.2 the oscillation of the octupole moment induced by the boost (solid red line). The associated strength function, shown in the right panel, exhibits a strong peak at an energy of  $\sim 3.4$  MeV. It corresponds to the main oscillation seen in the time evolution of  $Q_{30}(t)$ . Note

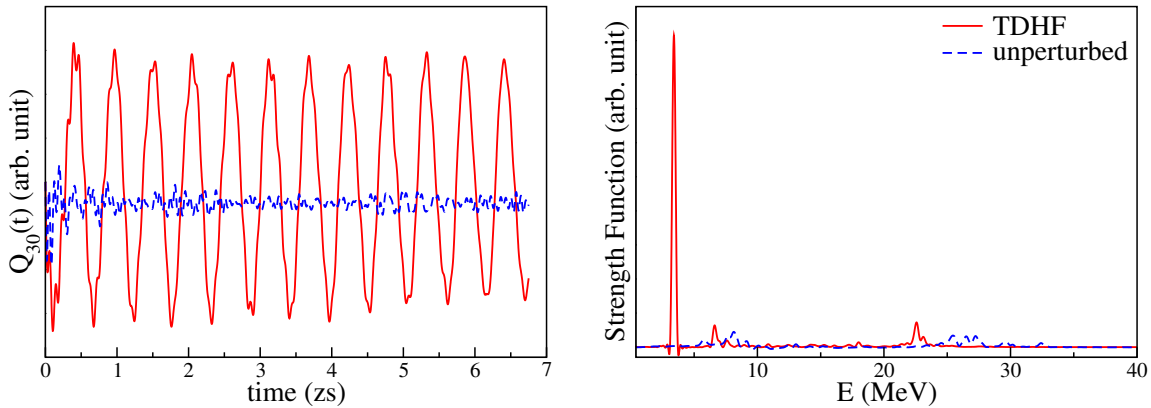


Figure 2.2: (left) Time evolution of the octupole moment in  $^{208}\text{Pb}$  after an octupole boost obtained with the TDHF3D code for both TDHF (solid line) and unperturbed (dashed line) responses (see text). (right) Associated strength function.

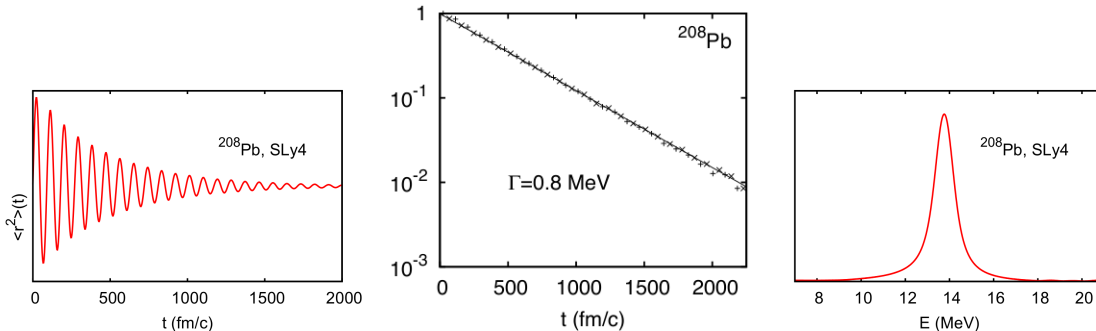


Figure 2.3: (left) Time evolution of the mean square radius in  $^{208}\text{Pb}$  after a monopole boost obtained with the TDHFBRAD code (without pairing). (middle) Time evolution of the oscillation amplitude (log scale). (right) Associated strength function. From Ref. [Ave09].

that this state is clearly bound, as can be seen from the undamped nature of the oscillation. This peak is associated to the low-lying  $3^-$  state in  $^{208}\text{Pb}$ . The energy of this state is overestimated with the SLy4 parametrisation of the Skyrme EDF, as the experimental value gives 2.6 MeV. However, its collective nature is unambiguous. This can be seen from a comparison with the unperturbed response of the same boost. The latter is obtained by freezing the mean-field in its initial HF value, i.e., neglecting the self-consistency of the mean-field in the dynamics. This procedure removes the residual interaction which is responsible for the collectivity of vibrations in TDHF (and RPA). We see that this peak disappears in the unperturbed spectrum, proving its collective nature.

Another example is shown in Fig. 2.3. Here, a monopole boost is applied on the

$^{208}\text{Pb}$  ground-state. The evolution has been obtained with a TDHF code<sup>2</sup> in spherical symmetry (allowing for large boxes) developed by B. Avez during his PhD [Ave09]. In this case, almost all the strength (if not all) goes into the GMR which is unbound. Such a resonance can then decay by particle emission. In particular, the direct decay induces an escape width. The latter is included in the TDHF framework thanks to evaporation of unbound components of the single particle wave functions [CGS87, PMB88, 3]. The decay induces an exponential decrease of the oscillation amplitude (see middle panel of Fig. 2.3). The corresponding escape width is  $\Gamma^\uparrow = 0.8$  MeV. This escape width is responsible for the main part of the width of the peak in the right panel of Fig. 2.3. Indeed, the total width of the peak is  $\Gamma^{tot.} \simeq 1.1$  MeV. The difference between the TDHF predictions of  $\Gamma^{tot.}$  and  $\Gamma^\uparrow$  could be attributed to Landau damping.

Experimentally, the energy of the GMR in  $^{208}\text{Pb}$  is [YLC<sup>+</sup>04]

$$E_{GMR}^{exp.} \equiv \frac{m_1}{m_0} = 14.0 \pm 0.2 \text{ MeV},$$

where the energy weighted moment  $m_k$  is defined as [RS80]

$$m_k = \sum_{\alpha} \omega_{\alpha}^k |\langle \alpha | \hat{Q} | \Psi_0 \rangle|^2, \quad (2.2)$$

$|\alpha\rangle$  denoting eigenstates of the Hamiltonian,  $|\Psi_0\rangle$  its ground-state, and  $\hat{Q}$  being the observable used in the excitation (here the monopole moment). This value is in excellent agreement with the TDHF result determined from the  $m_1/m_0$  ratio:  $E_{GMR}^{TDHF} \simeq 13.9$  MeV [Ave09]. However, the total width obtained from TDHF,  $\Gamma_{TDHF}^{tot.} \simeq 1.1$  MeV, underestimates the experimental value  $\Gamma_{exp.}^{tot.} = 2.9 \pm 0.2$  MeV [YLC<sup>+</sup>04]. This is due to the fact that TDHF does not take into account the spreading width (see Fig. 2.1 and the discussion in the introduction of this chapter). To go beyond and describe the spreading width, one would need to include the residual interaction. Calculations at the semi-classical level have indeed shown an increase of the damping thanks to the introduction of the collision term [SPS89].

## 2.3 Direct decay of giant resonances

Giant resonances usually lie above the proton and neutron emission thresholds. As mentioned above, their direct decay induces an escape width contributing to the total width of the GR. Such escape width can be studied with the TDHF formalism. Indeed, TDHF codes have been used in the past to investigate the direct decay of

---

<sup>2</sup>This is the TDHFBRAD code which solves the TDHFB equation. However pairing is neglected in this section.



Figure 2.4: Schematic description of the spatial repartition of numerical elements to compute spectra of emitted nucleons. The excited nucleus is in the center of a (spherical) box. Unbound parts of single-particle wave-functions are emitted in the continuum. The "detector" shows the region of space where the energy of the emitted wave functions is computed. Absorbing boundary conditions (ABC) are used to absorb particles leaving the detector and to avoid spurious reflection on the box boundary.

GMR [CGS87, PMB88]. In addition to its contribution to the escape width, GR direct decay is particularly interesting as it brings informations on the microscopic structure of the GR [HvdW01]. This is the main goal of the present study.

TDHF calculations of GR direct decay use large spatial grids to construct spectra of emitted nucleons with a good precision. It is then easier to use spherical TDHF codes, although it limits the applications to monopole vibrations only. Let us also introduce a numerical "detector" corresponding to the region of space where the energy of the emitted nucleons is computed from Fourier transform of their spatial wave function. This detector should be away from the center of the box to avoid any nuclear interaction of the emitted nucleons with the nucleus. Fig. 2.4 shows a schematic representation of this numerical setup. Absorbing boundary conditions (ABC) with an imaginary potential may be used to avoid any spurious interaction with particles reflected on the box boundary [NY05, RSA<sup>+</sup>06].

Fig. 2.5 shows an example of calculations of emitted nucleon spectra for the isovector GMR in  $^{40}\text{Ca}$ . The calculations have been performed with the same spherical code and simplified Skyrme EDF as in Ref. [37].

The left panel of Fig. 2.5 shows the proton spectra at different times. The first protons to reach the "detector" are obviously the fastest, i.e., with the highest kinetic energy. They also leave quickly the detector while slower protons reach it. Put together, these proton spectra form a spectrum<sup>3</sup>, shown in black thick solid line in the right panel of Fig. 2.5. The neutron spectrum is also shown (dashed line). The difference between proton and neutron separation energies in  $^{40}\text{Ca}$ , together with the absence of Coulomb barrier for neutrons explains the fact that the neutron spectrum shows a more important contribution at low energy than the proton one.

<sup>3</sup>This spectrum is defined by the maxima of the spectra obtained at different times.

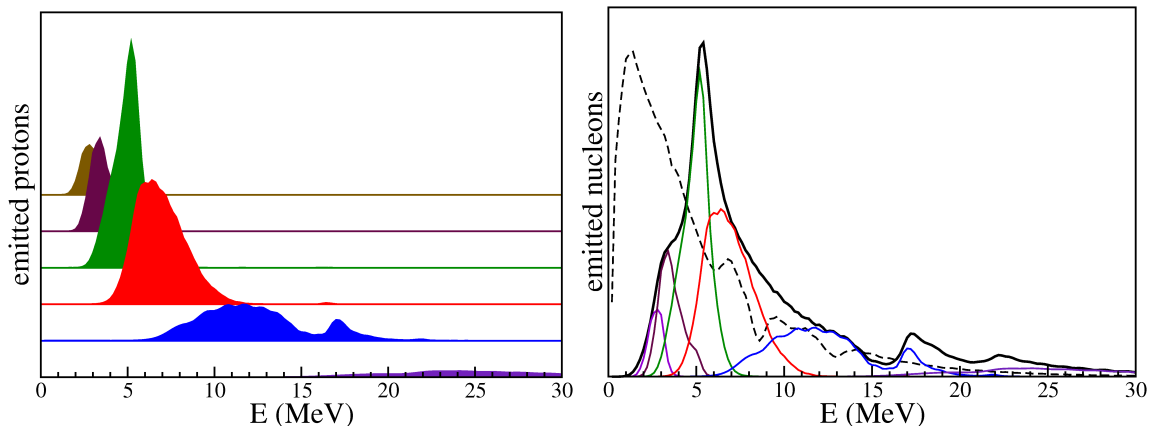


Figure 2.5: Spectra of protons in the "detector" (see text and Fig. 2.4) at different times following an isovector monopole boost in  $^{40}\text{Ca}$ . (left) Each spectrum is shifted vertically for clarity (time increases from bottom to top). The time delay between two consecutive spectra is  $\Delta T = 5$  zs. (right) The proton spectra at different times form an envelope (thick solid black line). The similar envelope obtained for neutron is also shown with a dashed line.

We can see in Fig. 2.5 that both proton and neutron spectra exhibit some structures which cannot be explained by a simple hydrodynamical model. Instead, one should seek for an explanation in terms of the microscopic structure of the GR. This motivated a more detailed investigation which was part of B. Avez's PhD work [Ave09] and which is describe in detail in Ref. [3].

A brief summary of the result for the GMR in  $^{16}\text{O}$  is presented here (see Ref. [3] for more details and for more results on tin isotopes). In this study, the TDHF-BRAD code [4] is used with the SLy4 parametrisation of the Skyrme EDF without pairing. Fig. 2.6 shows the time evolution (left) of the monopole moment after a monopole boost, and the associated spectrum (right) obtained within the linear response theory. The GMR spectrum exhibits structures which are associated to different single-particle orbitals. For instance, the high energy shoulder around 31 MeV is due to  $s_{1/2}$  particle-hole excitations<sup>4</sup>.

The spectra of emitted protons and neutrons are shown in the left panel of Fig. 2.7. The latter depend strongly on the associated single-particle quantum numbers. In particular, no  $s_{1/2}$  nucleons are emitted. This is due to the fact that the  $1s_{1/2}$  hole state is deeply bound (-32.4 MeV for protons and -36.2 MeV for neutrons according to the HF initial configuration [3]). In fact, the high energy shoulder of the GMR spectrum (see Fig. 2.6-right) does not have enough energy to bring the

<sup>4</sup>The monopole excitations is associated to a  $\Delta L = 0\hbar$  angular momentum transfer so that particle and hole have the same quantum numbers at the time of the excitation.

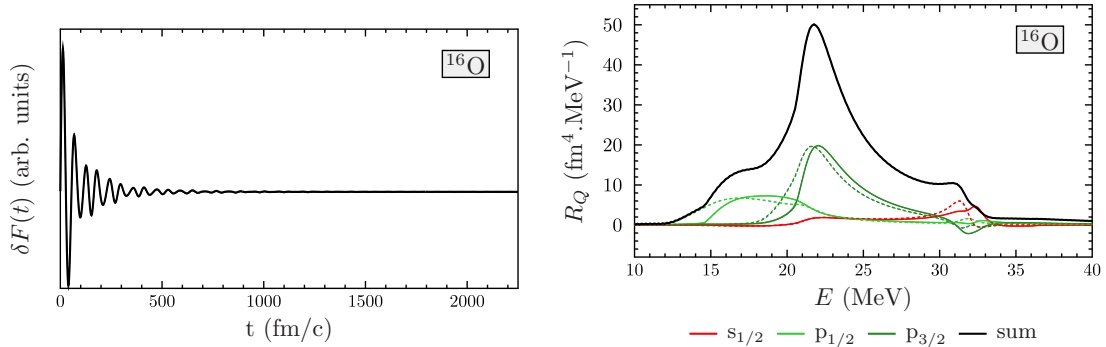


Figure 2.6: (left) Time evolution of the monopole moment in  $^{16}\text{O}$  after a monopole boost obtained with the TDHFBRAD code [4]. (right) Associated strength function and its decomposition onto single-particle quantum numbers  $l$  and  $j$  (spectroscopic notation). Solid (dashed) lines show neutron (proton) contributions.

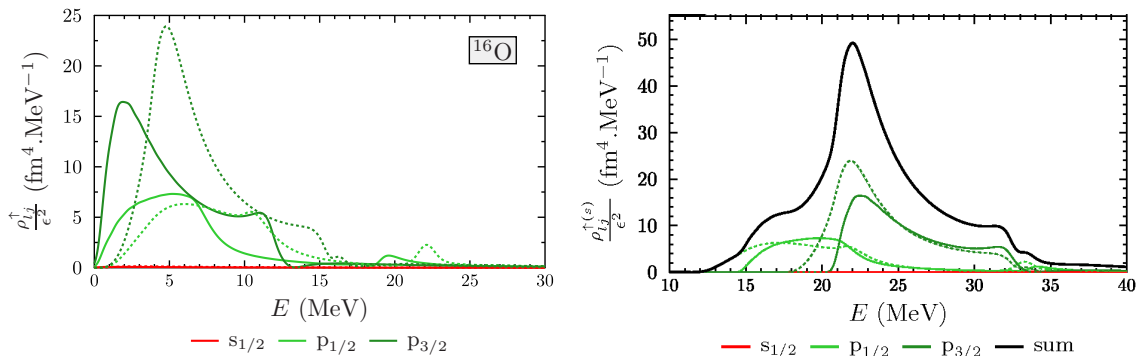


Figure 2.7: (left) Neutron (solid lines) and proton (dashed lines) direct-decay spectra. (right) Same spectra "shifted" by the energy of the initially occupied single-particle state. Their sum is shown in black solid line.

initial  $1s_{1/2}$  particle into the continuum.

The right panel of Fig. 2.7 shows the same quantity as the left panel, with a shift in energy (different for each  $l_j$  contribution) corresponding to the binding energy of the hole state. The sum of each shifted  $l_j$  contribution gives a spectrum which is very close to the GMR spectrum (compare with Fig. 2.6-right). The agreement is excellent for both the shape and the magnitude of the spectra. The origin of the structures in the direct emission spectra is entirely due to the shell structure of the nucleus.

It is also interesting to note that, although the high energy shoulder in the GMR spectrum is due to the excitation of a *bound*  $1p1h$  state, it appears in the "shifted" spectrum due to the *emission* of particles in  $p$ -states. In fact, the TDHF (or RPA) residual interaction is responsible for the coupling between the bound  $1p1h$   $s_{1/2}$  state

and unbound  $1p1h$   $p$ -states. As such, TDHF or continuum-RPA are good tools to investigate direct decay of vibrational modes. Note that similar couplings have been obtained in tin isotopes [3]. For instance, the GMR in  $^{100}\text{Sn}$  decays by protons only, while it is associated to a collective oscillation of both protons and neutrons.

Coincidence experiments between particles emitted in the GR decay and the ejectile resulting from the GR excitation process have been performed in the past to investigate GR properties [HvdW01]. The present theoretical analysis of GR direct decay is then interesting as it allows a direct comparison between theoretical and experimental spectra. However, for quantitative comparisons, one should use a more elaborated approach than the TDHF theory. Indeed, the fact that TDHF does not include  $2p2h$  residual interaction is a strong limitation, as the latter has been shown to be crucial to reproduce the width, the energy and the fragmentation of GR spectra [LAC04]. The present analysis of GR decay should then be repeated with, e.g., the extended-TDHF (ETDHF) or the time-dependent density-matrix (TDDM) approaches (see table 1.1 and Ref. [40]). Note also that calculations should be performed with 2D or 3D codes in order to study the decay of GR with higher multipolarity than the GMR.

## 2.4 Anharmonicity of giant resonances

In the harmonic picture, a GR is the first phonon eigenstate of an harmonic oscillator describing the collective motion, and corresponds to a coherent sum of  $1p1h$  states [BM75]. Experimental observations of 2 and 3-phonon states proved the vibrational nature of GR. However, they also showed the limit of the harmonic picture [CF95, ABE98, Sca04]. In particular, excitation probability of multi-phonon states was larger than predicted by the harmonic picture. This indicates that different phonon states may be coupled by the residual interaction [VCC<sup>+</sup>95, BD97, 32, FCA<sup>+</sup>03, 9, LCA<sup>+</sup>06, 33].

TDHF takes into account the effects of the residual interaction if the considered phenomenon can be observed in the time evolution of a one-body observable. In particular, the nonlinear response in TDHF contains the couplings between one- and two-phonon states coming from the  $3p1h$  and  $1p3h$  residual interaction [32]. In that sense, it goes beyond the RPA, which is a harmonic picture and contains only  $1p1h$  residual interaction.

We investigated in Ref. [32] the couplings leading to the excitation of a GMR or a GQR (resp. a GMR) on top of a GDR (resp. a GQR) using the nonlinear response to an external field in the TDHF theory. This work was part of my PhD thesis [25]. As a continuation to this work, we developed in Ref. [33] different techniques to compute

the matrix elements of the residual interaction responsible for these couplings.

These matrix elements can be written  $v_\mu = \langle \nu | \hat{V} | \nu\mu \rangle$  where the residual interaction  $\hat{V} = \hat{H} - \hat{H}_0$  is the difference between the full Hamiltonian  $\hat{H}$  and the HF+RPA Hamiltonian  $\hat{H}_0$ .  $|\nu\rangle$  and  $|\nu\mu\rangle$  are 1 and 2-phonon eigenstates of  $\hat{H}_0$  with eigenenergies  $E_\nu = E_0 + \hbar\omega_\nu$  and  $E_{\nu\mu} = E_0 + \hbar\omega_\nu + \hbar\omega_\mu$ , where  $\omega_{\nu,\mu}$  denote the collective frequencies and  $E_0$  is the ground state energy. The state  $|\nu\mu\rangle$  can be seen as one phonon of the GR  $\mu$  (e.g., a GQR) excited on top of one phonon of the GR  $\nu$  (e.g., a GDR).

In addition to the original technique based on the non-linearities of the time-dependent response [32], we introduced two other methods in Ref. [33]. A brief summary of these three methods is given below (see Ref. [33] for more details):

- *method 1*: A boost  $e^{-ik_\nu\hat{Q}_\nu}$  applied on the ground state induces, at lowest order in  $k_\nu$ , an oscillation of  $Q_\nu(t) = \langle \hat{Q}_\nu \rangle(t)$  linear in  $k_\nu$ , and an oscillation of  $Q_\mu(t)$  quadratic in  $k_\nu$  and proportional to  $v_\mu$ . Computing the response  $Q_\mu(t)$  to such a boost with TDHF gives then access to  $v_\mu$ .
- *method 2*: The same boost can be applied on a HF state obtained with a small constraint  $\lambda\hat{Q}_\mu$ . The linear response  $Q_\nu(t)$  oscillates then with a frequency  $\omega_\nu(\lambda)$ . The variation  $\frac{\partial\omega_\nu}{\partial\lambda}$  is proportional to  $v_\mu$ . Computing  $\frac{\partial\omega_\nu}{\partial\lambda}(\lambda=0)$  with a TDHF or deformed RPA code<sup>5</sup> gives also access to  $v_\mu$ .
- *method 3*: A "double" boost  $e^{-ik_\nu\hat{Q}_\nu}e^{-ik_\mu\hat{Q}_\mu}$  is applied on the ground state  $|0\rangle$ . Define the "coupling response function" as<sup>6</sup>

$$R_\nu^c(\omega) = \frac{-1}{\pi k_\nu k_\mu} \int_0^\infty dt \cos(\omega t) Q_\nu(t). \quad (2.3)$$

At lowest order in  $k_{\mu,\nu}$ , we can show that  $R_\nu^c(\omega)$  is proportional to  $v_\mu$  and exhibits peaks at  $\omega_\nu$  and  $|\omega_\nu \pm \omega_\mu|$  with opposite signs. The amplitude of these peaks provides a third way to extract  $v_\mu$ .

An illustration of the first method applied to the  $^{132}\text{Sn}$  nucleus with  $\nu \equiv \text{GDR}$  and  $\mu \equiv \text{GQR}$  is given in Fig. 2.8. On the left panel, we observe an oscillation of both the dipole and quadrupole moments, although the boost contains only the dipole moment. The oscillation of the quadrupole moment is in fact induced by the residual interaction. The right panel shows that, as expected, the amplitude of the dipole (resp. quadrupole) oscillation is linear (quadratic) in the boost velocity  $k_D$ . Numerical application gives a matrix element of the residual interaction

<sup>5</sup>This technique involves linear response only. The matrix element  $v_\mu$  can then be computed with a RPA code allowing initial deformations (generated by the constraint  $\lambda\hat{Q}$ ) of the vacuum.

<sup>6</sup>This function differs from the standard response function essentially by the cosine function instead of a sine function.

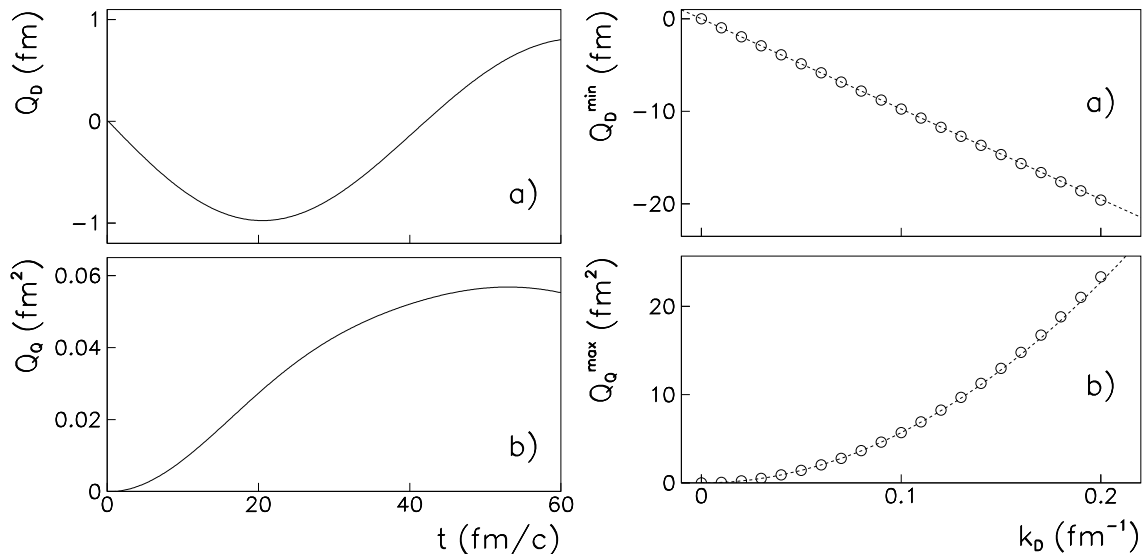


Figure 2.8: Left: Time evolution of the dipole (a) and quadrupole (b) moments in  $^{132}\text{Sn}$  after a dipole boost. Right: Circles indicate the first minimum and maximum of the dipole (a) and quadrupole (b) moment evolution, respectively, as a function of  $k_D$ . Dashed lines show linear and quadratic extrapolations at  $k_D \rightarrow 0$  of the dipole (a) and quadrupole (b) amplitudes, respectively.

$v_Q^{(1)} \simeq -0.61$  MeV. The two other methods give  $v_Q^{(2)} \simeq -0.56$  and  $v_Q^{(3)} \simeq -0.68$  MeV, respectively, showing a good agreement between the three methods [33].

Couplings have been computed in other tin isotopes [33] and in other nuclei ( $^{40}\text{Ca}$ ,  $^{90}\text{Zr}$ , and  $^{208}\text{Pb}$ ) with TDHF [32] and with a boson mapping method [FCA<sup>+</sup>03]. Refs. [32, FCA<sup>+</sup>03] also discuss couplings involving the GMR built on top of the GQR or the GDR. The TDHF results provide a confirmation to the amplitude of the couplings computed with the boson mapping method (see discussion in Ref. [32]).

Another conclusion of Ref. [33] is that there is no (or little) dependence of the coupling with isospin. However, an overall decrease of the coupling is obtained with increasing mass, showing that the couplings are mediated by the surface [32, FCA<sup>+</sup>03, 33].

Overall, the couplings are small but significant compared to the GR energies (e.g.,  $v/\omega \sim 5\%$  for  $^{132}\text{Sn}$ ). Their effect on the first phonon is negligible, but becomes sensible on the second and third phonon, with a typical shift in  $\hbar\omega$  of the order of  $\sim 0.5$  MeV as compared to the harmonic picture [FCA<sup>+</sup>03]. How the anharmonicities induced by these couplings affect the excitation probability to the multiphonon states have been investigated by Lanza *et al.* within a semiclassical coupled-channels formalism [LCA<sup>+</sup>06]. This model, based on the boson mapping method for the multi-phonon properties, allows for calculations of inelastic cross

sections for the multiple excitation of giant resonances induced by heavy-ion probes. Their calculations show that these anharmonicities induce an increase of the inelastic cross-section (as compared to the harmonic model) in the multi-phonon region, in good agreement with experimental data.

The role of pairing correlations, neglected so far, should also be considered. For instance, the fully self-consistent QRPA code with Gogny interaction and allowing for static deformations developed by S. Péru [PG08] will be used to obtain the couplings between the GQR and the GMR built on top of it. Couplings with exotic modes such as the pygmy dipole resonance [LCG<sup>+</sup>09] should also be investigated with the present methods.

## 2.5 Pairing dynamics

The TDHF calculations presented in the previous sections were applied to "normal" vibrations, i.e., vibrations of the one-body density (also called *normal* density)  $\rho(t)$  with matrix elements

$$\rho_{\alpha\beta}(t) = \langle \Psi(t) | \hat{a}_\beta^\dagger \hat{a}_\alpha | \Psi(t) \rangle. \quad (2.4)$$

In particular, these vibrations do not probe directly the pairing correlations between nucleons.

Inclusion of pairing is possible in the small amplitude limit with the quasiparticle-RPA (QRPA) based on HFB vacua. The HFB+QRPA has been widely used in nuclear structure studies [EBD<sup>+</sup>99, KSGVG02, FC05, PG08].

Similarly to the fact that TDHF is an extension to the HF+RPA, a natural extension of the HFB+QRPA is the time-dependent Hartree-Fock-Bogoliubov (TDHFB) theory [BR86]. In particular, the TDHFB theory provides a fully self-consistent<sup>7</sup> response to an external excitation including pairing dynamics and non-linearities.

The development of a realistic TDHFB spherical code with a full Skyrme EDF and a density-dependent pairing effective interaction was then initiated in 2006 by B. Avez during his PhD thesis. A first application to pairing vibrations was published in 2008 [4]. Recently, 3D codes have been developed to study pairing dynamics in nuclear systems at the BCS level [ENI<sup>+</sup>10, SLBW] and solving the TDHFB equation [SBMR11].

The present section introduces briefly the TDHFB formalism (see Ref. [40] for more details) and summarizes the results published in Ref. [4].

---

<sup>7</sup>Here, the self-consistency refers to the fact that the HFB vacuum and the residual interaction inducing the collective dynamics are derived from the same EDF.

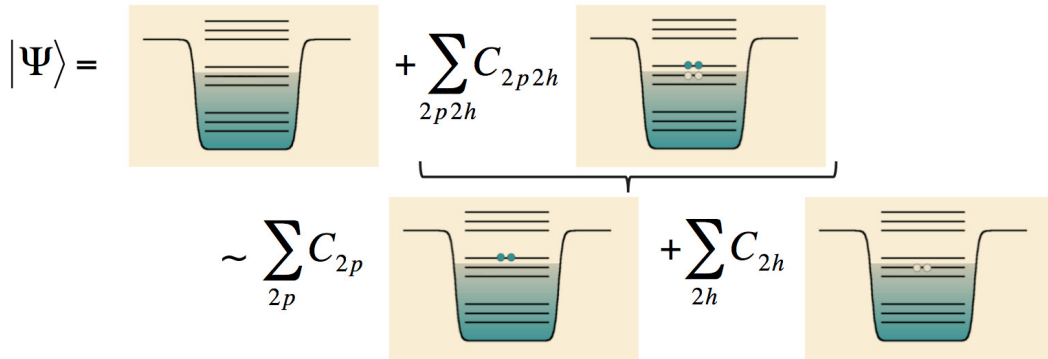


Figure 2.9: Illustration of the configurations used to generate a ground state with pairing correlations. up: exact case. bottom: BCS (or HFB) approximation.

### 2.5.1 The TDHFB theory

Pairing correlations are essentially due to an attractive short range contribution of the residual interaction in the  $^1S_0$  channel<sup>8</sup> [May50, DHJ03]. Pairing correlations affect then mostly (but not only) time-reversed states. The pairing residual interaction induces a scattering of a pair of nucleons across the Fermi surface. As a result, the ground-state with pairing correlations is a sum of  $2p2h$  states where the  $2p$  ( $2h$ ) are essentially time-reversed states. Such a state is represented schematically in the upper part of Fig. 2.9.

The treatment of pairing correlations in finite nuclei is simplified with the Bardeen-Cooper-Schrieffer (BCS) approximation initially developed to interpret superconductivity in metals [BCS57]. In this approximation, the  $2p2h$  states are replaced by a sum of  $2p$  and  $2h$  states (see bottom part of Fig. 2.9). The resulting approximation of the ground-state can then be written as a vacuum of quasiparticles, allowing for the application of the Wick theorem [RS80]. As a result, the BCS approximation leads to a *generalised* mean-field theory.

As we can see in Fig. 2.9, the "price to pay" is that the BCS ground-state is not an eigenstate of the particle number anymore. Pairing correlations are then included thanks to a gauge symmetry breaking. The Hartree-Fock-Bogoliubov (HFB) theory is more general but shares the same features with the BCS approach. In fact, it is an extension to the BCS theory where pairs are not limited to time-reversed states.

In the (TD)HFB theory, all the information on the state of the system is con-

<sup>8</sup>This notation means that the two nucleons are coupled to produce a total isospin 1, a total orbital angular momentum  $L = 0$  ( $S$ -wave), and a total spin 0.

tained in the *generalised* density matrix  $\mathcal{R}$  defined as

$$\mathcal{R} = \begin{pmatrix} \langle \hat{a}_j^\dagger \hat{a}_i \rangle & \langle \hat{a}_j \hat{a}_i \rangle \\ \langle \hat{a}_j^\dagger \hat{a}_i^\dagger \rangle & \langle \hat{a}_j \hat{a}_i^\dagger \rangle \end{pmatrix} = \begin{pmatrix} \rho & \kappa \\ -\kappa^* & 1 - \rho^* \end{pmatrix}, \quad (2.5)$$

where  $\kappa$  is the so-called *pairing tensor*.  $\kappa$  and  $\kappa^*$  contain the pairing correlations (at the HFB level).

The time evolution of the generalised density matrix is given by the TDHFB equation (see Ref. [40] for more details)

$$i\hbar \frac{d\mathcal{R}}{dt} = [\mathcal{H}, \mathcal{R}] \quad (2.6)$$

which has the same form than the TDHF equation 1.5. The generalised HFB Hamiltonian reads

$$\mathcal{H} \equiv \begin{pmatrix} h & \Delta \\ -\Delta^* & -h^* \end{pmatrix}, \quad (2.7)$$

where

$$h_{\mu\nu} = \frac{\delta\mathcal{E}[\rho, \kappa, \kappa^*]}{\delta\rho_{\nu\mu}} \quad \text{and} \quad \Delta_{\mu\nu} = \frac{\delta\mathcal{E}[\rho, \kappa, \kappa^*]}{\delta\kappa_{\mu\nu}^*} \quad (2.8)$$

are the HF Hamiltonian and the pairing field, respectively, and  $\mathcal{E}[\rho, \kappa, \kappa^*]$  is the EDF including pairing.

## 2.5.2 Application to pairing vibrations

Pairing vibrations are a particular manifestation of the dynamics of pairing correlations [BM75, RS80, BB66]. They are probed in two-nucleon transfer reactions [RP69, KSVGG04, PGB<sup>+</sup>11, SM11]. Pairing correlations are then expected to induce a collectivity which manifests itself as an increase of transition amplitude toward states associated to pairing vibrations. Starting with an even-even nucleus ground-state with  $A$  nucleons and spin-parity  $0^+$ , and assuming a  $\Delta L = 0$  direct pair transfer reaction, pair vibration states with  $J^\pi = 0^+$  are populated in the  $A + 2$  (pair addition) and/or  $A - 2$  (pair removal) nuclei.

Such a process can be simulated within the TDHFB formalism using an initial boost with a Hermitean pair-transfer operator [BB66]

$$\hat{F} = \int d\mathbf{r} f(r) \left( \hat{a}_{\mathbf{r},\downarrow}^\dagger \hat{a}_{\mathbf{r},\uparrow}^\dagger + \hat{a}_{\mathbf{r},\uparrow} \hat{a}_{\mathbf{r},\downarrow} \right), \quad (2.9)$$

where the arrows label the spin of the single-particles (we omit the isospin to simplify the notation). In the present application,  $f(r)$  is a Fermi-Dirac spatial distribution

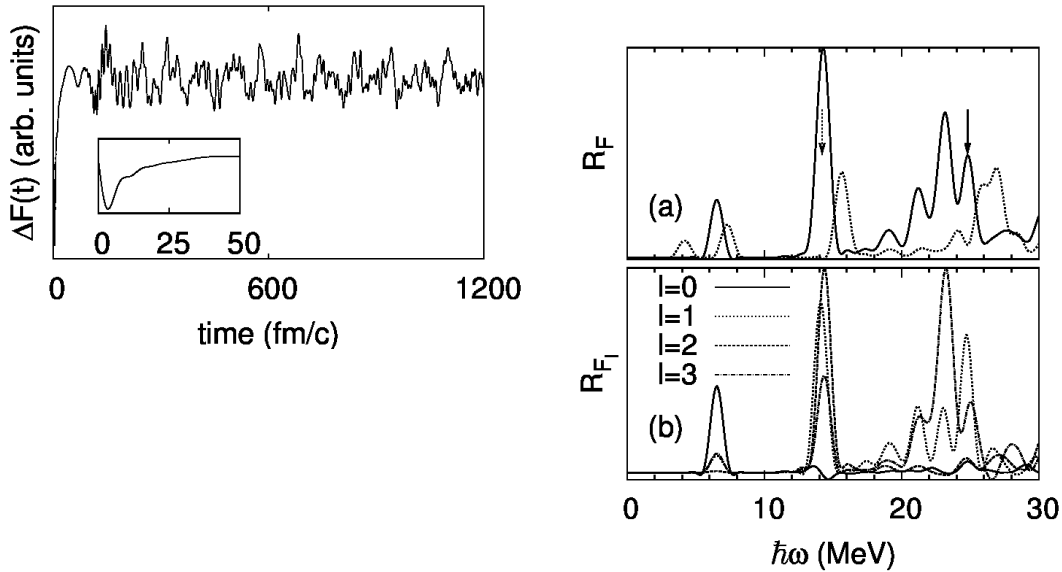


Figure 2.10: (left) Evolution of  $\langle F \rangle(t)$  after a pair transfer type excitation on  $^{18}\text{O}$ . The inset shows the same quantity at early times. (top-right) Associated TDHFB strength function (solid) compared with the unperturbed spectrum (dashed). The arrows indicate pair removal transition from the  $1p_{3/2}$  (solid) and  $1p_{1/2}$  (dotted) deep hole states. (bottom-right) TDHFB strength function decomposed into single-particle orbital angular momentum  $l$ -components.

containing the nucleus and cutting at 4 fm outside the nucleus. Its role is to remove unphysical high energy modes associated to pair creation outside of the nucleus.

In this approach, it is assumed that the spectroscopy of the  $A - 2$ ,  $A$  and  $A + 2$  nuclei can be obtained from the same quasiparticle vacuum (the  $A$  ground-state). Note that recent improvements have been proposed by Grasso *et al.* where this limitation is overcome for ground-state to ground-state transitions by using different vacua for the parent and daughter ground-states [GLV].

The TDHFBRAD code has been developed by B. Avez to solve the TDHFB equation in spherical symmetry with a full Skyrme EDF and density-dependent pairing effective interaction. As a first application, the linear response of  $\langle \hat{F} \rangle(t)$  has been computed in several oxygen and calcium isotopes [4]. The time-evolution of  $\langle \hat{F} \rangle(t)$  is shown in the left panel of Fig. 2.10 for a  $^{18}\text{O}$  vacuum. The apparent chaotic behaviour of  $\langle \hat{F} \rangle(t)$  is due to the simultaneous excitation of several pair vibrations, as we can see from the strength function (solid line) in the top-right panel. Both pair additional and pair removal (indicated by the arrows) modes are present. A comparison with the unperturbed strength function (dashed line) obtained by removing the self-consistency of the generalised mean-field shows two features in the TDHFB spectra:

- an increase of the strength,
- and a lowering of the transition energies.

Both are compatible with the attractive nature of the dynamical pairing residual interaction. In particular, the increase of the strength is a clear signature for collective effects. Note that similar conclusions were drawn from continuum QRPA calculations by Khan *et al.* [KSVGG04].

The bottom-right panel of Fig. 2.10 shows a decomposition of the response in terms of single-particle orbital angular momentum  $l$ . Together with the structure of the initial HFB vacuum, this decomposition allows for an understanding of each peak in terms of their main particle and hole contributions. See Ref. [4] for a detailed microscopic analysis. See also Refs. [4, 1] for an analysis of other nuclei (oxygen, calcium and tin isotopes).

This first realistic application of the TDHFB theory to nuclear systems has confirmed previous QRPA calculations of pairing vibrations [KSVGG04]. Future applications of the TDHFBRAD code to study the role of pairing dynamics on normal vibrations and their decay, and to investigate non-linear effects in pairing dynamics are envisaged. The recent development of a 3D TDHFB code [SBMR11] opens also new perspectives for the study of  $L \neq 0$  vibrations.

## 2.6 Conclusions and perspectives

Real time mean-field calculations have been performed to investigate collective vibration properties. The response to an external excitation has been obtained with 3D and spherical TDHF codes and associated strength functions have been computed within the linear response theory.

Direct decay of GR have been analysed from energy spectra of emitted nucleons. Within the TDHF approach, the latter contains enough information to reconstruct the strength function if the hole structure of the nucleus is known. A comparison between the microscopic decompositions of the strengths obtained from the time response of the excitation operator and from the emitted nucleon spectra shows that the residual interaction couples bound  $1p1h$  states with unbound ones, allowing for particle emission in the continuum.

Non linear vibrations were also studied within the TDHF framework. They are used to quantify the coupling between one GR phonon and two (different) GR phonon states. The large values of the couplings which have been obtained in different nuclei confirm that these kind of couplings is a probable source of the anharmonicities observed in GR multiphonon experiments.

Our last work concerned the inclusion of pairing correlations in the mean-field dynamics. To that purpose, a realistic spherical TDHFB code has been built and applied to the study of pairing vibrations excited in pair-transfer reactions. Comparisons with unperturbed calculations showed that the dynamical pairing residual interaction included in TDHFB is attractive and induces some collectivity to the pairing vibrations.

Several possible extensions to these works have already been discussed, such as the study of non-linear vibrations and particle decay with pairing, and the study of  $L \neq 0$  vibrations with 3D TDHFB codes.

Other perspectives could be considered.

In the present studies, we focused on collective motion at zero temperature, in particular vibrations built on top of the ground state. The role of finite temperature on collective motion (e.g., the so-called "hot GR") has been widely discussed in the nuclear physics community [BBB98]. Questions such as the effect of temperature on pairing dynamics and on the couplings between GR multiphonon states could be addressed with an extension of the present calculations to finite temperature systems. TDHF studies of giant resonances at finite temperature are indeed possible [VTV87] starting from an initial hot HF solution [BLV84]. In the next chapter, we also discuss the particular case of GDR excited in the fusion of two nuclei.

Recently, it has been shown with a molecular dynamics approach that GR in light nuclei ( $^{12}\text{C}$ ,  $^{16}\text{O}$ ,  $^{24}\text{Mg}$ ) were also affected by  $\alpha$ -clustering [FHG<sup>+</sup>10]. In particular, these  $\alpha$ -clusters induce new vibrational modes which could couple to GR producing a new source of anharmonicity.

The calculations presented in this chapter and the possible perspectives discussed above are based on a (generalised) mean-field approach. For a more realistic comparison to experimental data, extensions to theories going beyond the (generalised) one-body limit are mandatory, in particular to reproduce the GR energies, fragmentations and widths [LAC04]. Possible approaches include extended-TDHF [LCA98], second RPA [DNSW90, LMvNC<sup>+</sup>00], time-dependent density matrix theory [Toh01, TU02, WC85], or stochastic one-body transport theory [RS92, LAC01, JC02]. Although they all face their own technical difficulties, these approaches could benefit from the recent increase of computational power.

# Chapter 3

## Heavy-ion collisions

The previous chapter dealt with small amplitude vibrations. We now investigate the collision of two atomic nuclei which is by nature a large amplitude collective motion. In contrast to the precedent chapters, part of the work reported in this chapter is experimental, although the main contribution is theoretical.

We first start in section 3.1 by describing some motivations to study heavy-ion collisions.

The outcome of a heavy-ion collision depends essentially on few properties of the entrance channel: energy, masses, angular momentum, deformation and orientation,  $N/Z$  asymmetry, and internal structure (e.g., magicity). Thus, we discuss different reaction mechanisms and their dependence on entrance channel properties. In sections 3.2, 3.3, 3.4, and 3.5, we present studies on fusion, transfer, deep-inelastic, and quasi-fission reactions, respectively. In section 3.6 we present a theoretical study of actinide collisions. Note that only a brief summary of each study is given, in particular when more details can be found in the associated publications. Finally, we conclude and give some perspectives.

### 3.1 Motivations

There are several motivations to achieve a good understanding of heavy-ion reaction mechanisms. Two of them are particularly relevant to the work presented in this chapter:

- To investigate quantum phenomena with complex systems,
- To optimize the production of specific nuclei.

Some examples are also discussed below.

### 3.1.1 Unique perspectives brought by the nuclear case to study quantum phenomena

A huge difference between the quantum treatment of a macromolecule, such as a fullerene, and an atomic nucleus is their interaction with their environments. Indeed, large molecules interact strongly with the surrounding gas and photon bath, while a system of colliding nuclei is free of such interactions. This is because (i) nuclei do not interact with most photons in nature due to their small size (few fm), and (ii) nuclear excited states have much longer lifetimes ( $\sim 10^{-18}$  s) than typical reaction times in heavy-ion collisions<sup>1</sup> ( $< 10^{-20}$  s). Being entirely isolated during the reaction, heavy-ion collisions could then be considered as ideal to investigate the role of the composite nature of nuclei on quantum processes such as tunnelling<sup>2</sup>.

As an example, one of the most striking signatures of quantum phenomena in nuclear collisions is the coherent quantum superposition of reaction channels leading to fusion barrier distributions [DHRS98] which are interpreted within the coupled-channel framework [HRK99]. Fusion via tunnelling is effectively a powerful microscope, magnifying quantum effects in nuclear collisions through the exponential dependence of tunnelling probability on the potential, which is modified by quantum coherent effects.

### 3.1.2 Production of specific nuclear systems: case of the heaviest nuclei

Stellar nucleosynthesis has produced a great variety of nuclei thanks to various reaction mechanisms. Of course all that remains on Earth are the stable and very long-lived by-products of these reactions, and in order to perform experimental nuclear studies, these must serve as our starting points. The internal structure of nuclei is of considerable interest in their own right and we can use the nuclei left by nature to create others, like new super-heavy elements (SHE) or isotopes which may or not be produced at the far end of the astrophysical r-process [LMPPT11].

Transfermium nuclei are of great interests for our understanding of the quantum nature of the nuclear many-body problem as most of them are stable against fission thanks to quantum shell effects only. In particular, an island of stability is predicted in the super-heavy region with  $Z = 114 - 126$  and  $N = 172 - 184$  (see, e.g.,

---

<sup>1</sup>This point is crucial. Indeed, if an excited state decays by  $\gamma$ -emission during the collision, then the state of the environment changes from the vacuum  $0\gamma$ -state to  $1\gamma$ -state. If such an emission occur, the system of nucleons would then be strongly coupled to its environment.

<sup>2</sup>If the system was not isolated from its environment, then decoherence would occur and the system would have a classical behaviour[JZK<sup>+</sup>03].

Ref. [BRR<sup>+</sup>99] for mean-field calculations).

The discovery of SHE is important for various fundamental research fields:

- *Astrophysics*: Does the r-process reach the super-heavy island of stability, or does it stop with spontaneous fissile lighter nuclei (see, e.g., [LMPPT11])?
- *Atomic physics and chemistry*: Relativistic effects on the electrons play a role on the atomic structure of SHE. As a result, SHE chemical properties may deviate from the standard classification suggested by the Mendeleiev table (see, e.g., [Eic07, Gäg11]).
- *Nuclear physics*: The precise location of the island of stability at the top of the nuclear chart would constrain the theoretical models (see, e.g., [BF99]).

The most important breakthrough in the quest for SHE came from heavy-ion fusion-evaporation reactions [HM00]. Elements up to  $Z=118$  have been produced with this technique [Oga06]. However, the cross-sections for the production of SHE in their ground state are extremely small. The smallest cross-section measured is 30 femtobarns (fb) with the production of two  $Z = 113$  nuclei, after more than half-year irradiation of  $^{209}\text{Bi}$  targets with  $^{70}\text{Zn}$  beam [Mor07].

Two main factors are hindering SHE formation by fusion:

- The quasi-fission mechanism strongly dominates [Boc82, Tök85, She87]. It leads to a fast re-separation of the projectile and target-like fragments after an exchange of nucleons from the heavy fragment to the light one.
- In case of fusion and formation of a compound nucleus at finite energy, the survival probability against fission is very small due to the small fission barriers of SHE.

A summary of the heaviest nuclei, most of them produced artificially on Earth, is given in Fig. 3.1. All transfermiums formed by fusion of stable nuclei are neutron-deficient. As a consequence, nothing is known about  $\beta$ -stable or neutron-rich transfermiums.

There are three possible mechanisms which could produce neutron-rich transfermium nuclei and, then, get closer to the island of stability: (*i*) a rapid neutron capture process, (*ii*) fusion with neutron-rich nuclei, and (*iii*) multi-nucleon transfer in actinide collisions. Neutron fluxes in nuclear reactors are not sufficient to use (*i*). A critical limitation of the upcoming exotic beam facilities is the beam intensities, without which the feasibility of (*ii*) is questionable. However, the process (*iii*), which is discussed in Sec. 3.6, seems promising. The main advantages of using actinides are:

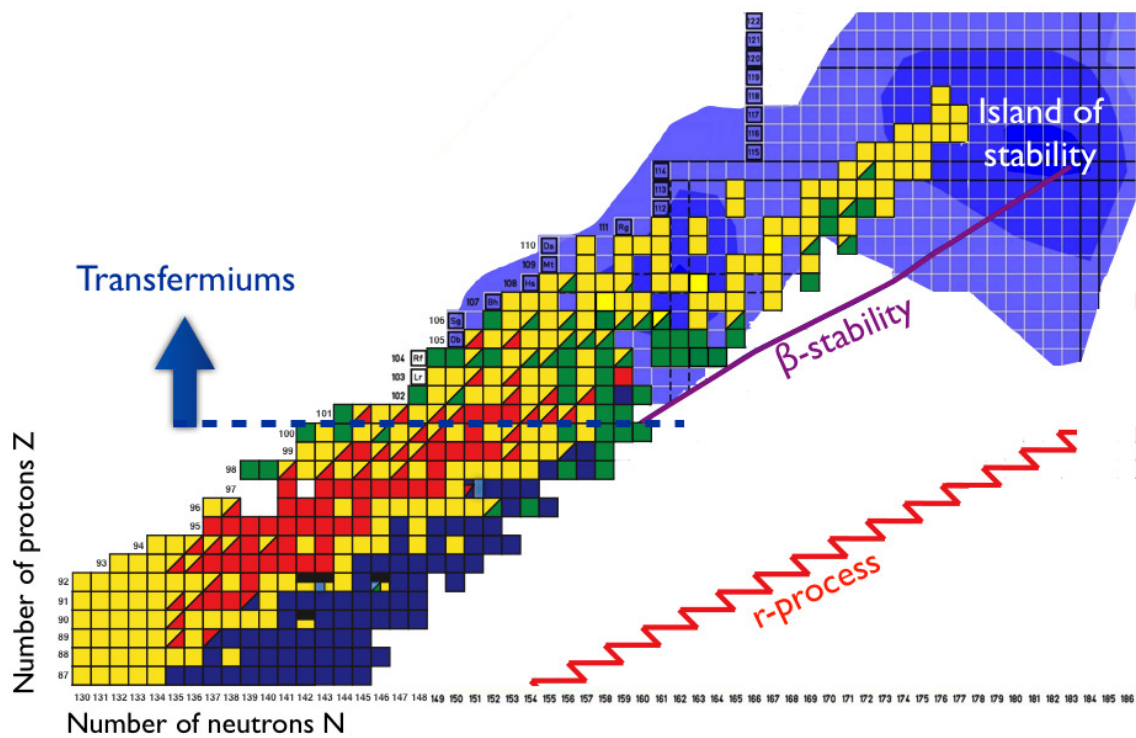


Figure 3.1: Upper part of the nuclear chart. The dark blue area indicates quantum shell correction energy leading to more bound, and then more stable nuclei, according to a microscopic-macroscopic approach [San97]. The purple line shows the expected  $\beta$ -stability line. The expected path followed by the r-process is shown with a red line.

- They exist in nature (e.g.,  $^{238}\text{U}$ ) or are easy to produce as radioactive targets (e.g.,  $^{248}\text{Cm}$ ).
- They have 50% more neutrons than protons, which is crucial for the production of new isotopes along the  $\beta$ -stability line.

## 3.2 Fusion in medium mass systems

Dynamical mean-field theories like TDHF are well suited to the study of low-energy reaction mechanisms, such as fusion at energies around (but above) the barrier. Indeed, at low energies, the Pauli principle blocks collisions between nucleons, increasing their mean-free path to the order of the size of the nuclear system. In addition, fusion occurs by transferring relative motion into internal excitation via one-body mechanisms well treated by TDHF.

Early TDHF codes have been successfully applied to describe above-barrier fusion reaction in light systems [BGK78]. However, these calculations also predicted a lower limit to the angular momentum for fusion. For smaller angular momenta, a "transparency" was observed in the calculations (two fragments are emitted along the collision axis). This prediction was never confirmed experimentally. In fact, it was shown by Umar and collaborators that this so-called "fusion-window" problem was in fact solved with the inclusion of the spin-orbit interaction [USR86]. Indeed, the latter was shown to be an important source of dissipation in heavy-ion collisions.

Modern TDHF calculations are now performed with a full Skyrme EDF including spin-orbit terms [KOB97, MRS<sup>+</sup>05, NY05, UO05, SFdlM09].

The first observable we propose to study with the TDHF3D code is the capture threshold between two nuclei. We consider here systems with  $Z_1 Z_2 < 1600$  to avoid the well known fusion hindrance observed in very heavy systems<sup>3</sup>. We also discuss above barrier fusion cross-sections, and investigate the path to fusion from the charge equilibration process.

### 3.2.1 Fusion of spherical nuclei: the example of the $^{16}\text{O} + ^{208}\text{Pb}$ system

A reference barrier could be obtained in the frozen approximation<sup>4</sup> with the same Skyrme EDF. The FROZEN code allows for calculations of nucleus-nucleus potentials in the frozen approximation using the same routines as the TDHF3D code for the field

---

<sup>3</sup>The latter is discussed in section 3.5.

<sup>4</sup>In the frozen approximation, the collision partners are assumed to have the density of their ground-state during the approach.

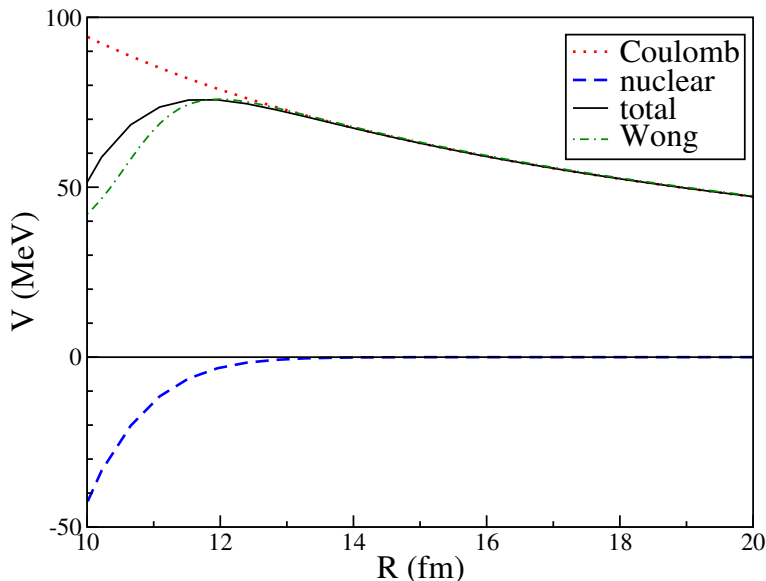


Figure 3.2: Nucleus-nucleus potentials obtained with the frozen approximation in the  $^{16}\text{O}+^{208}\text{Pb}$  system. Nuclear (dashed blue line) and Coulomb (dotted red line) contributions, and their sum (solid line) have been obtained with the FROZEN code. For comparison, the Wong potential [Won73] is shown in green dot-dashed line. The latter is obtained with a potential depth  $V_0 = 70$  MeV, a potential diffuseness  $a = 0.48$  fm, and nuclear radii  $R_i = 1.25A_i^{1/3}$  fm.

and the spatial derivatives. Nucleus-nucleus potentials are computed by translating the nuclei in their HF state [29].

An example is shown in Fig. 3.2 for the  $^{16}\text{O}+^{208}\text{Pb}$  system which could be considered as a benchmark in low energy reaction studies (see, e.g., Refs. [VGG<sup>+</sup>77, TNLS89, MBD<sup>+</sup>99, DHDT<sup>+</sup>07, 11, 26]). A comparison with the Wong formula [Won73] is shown. We see that, although the potential heights agree, differences appear at short distances. In fact, inside the barrier, the parametrisations of nucleus-nucleus potentials are less constrained by experimental data. In addition, the frozen approximation neglects the Pauli principle between the nucleons of different collision partners, which may affect the inner barrier region.

The height of the barrier obtained with the frozen approximation<sup>5</sup> is  $V_B^{\text{frozen}} \simeq 76.0$  MeV. This value is close to the barrier obtained with the Wong formula [Won73],  $V_B^{\text{Wong}} \simeq 75.9$  MeV, while it is 1 MeV smaller than the Bass barrier [Bas77],  $V_B^{\text{Bass}} \simeq 77.0$  MeV. All these barriers overestimate the experimental value obtained from the centroid of the barrier distribution (see Fig. 3.3)  $V_B^{\text{exp.}} \sim 74.5$  MeV.

To investigate the possible role of dynamical effects on the fusion barrier, the latter has been computed with the TDHF3D code. Because the TDHF theory does

<sup>5</sup>The same value has been obtained, independently, by Washiyama *et al.* [WL08].

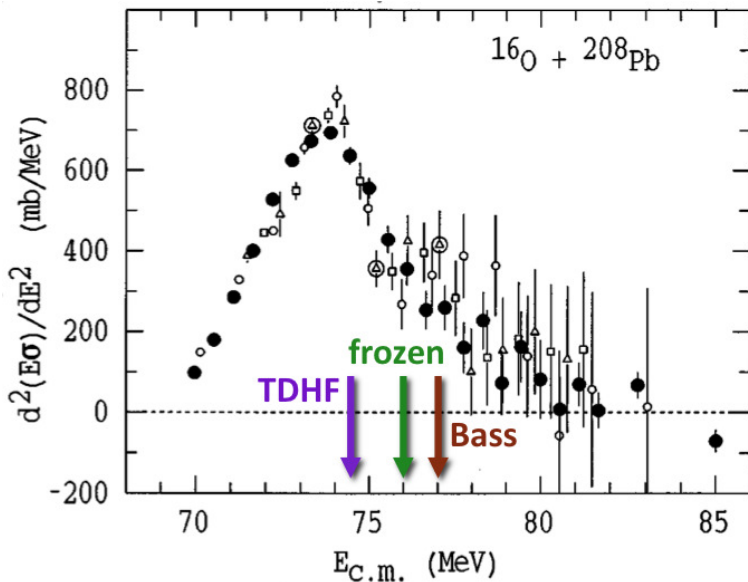


Figure 3.3: Experimental fusion barrier distribution of the  $^{16}\text{O}+^{208}\text{Pb}$  system from Ref. [MBD<sup>+</sup>99]. The frozen, Bass and TDHF barriers (see text) are shown with arrows.

not allow for quantum tunnelling of the many-body wave function, the TDHF fusion barrier can be identified as the capture threshold for central collisions, above which a compound system is formed and below which two fragments are emitted. Due to the finite time of the TDHF evolutions, one has to define a maximum computational time<sup>6</sup> above which the final configuration (i.e., one compound system or two fragments) is assumed to be reached.

Figure 3.4 shows the evolution of the relative distance between fragment centers of mass in central  $^{16}\text{O}+^{208}\text{Pb}$  collisions at different energies around the capture threshold. We clearly identify two sets of trajectories associated to capture (fusion) and to re-separation of the fragments. These calculations predict a fusion threshold of  $V_B^{TDHF} = 74.445 \pm 0.005$  MeV. As a result, the dynamical effects included in TDHF calculations lower the barrier by  $\sim 1.5$  MeV for this system. Note that these TDHF calculations seem to precisely describe the position of the fusion barrier while no parameter of the Skyrme EDF has been adjusted on reactions.

To get a deeper insight into these dynamical effects, the density evolutions at  $E_{c.m.} = 74.44$  and  $74.45$  MeV are plotted in Fig. 3.5. In the first case, the composite system seems to "hesitate" to fuse. It forms a "di-nuclear" system for relatively long time ( $\sim 500$  fm/c) before re-separating. In the second case, the system overcomes the fusion barrier. More generally, the two figures illustrate the richness of physi-

<sup>6</sup>This time may depend on the system. For medium mass systems such as  $^{16}\text{O}+^{208}\text{Pb}$ , a typical time of  $10^3$  fm/c (1 zs=300 fm/c) is used.

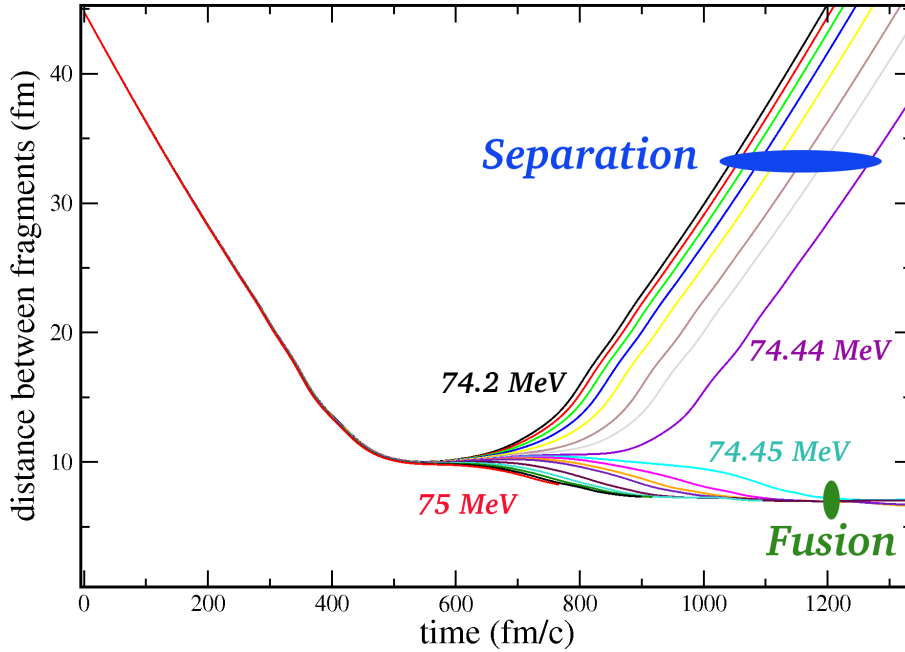


Figure 3.4: Relative distance between fragments as a function of time for head-on  $^{16}\text{O}+^{208}\text{Pb}$  reactions computed with the TDHF3D code.

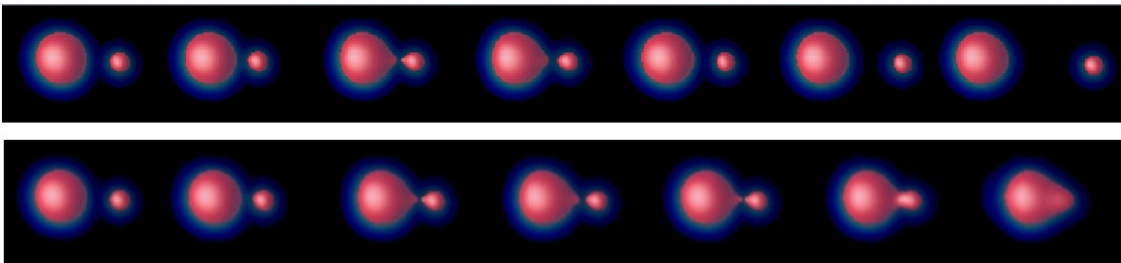


Figure 3.5: Top: Density evolution for the reaction  $^{16}\text{O}+^{208}\text{Pb}$  corresponding to a head-on collision at a center of mass energy  $E_{c.m.} = 74.44$  MeV (just below the fusion barrier). The red surfaces correspond to an iso-density half of the saturation density ( $\rho_0/2 = 0.08 \text{ fm}^{-3}$ ). Each figure is separated by a time step of 135 fm/c. Bottom: Same at  $E_{c.m.} = 74.45$  MeV, i.e., just above the fusion threshold.

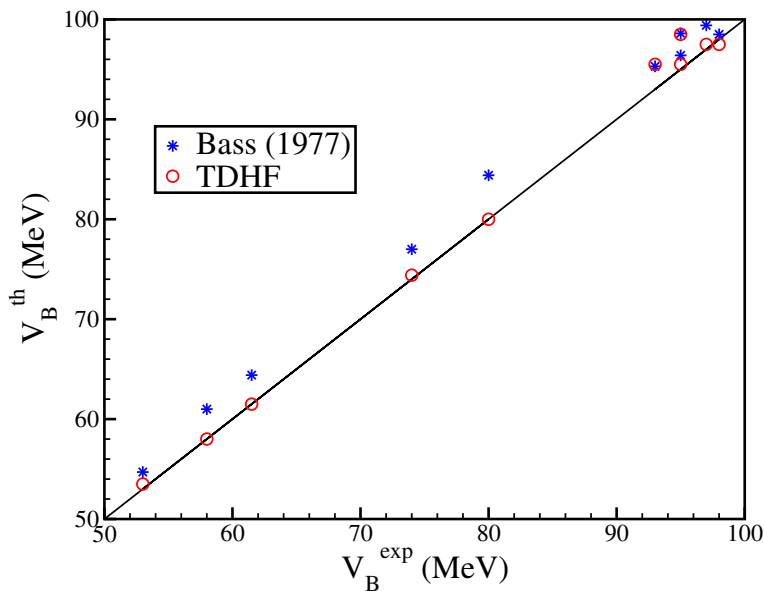


Figure 3.6: Bass barriers [Bas77] (stars) compared to barriers extracted from TDHF calculations (circles) as a function of experimental barriers (centroids of fusion barrier distributions).

cal phenomena contained in TDHF calculations: surface diffusivity, neck formation at early stage of the fusion process, quadrupole/octupole shapes of the compound system...

The observed lowering of the fusion barrier due to dynamical effects could be partly explained by a coupling of the relative motion to a transfer mechanism [28]. In fact, the outgoing channel of  $^{16}\text{O}+^{208}\text{Pb}$  at  $E_{c.m.} = 74.44$  MeV (see top of Fig. 3.5) is, in average,  $^{14}\text{C}+^{210}\text{Po}$ . This two-proton transfer channel effectively lowers the barrier by decreasing  $Z_1Z_2$  and, then, the Coulomb repulsion. Transfer reactions in the  $^{16}\text{O}+^{208}\text{Pb}$  system are discussed in more details in section 3.3. Note that low-lying collective vibrations, such as the first  $3^-$  state in  $^{208}\text{Pb}$  (see Fig. 2.2) also affect the fusion barrier distribution [MBD<sup>+</sup>99].

We also performed systematic calculations of fusion barriers for other medium mass systems involving spherical nuclei [28]. A summary of the results is shown in Fig. 3.6. A good reproduction of distribution barrier centroids has been obtained (better than the Bass parametrisation) for all the studied systems. Other calculations with the TDHF3D code confirmed its predictive power for the determination of fusion barriers [WL08].

In Ref. [28], we also calculated fusion cross-sections at above barrier energies for the  $^{16}\text{O}+^{208}\text{Pb}$  system. The fact that fusion probabilities are either 0 or 1 implies

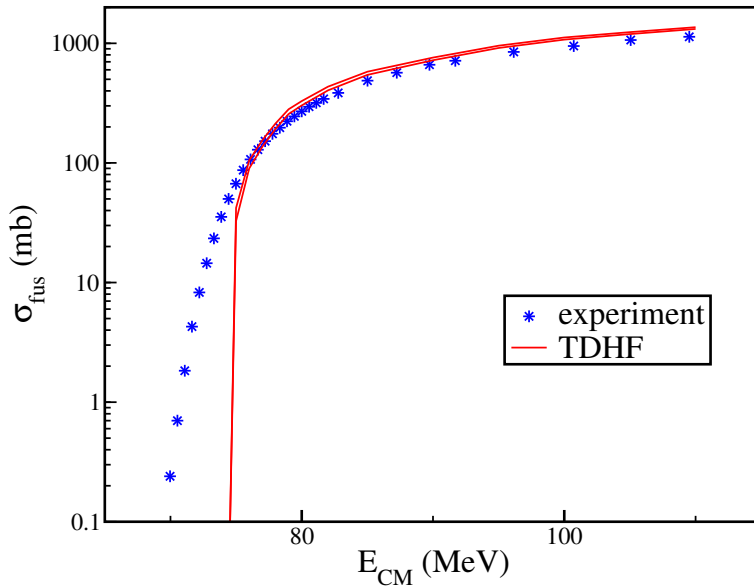


Figure 3.7: Experimental fusion cross sections from Ref. [MBD<sup>+</sup>99] (stars) compared to cross sections deduced from TDHF calculations (lines) of  $^{16}\text{O}+^{208}\text{Pb}$  collisions. The two lines correspond, respectively, to lower and upper limits of theoretical cross sections.

that cross sections are obtained using the "quantum sharp cutoff formula" [Bla54]

$$\sigma_{fus}(E) = \frac{\pi \hbar^2}{2\mu E} [l_{max}(E) + 1]^2, \quad (3.1)$$

where the fusion probability is 0 for  $l > l_{max}(E)$ . To avoid discontinuities due to the integer values of  $l_{max}(E)$ ,  $[l_{max}(E) + 1]\hbar$  is generally approximated by its semi-classical equivalent  $\mathcal{L}_c = \sqrt{2\mu E} b_c$ . The latter corresponds to the classical angular momentum threshold for fusion and  $b_c$  denotes the maximum impact parameter below which fusion takes place [Bas80]. This replacement is justified by the fact that  $(l_{max} + 1)^2$  and  $\mathcal{L}_c^2/\hbar^2$  are both greater than  $l_{max}(l_{max} + 1)$  and lower than  $(l_{max} + 1)(l_{max} + 2)$ . Accordingly, we finally obtain the standard classical expression for fusion cross sections  $\sigma_{fus}(E) \simeq \pi \mathcal{L}_c^2/2\mu E = \pi b_c^2$ .

The results are shown in Fig. 3.7 for the  $^{16}\text{O}+^{208}\text{Pb}$  system. Fusion cross-sections are overestimated by about 16% above the barrier. Although this discrepancy is small for a theory which has no parameter adjusted on reaction mechanisms, its origin is unclear.

Finally, the calculations are not able to reproduce the sub-barrier energies. This is of course one of the main drawbacks of the TDHF approach. The inclusion of quantum tunnelling of the many-body wave function is clearly one of the biggest challenges in the microscopic treatment of low-energy nuclear reactions.

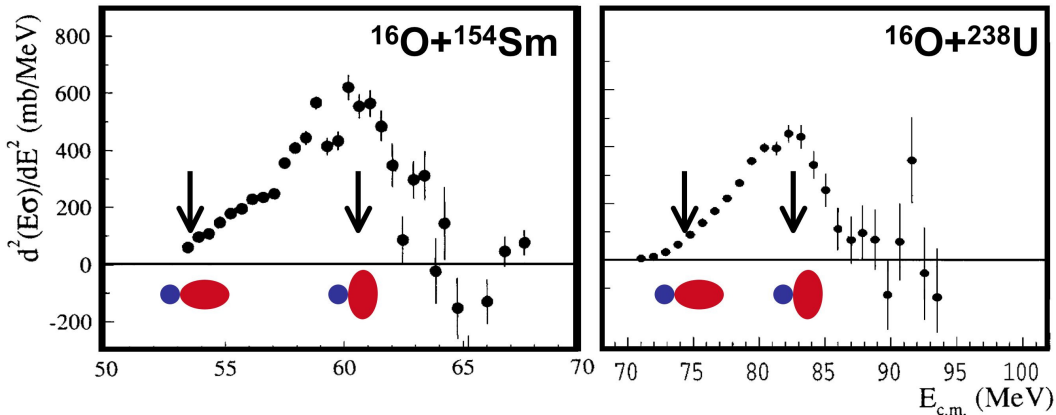


Figure 3.8: (left) Experimental barrier distributions for  $^{16}\text{O}+^{154}\text{Sm}$  [LDH<sup>+</sup>95]. (right) Same for the  $^{16}\text{O}+^{238}\text{U}$  system [HDL<sup>+</sup>96]. The arrows indicate the barriers obtained from TDHF calculations for two extreme configurations. From Ref. [28].

### 3.2.2 Fusion barriers with a deformed nucleus

We now consider collisions of a spherical nucleus on a deformed one. In such a case, the barrier depends on the orientation of the deformed nucleus at the touching point, leading to a wider barrier distribution than the single barrier case [DHRS98, RSS91].

Fig. 3.8 shows two examples of experimental barrier distributions involving a prolaty deformed heavy target [LDH<sup>+</sup>95, HDL<sup>+</sup>96]. Such barrier distributions are usually well reproduced in the framework of coupled channel calculations [DHRS98]. Their usual interpretation is that the low (resp. high) energy part of the barrier distribution corresponds to collisions with the tip (side) of the deformed nucleus. In Ref. [28], we confirmed this interpretation with TDHF calculations presented by arrows in Fig. 3.8.

We conclude that, in addition to a good reproduction of the centroid, modern TDHF calculations also reproduce the width of the barrier distributions generated by a static deformation of a heavy target without any adjustment of parameters.

As a continuation of a part of my PhD work, the case of a light deformed projectile on a heavy spherical target has been investigated in Ref. [35] both within the TDHF approach and within the coupled channel frameworks with the code CCFULL [HRK99]. For such systems, the barrier distribution is affected by the re-orientation of the deformed nucleus in the Coulomb field of the target. This induces an anisotropy of the orientation axis distribution and results into a fusion hindrance at low energies [35]. This is what we observe in Fig. 3.9 where the results of CCFULL calculations are shown for the  $^{24}\text{Mg}+^{208}\text{Pb}$  system<sup>7</sup> without (solid line) and with

<sup>7</sup>The  $^{24}\text{Mg}$  exhibits a static prolate deformation in its ground state.

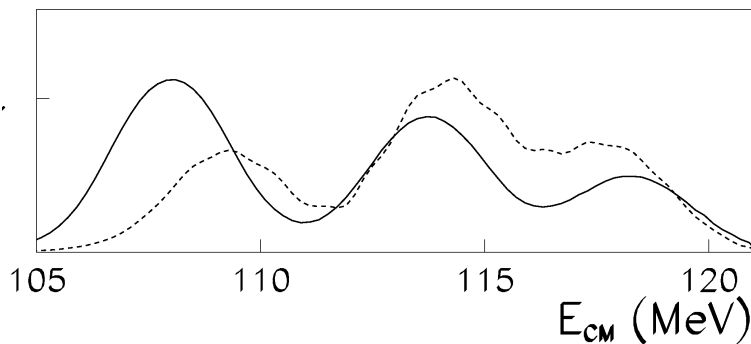


Figure 3.9: Barrier distribution for the reaction  $^{24}\text{Mg}+^{208}\text{Pb}$  obtained with the CCFULL code without (solid line) and with Coulomb coupling up to a distance of 241 fm (dashed line). Adapted from Ref. [35].

(dashed line) reorientation due to the long range Coulomb interaction.

Possible experimental evidences of this effect have been reported [NCS<sup>+</sup>07]. Note that the reorientation is proportional to  $A_{\text{spherical}}/A_{\text{total}}$  and then does not affect the systems studied in Fig. 3.8. Note also that, although it is a Coulomb effect, the reorientation does not depend on the charges of the nuclei but on their masses only [35].

Finally, it is worth mentioning that, although TDHF calculations help to understand the structure of fusion barrier distributions, they would not be able to reproduce their detailed structure (e.g. the peaks in Fig. 3.9) due to a lack of quantum effects associated to the collective degrees of freedom. In particular, the state of the deformed nucleus should be a coherent superposition of different orientations in the laboratory frame. This quantum coherence is lost at the mean-field level. A possible improvement would be to restore this coherence using a time-dependent generator-coordinate method (TDGCM), using the orientation of the nucleus as a collective coordinate [RCG83].

### 3.2.3 Charge equilibration in fusion

As a continuation to part of my PhD work and to the work published in Ref. [34], we investigated the process of charge equilibration in above-barrier fusion reactions. The results have been published in Ref. [36].

Charge equilibration occurs when two nuclei with different  $N/Z$  collide. This difference induces a net dipole moment at contact which can oscillate. This isovector dipole oscillation is also called preequilibrium GDR, as it is a collective motion occurring in the preequilibrium stage of the compound system, i.e., before a complete equilibration of its degrees of freedom. This mechanism has been investigated with TDHF calculations [BN81, 34, 36] as well as semi-microscopic approaches [SPS89,

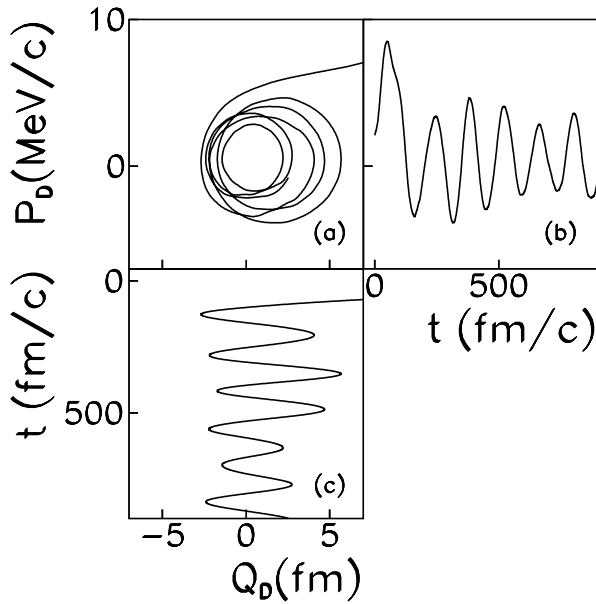


Figure 3.10: Evolution of the expectation value of the dipole moment  $Q_D$  and its conjugated moment  $P_D$  in the case of the  $N/Z$  asymmetric reaction  $^{40}\text{Ca}+^{100}\text{Mo}$  at a center-of-mass energy of 0.83 MeV/nucleon.

CTS93, BBCDT01].

An example of such preequilibrium dipole motion is shown in Fig. 3.10, where the time evolution of the dipole moment  $Q_D$  (proportional to the distance between the proton and neutron centers of mass) and its conjugated moment  $P_D$  (proportional to their relative velocity) are shown in the case of the  $N/Z$  asymmetric reaction  $^{40}\text{Ca}+^{100}\text{Mo}$  [36].  $P_D$  and  $Q_D$  oscillate in phase quadrature, and, then, exhibit a spiral in the plot of  $P_D$  as a function of  $Q_D$ .

It is possible to compute the spectrum of  $\gamma$  emitted by the preequilibrium GDR using laws of classical electrodynamics. Such a  $\gamma$ -spectrum is shown in the bottom-right of Fig. 3.11 (solid-line, purple area). A comparison with the first chance statistical GDR  $\gamma$ -ray decay spectrum, shows that the preequilibrium GDR  $\gamma$  are emitted at lower energy. This is interpreted in terms of a large deformation of the compound nucleus in its preequilibrium phase [34, 36].

Experimental  $\gamma$ -spectra are shown in the left panel of Fig. 3.11 for the  $^{40}\text{Ca}+^{100}\text{Mo}$   $N/Z$  asymmetric reaction and for the  $^{36}\text{S}+^{104}\text{Pd}$  reaction which is quasi-symmetric in  $N/Z$ . Only the first reaction is expected to exhibit a preequilibrium dipole motion. Indeed, more  $\gamma$  are observed in this reaction. The difference (purple area in left panel of Fig. 3.11) is interpreted in terms of  $\gamma$ -decay from the preequilibrium GDR [Fli96]. This preequilibrium GDR  $\gamma$ -spectrum is shown in the top-right panel of Fig. 3.11. The energy of the peak is in good agreement with the spectrum com-

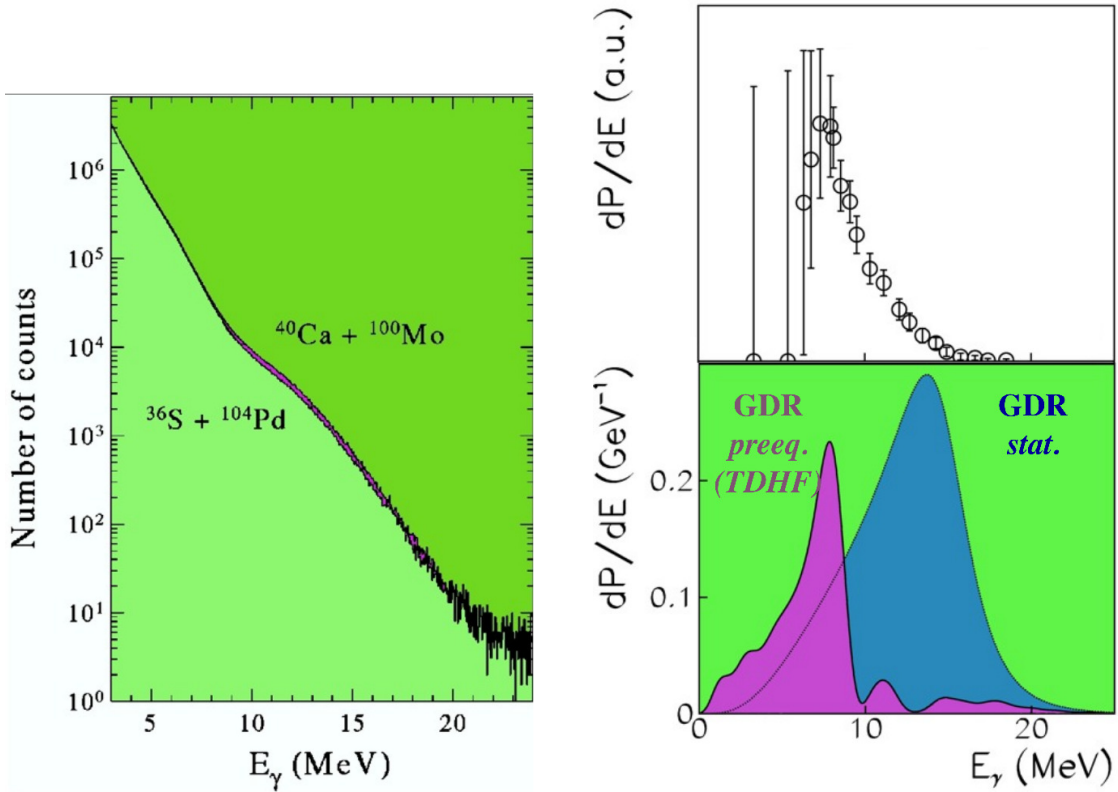


Figure 3.11: (left)  $\gamma$ -spectra measured in the  $^{40}\text{Ca}+^{100}\text{Mo}$  and  $^{36}\text{S}+^{104}\text{Pd}$  reactions at a center-of-mass energy of 0.83 MeV/nucleon [Fli96]. (right-top) Preequilibrium GDR  $\gamma$ -decay spectrum obtained from the difference between the two  $\gamma$ -spectra in the left. (right-bottom) Theoretical  $\gamma$  spectrum computed from the preequilibrium dipole moment evolution in Fig. 3.10 (solid line, purple area). The dotted line represents the first chance statistical  $\gamma$ -ray decay spectrum (blue area). Adapted from [36].

puted from the TDHF response. We interpret this lowering of the preequilibrium GDR energy, by comparison to the hot GDR, as a signature of a strong deformation of the preequilibrium nucleus. In particular, this means that the shape equilibration is much slower than the charge equilibration. We will discuss charge equilibration times more quantitatively in section 3.5.

To conclude, we see that the preequilibrium GDR contains informations on the structure of the preequilibrium compound system and, then, on the path to fusion. Here, we discussed the example of deformation. In Refs. [34, 36], we also use the preequilibrium GDR to investigate other properties of the path to fusion, such as the role of rotation, the coupling with collective shape vibrations, the role of mass asymmetry... We also proposed that the decay of a preequilibrium GDR could serve as a cooling mechanism increasing the survival probability of the heaviest compound nuclei [36]. This effect still needs experimental investigations.

### 3.3 Transfer reactions

We discussed in section 3.2.1 the interplay between fusion and transfer reactions in the  $^{16}\text{O}+^{208}\text{Pb}$  system around the barrier. In particular, we observed just below the barrier (see bottom of Fig. 3.5) an average transfer of two protons. We now discuss such transfer reactions in heavy-ion collisions.

First, we present some results published in Ref. [26], where the transfer reactions in the  $^{16}\text{O}+^{208}\text{Pb}$  system was investigated from a theoretical point of view. Then, we compare with the results of Ref. [11] where the same reaction has been studied experimentally<sup>8</sup>. Other experiments with the  $^{6,8}\text{He}$  exotic beams are also briefly discussed [24, 8, 22, 23].

Several recent attempts of describing nucleon transfer in heavy-ion collisions within the TDHF framework have been made in medium mass systems [UOM08, 28, WAL09, 40, 26, YALW11]. Indeed, the TDHF equation describe the evolution of single-particle wave-functions. The latter, initially localised within one collision partner, may be partially transferred to the other fragments during the collision, as illustrated in Fig. 3.12

A signature of transfer is given by the change of average particle number of the fragment after a collision. Figure 3.13 gives the evolution of the expectation value of  $\hat{Z}$  and  $\hat{N}$  of the small fragment in the exit channel of  $^{16}\text{O}+^{208}\text{Pb}$  sub-barrier central collisions. At the barrier,  $\sim 2$  protons and no neutron, in average, are transferred (see also bottom of Fig. 3.5), while at  $\sim 10\%$  below the barrier, the average  $N$  and  $Z$  of the projectile are obtained, indicating a dominance of (in)elastic scattering.

---

<sup>8</sup>I was involved in the theoretical interpretation of the results of this experiment.

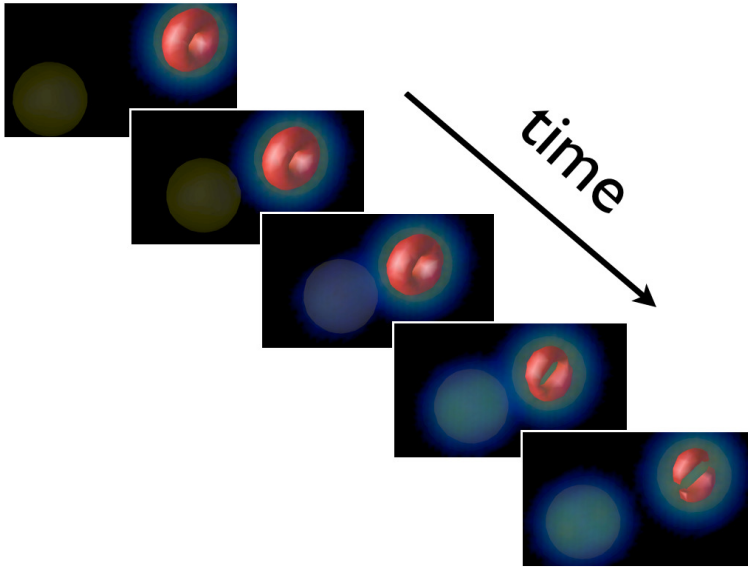


Figure 3.12: TDHF calculations of central sub-barrier collision of two  $^{16}\text{O}$  nuclei. The nuclei approach each other, and re-separate back-to-back due to the Coulomb repulsion. The evolution of one single-particle belonging initially to the nucleus in the right is shown. After the collision, part of this wave function has been transferred to its collision partner. Since this reaction is symmetric, a similar transfer occurs from the left to the right, and both fragments have the same particle number distributions.

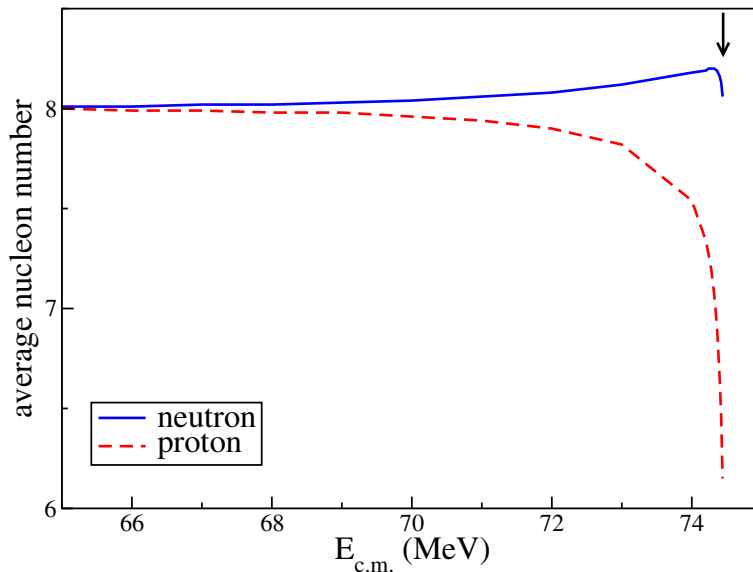


Figure 3.13: Transfer below the barrier in  $^{16}\text{O}+^{208}\text{Pb}$  sub-barrier central collisions. The average number of protons and neutrons of the small fragment in the exit channel are plotted as a function of  $E_{c.m.}$ . The arrow indicates the TDHF fusion barrier.

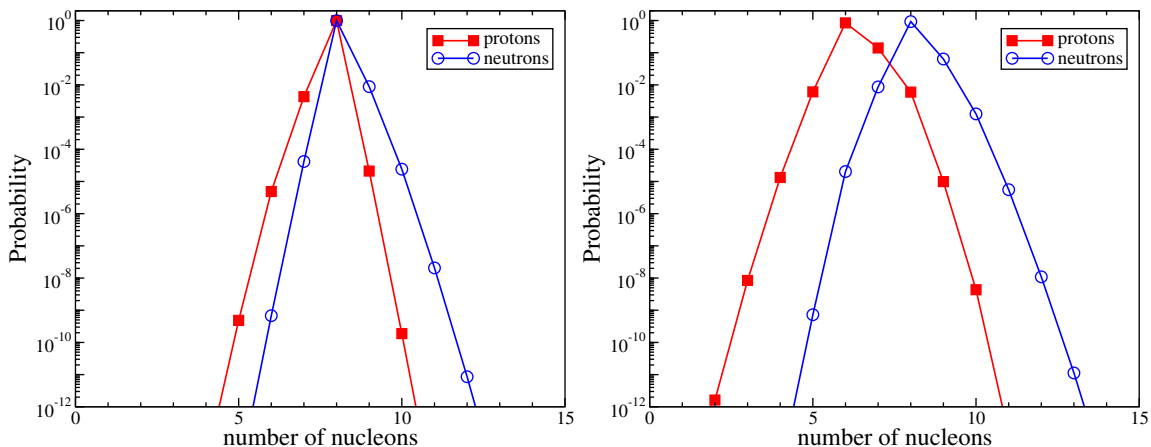


Figure 3.14: Neutron (circles) and proton (squares) number probability distributions of the lightest fragment in exit channel of a head-on  $^{16}\text{O}+^{208}\text{Pb}$  collision at  $E_{c.m.} = 65$  MeV (left) and 74.44 MeV (right) computed with the TDHF3D code. Adapted from Ref. [26].

We see that the probability for proton stripping (transfer from the light to the heavy nucleus) is higher than for proton pickup (transfer from the heavy to the light nucleus), while neutron pickup is more probable than neutron stripping. This qualitative observation is in agreement with experimental data [VGG<sup>+</sup>77, 11].

To get a deeper insight into this transfer mechanism, the transfer probabilities are extracted at the TDHF level thanks to a projection onto a good particle number technique<sup>9</sup> applied on the fragments<sup>10</sup> (see Ref. [26] for details).

Fig 3.14 shows the resulting transfer probabilities at (right) and well below (left) the barrier. As expected from the average values (see Fig. 3.13), the most probable channels are  $Z = N = 8$  well below the barrier, and  $Z = 6, N = 8$  at the barrier.

A standard representation of experimental sub-barrier energy transfer data is to plot transfer probabilities as a function of the distance of closest approach  $R_{min}$  between the collision partners [CPS09].  $R_{min}$  is computed assuming a Rutherford trajectory [BW91]:

$$R_{min} = Z_1 Z_2 e^2 [1 + \text{cosec}(\theta_{c.m.}/2)] / 2E_{c.m.} \quad (3.2)$$

where  $\alpha$  is the center of mass scattering angle.

<sup>9</sup>This technique is standard in beyond-mean-field models for nuclear structure when the number of particles is only given in average [RS80].

<sup>10</sup>One could question this approach as the TDHF wave functions are not used for the calculation of expectation values of one-body operators. In particular, the width of the distributions should be underestimated [DDP79]. However, as we will see in section 3.4, the TDHF and BV widths are similar for non violent collisions such as sub-barrier transfer.

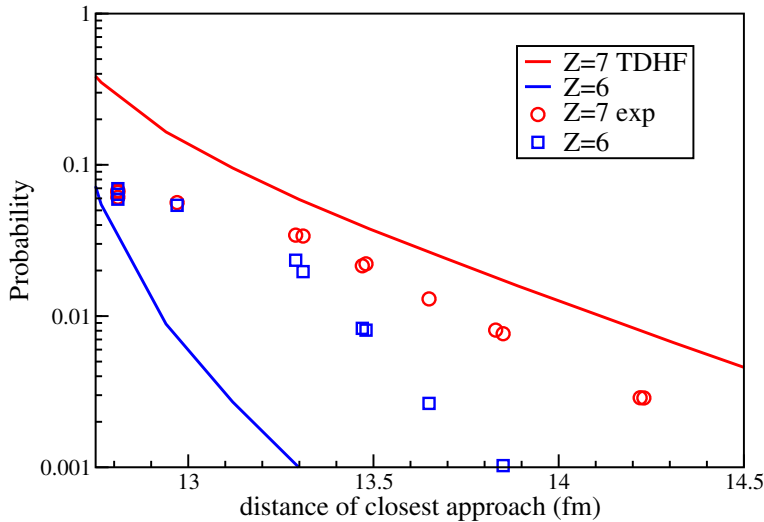


Figure 3.15: Proton number probability distribution as function of the distance of closest approach obtained with TDHF (lines). Experimental data are taken from Ref. [11].

A comparison with recent data from Ref. [11] is shown in Fig. 3.15 for sub-barrier one and two-proton transfer channels. We see that TDHF overestimates the one-proton transfer probabilities and underestimates the 2-proton transfer channel. We interpreted this discrepancy as an effect of pairing interactions [26, 11]. For  $R_{min} > 13$  fm, however, the TDHF calculations reproduces reasonably well the sum of one and two proton transfer channels<sup>11</sup> [26].

The study of transfer reactions is also a very active field with weakly bound nuclei beams. In this case, the continuum affects the reaction channels by allowing for break-up reactions. An experimental campaign<sup>12</sup> has been carried on with SPIRAL exotic helium beams to study such effects at GANIL [24, 8, Lem09, 22, 23]. In the first experiment, projectile like fragments were detected in coincidence with  $\gamma$ -rays with the EXOGAM detector array. Large neutron transfer cross sections were obtained with  ${}^6\text{He}$  beams, and were found to be larger than those for breakup [24]. This measurement was repeated with an additional neutron detector in order to distinguish between  $1n$  and  $2n$  transfer channels. It was shown that the main contribution to transfer arises from the  $2n$  component, thereby indicating the dominance of the dineutron structure<sup>13</sup> in  ${}^6\text{He}$  [8].

<sup>11</sup>For  $R_{min} < 13$  fm, sub-barrier fusion, not included in the TDHF calculations, reduces transfer probabilities and the agreement is less good [26, 11].

<sup>12</sup>The first experiment (Ref. [24]) was my PhD experiment. I also participated to a following experiment (Refs. [8, 22, 23]).

<sup>13</sup>The dineutron configuration corresponds to the two close neutrons by opposition to the cigare configuration where they are on both side of the nucleus.

These studies emphasize the role of pairing interactions in heavy-ion collisions for both stable and exotic beams. The recent inclusion of pairing interactions in 3D microscopic codes [AL09, ENI<sup>+</sup>10, SBMR11] gives hope in our ability to describe such data with more details in a near future. The inclusion of the pairing residual interaction will also be crucial to understand the effect of correlations between weakly bound neutrons on reaction mechanisms.

Finally, microscopic theories should also be used to determine, not only the transfer probabilities, but also the excitation energy of the final fragments. In particular, this would be of great help to understand how transfer reactions induce an energy dissipation, possibly hindering fusion at deep sub-barrier energies [DHDT<sup>+</sup>07, 11].

### 3.4 Deep-Inelastic Collisions

Deep-Inelastic Collisions (DIC) occur essentially well above the barrier. The main characteristics of DIC exit channels are:

- A strong damping of the initial kinetic energy,
- Large fluctuations of the fragment proton and neutron numbers around their initial value,
- An angular distribution of the fragments following a  $1/\sin\theta_{c.m.}$  behaviour<sup>14</sup>.

Early TDHF calculations were able to reproduce fragment kinetic energies, mean masses, and scattering angles, however they failed to reproduce the observed large fluctuations of the fragment  $Z$  and  $N$  distributions [KDMR<sup>+</sup>77, DMRKN78]. This failure was seen as a necessity to include a collision term. However, Balian and Vénéroni showed that the calculation of such fluctuations were in fact outside the range of applications of the TDHF formalism [BV81], and that one should use Eq. 1.39 instead [BV84].

Prior to Ref. [27], the BV prescription was applied to particle number fluctuations in DIC by Bonche and Flocard [BF85], Marston and Koonin [MK85], Broomfield and Stevenson [Bro09], and within a semi-classical approximation by Zielinska-Pfabé and Grégoire [ZPG88]. Comparing with standard TDHF calculations, these works showed indeed an increase of the fluctuations. However, the first realistic calculations allowing for a direct comparison with experimental data<sup>15</sup> was only recently performed in Ref. [27]. We now present the main results of this paper.

<sup>40</sup>Ca+<sup>40</sup>Ca collisions at  $E_{c.m.} = 128$  MeV ( $\sim 2.4$  times the barrier height) have been studied with the TDHF3D code. Fig. 3.16(left) shows density plots obtained

---

<sup>14</sup>This behaviour is due to a large orbiting of the fragments at contact. All  $\theta_{c.m.}$  are then equiprobable. However the emission is not isotropic as it occurs in the collision plane. As a result,

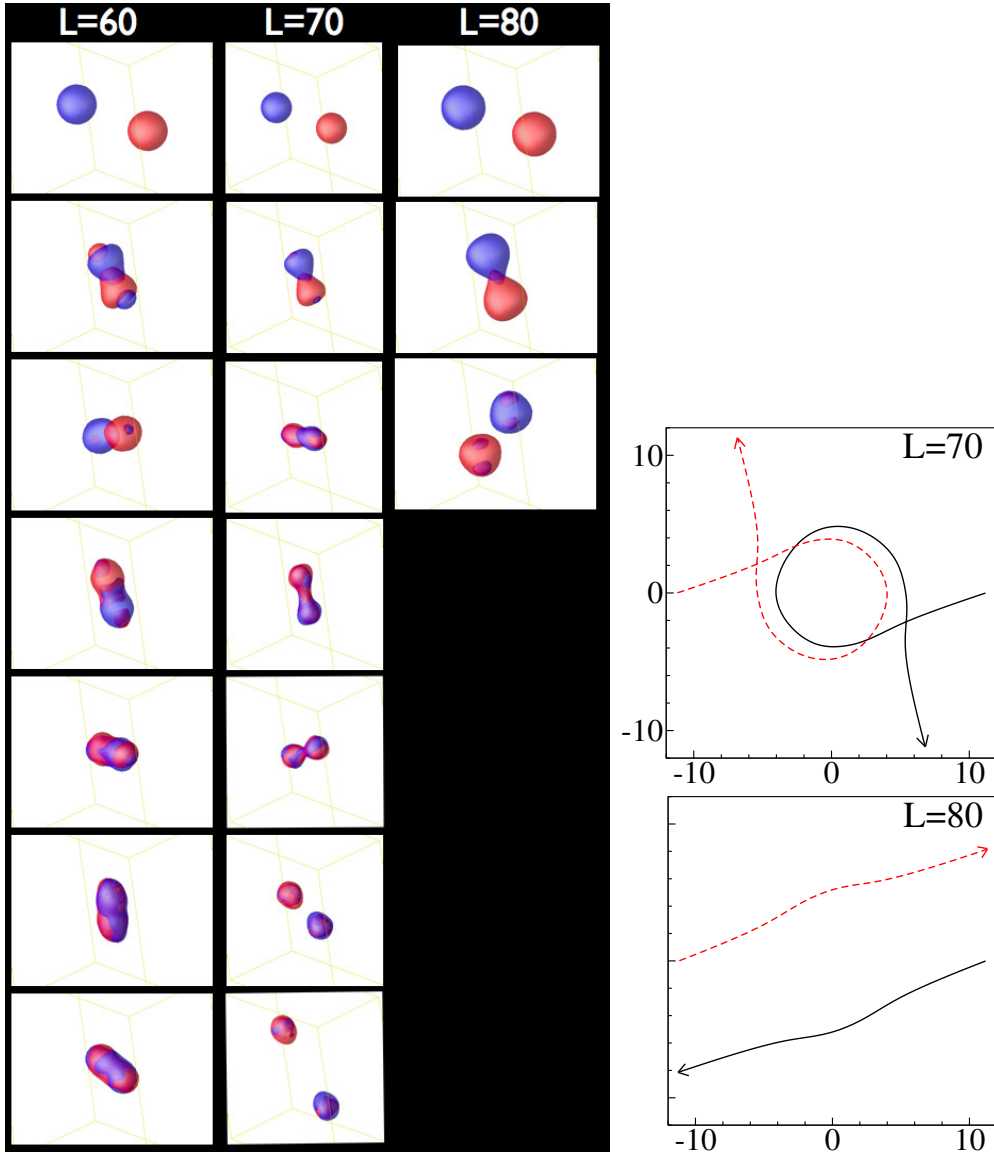


Figure 3.16: (left) Density evolution computed with the TDHF3D code for  $^{40}\text{Ca}+^{40}\text{Ca}$  collisions at  $E_{c.m.} = 128$  MeV. (right) Trajectories of the centers of mass of the fragments.

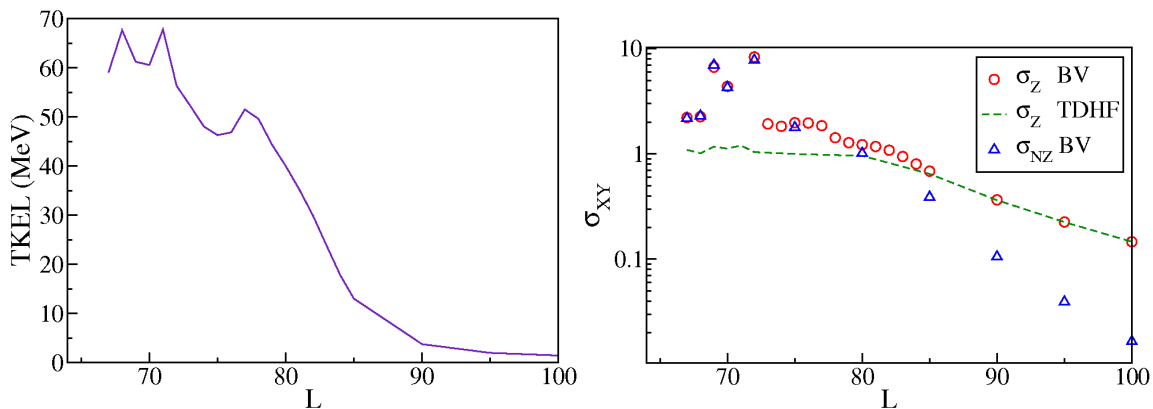


Figure 3.17: Properties of the exit channel of the  $^{40}\text{Ca}+^{40}\text{Ca}$  collisions at  $E_{c.m.} = 128$  MeV as a function of the initial angular momentum  $L$ . (left) Total kinetic energy loss from TDHF. (right) TDHF (dashed line) and BV (circles) fluctuations of  $Z$ , and BV correlations between  $N$  and  $Z$  (triangles) of the outgoing fragments.

with angular momenta  $L=60, 70$  and  $80$  (in units of  $\hbar$ ). Three reaction mechanisms are observed: capture (at  $L = 60$ ), DIC (at  $L = 70$ ), and a partially damped collision (at  $L = 80$ ). In particular, the  $L = 70$  case leads to an orbiting trajectory (see right panels of Fig. 3.16) which is characteristic of a DIC. This trajectory also corresponds to a strongly damped collision, as can be seen from the left panel of Fig. 3.17 where the total kinetic energy loss (TKEL) is plotted as a function of the initial angular momentum. Indeed, around  $L \simeq 70$ , the TKEL is  $\sim 60 - 70$  MeV. These values are slightly below the Viola systematics [VKW85] which predicts  $TKEL_{Viola} \simeq 76$  MeV, indicating that these collisions are almost fully damped.

The right panel of Fig. 3.17 shows the evolution of the fluctuations  $\sigma_Z$  of the number of protons<sup>16</sup> in the outgoing fragments as a function of  $L$ . As expected<sup>17</sup>, the BV prescription (Eq. 1.39) leads to larger fluctuations than standard TDHF fluctuations obtained from Eq. 1.36. This is particularly true for DIC. However, TDHF and BV prescriptions converge at large  $L$ , e.g., for  $L > 90$  where the TKEL is less than 5 MeV, indicating a dominance of quasi-elastic scattering. We conclude that TDHF fluctuations are reasonable for such non-violent collisions. In particular,

---

<sup>15</sup> $\frac{d\sigma}{d\theta_{c.m.}} = 2\pi \sin \theta_{c.m.} \frac{d\sigma}{d\Omega}$  is constant. Then,  $\frac{d\sigma}{d\Omega} \propto \frac{1}{\sin \theta_{c.m.}}$ .

<sup>15</sup>Marston and Koonin claimed that their calculations are in good agreement with experimental data. However, they only computed the fluctuations of  $A = N + Z$  and compared with measured fluctuations of  $Z$ . In addition, their calculations were performed at angular momenta leading to fusion when spin-orbit terms are included (see discussion in Ref. [Bro09]).

<sup>16</sup>Neutron fluctuations are very close to the proton one. This is due to the fact that the collision partners are  $N = Z$  nuclei.

<sup>17</sup>See early applications of the BV prescription for fluctuations where greater fluctuations than their TDHF counterparts were obtained [MK85, BF85, Bro09].

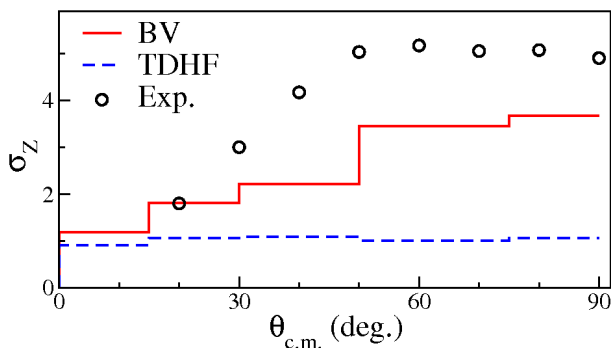


Figure 3.18: Comparison between BV (solid line) and TDHF (dashed line) predictions of  $\sigma_{ZZ}$  for damped events (see text) as a function of  $\theta_{c.m.}$  with data (circles) from [RDF<sup>+</sup>77].

this justifies the calculation of transfer probabilities for sub-barrier collisions with TDHF, as we did in Sec. 3.3.

Fig. 3.17 also shows an application of the BV prescription for the correlations between  $N$  and  $Z$  distributions. These correlations are determined from Eq. 1.37. We observe increasing correlations with decreasing  $L$ . In particular, in DIC, the BV prescription predicts<sup>18</sup>  $\sigma_N \simeq \sigma_Z \simeq \sigma_{NZ}$ , while, for quasi-elastic scattering, correlations are negligible.

Let us recall the signification of such correlations. Uncorrelated distributions means that the probability to transfer  $z$  protons is independent from the probability to transfer  $n$  neutrons, i.e.,  $P(z, n) \equiv P(z)P(n)$ . On the other side, strongly correlated distributions mean that if we measure  $n$  (resp.  $z$ ), then we know what is  $z$  ( $n$ ). This is the case, for instance, if all fragments have  $N = Z$ . In this case, we would have  $P(z, n) \equiv P(z)\delta_{n,z} \equiv P(n)\delta_{n,z}$ . The reality is usually in between and, assuming Gaussian distributions, we have

$$P(n, z) = \left(2\pi\sigma_N\sigma_Z\sqrt{1-\rho^2}\right)^{-1} \exp\left[-\frac{1}{1-\rho^2}\left(\frac{n^2}{\sigma_N^2} + \frac{z^2}{\sigma_Z^2} - \frac{2\rho n z}{\sigma_N\sigma_Z}\right)\right], \quad (3.3)$$

where  $\rho = \frac{\sigma_{NZ}^2}{\sigma_N\sigma_Z}$ . The case  $\rho = 0$  means no correlations between  $N$  and  $Z$  distributions, while the limit  $\rho \rightarrow 1$  corresponds maximum correlations.

In the calculations of  $^{40}\text{Ca}+^{40}\text{Ca}$  at  $E_{c.m.} = 128$  MeV shown in Fig. 3.17, we have  $\sigma_{NZ} \simeq \sigma_N \simeq \sigma_Z$  for DIC ( $L < 80$ ). This means that  $N$  and  $Z$  distributions of the fragments are strongly correlated in DIC. However, quasi-elastic reactions ( $L > 90$  here) have  $\sigma_N \simeq \sigma_Z \gg \sigma_{NZ}$ , meaning almost independent  $N$  and  $Z$  distributions in this case.

We now compare these results with the experimental data of Roynette *et al.* [RDF<sup>+</sup>77]. The angle  $\theta_{c.m.}$  between the fragments in the outgoing channel and the collision axis

<sup>18</sup> $\sigma_N$  is not shown in Fig. 3.17(right) for clarity.

have been determined for each  $L$ . Fig. 3.18 shows theoretical and experimental evolution of the charge fluctuations for damped events (defined, as in Ref. [RDF<sup>+</sup>77], by a  $TKEL > 30$  MeV) as a function of  $\theta_{c.m.}$ . Due to the orbiting, only DIC are expected to emit fragments at large angles, and the experimental plateau at  $\theta_{c.m.} \geq 50$  deg is then attributed to DIC. We see that TDHF fluctuations underestimate experimental results at all angles, except at very forward angles where quasi-elastic reactions dominate. The results of the BV prescription are in better agreement, although they still underestimate data. This is probably due to fusion-fission events (not included in the calculations) leading to large fluctuations and, to a less extent, to the cooling down of the fragments by nucleon emission (see Ref. [27] for more details).

In addition, calculations with exotic nuclei have been performed to study the role of isospin asymmetry in the entrance channel [27]. The  $^{80,92}\text{Kr}+^{90}\text{Zr}$  systems have been investigated at beam energy  $E/A = 8.5$  MeV. Charge equilibration is observed in the  $^{92}\text{Kr}+^{90}\text{Zr}$  due to an initial  $N/Z$  asymmetry, inducing larger correlations between  $N$  and  $Z$  distributions, while fluctuations are only slightly affected. These calculations serve as a theoretical support for the letter of intent "Transport Properties of Isospin Asymmetric Nuclear Matter" to be studied with DIC at SPIRAL2 (R. Lemmon, A. Chbihi, *et al.*).

Finally, other fluctuations should also be computed with the BV approach, such as the width of TKE distributions of the fragments.

### 3.5 Fusion and quasi-fission in heavy systems

In section 3.2, we restricted the study to  $Z_1 Z_2 < 1600$  systems for which no fusion hindrance is usually observed<sup>19</sup>. We now investigate the reaction mechanism in heavy systems with possible fusion hindrance.

We first illustrate the fusion hindrance with TDHF calculations of fusion thresholds<sup>20</sup> [Ave09, 29]. Then, we discuss an experimental search<sup>21</sup> for fusion-evaporation events in the  $^{124}\text{Sn}+^{136}\text{Xe}$  reaction [2]. Then we present an experimental study of the quasi-fission mechanism [39]. Finally, we discuss results of a recent study of

---

<sup>19</sup>This threshold is empirical. Based on his extra-push model, Swiatecki proposed an effective fissility, depending on both charges and masses of the nuclei, above which extra-push energy is needed to fuse [Swi82]. Note that this should not be confounded with a threshold for quasi-fission which, in fact, may occur in lighter systems. Indeed, quasi-fission has been observed in, e.g.,  $^{16}\text{O}, ^{32}\text{S}+^{238}\text{U}$  [HDL<sup>+</sup>96, Itk11, NMU<sup>+</sup>07], and even in lighter systems such as  $^{32}\text{S}+^{208}\text{Pb}$  [NMU<sup>+</sup>07] and  $^{24}\text{Mg}+^{186}\text{W}$ .

<sup>20</sup>This study was partly performed by B. Avez during his PhD.

<sup>21</sup>This experiment was part of B. Avez's PhD work. We participated to the preparation and data acquisition. With A. Drouart, we also were in charge of the data analysis.

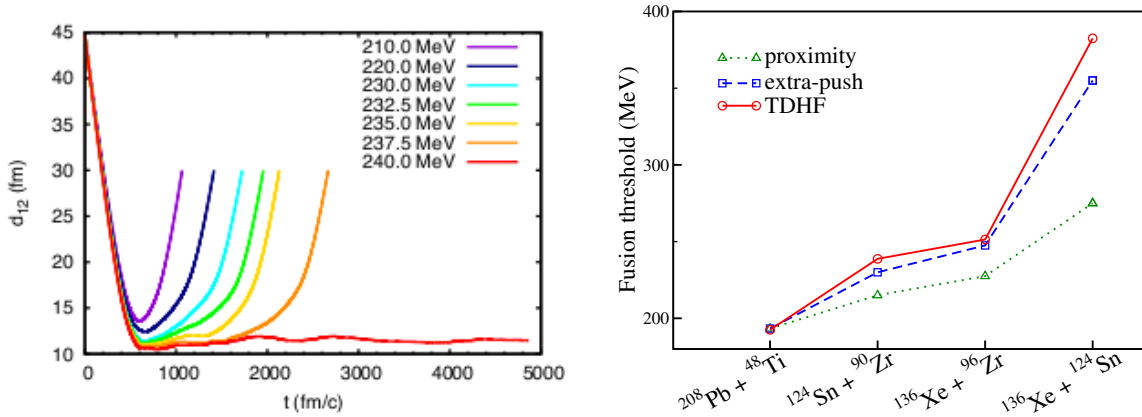


Figure 3.19: (left) Relative distance between fragments as a function of time for head-on  $^{90}\text{Zr}+^{124}\text{Sn}$  collisions computed with the TDHF3D code. (right) TDHF fusion thresholds for several heavy systems are compared with the proximity barrier [BRST77] and with results from the extra-push model [Swi82].

quasi-fission with TDHF calculations<sup>22</sup> [41].

### 3.5.1 TDHF calculations of fusion hindrance

The left panel of Fig. 3.19 shows the evolution of the relative distance between fragments as a function of time for  $^{90}\text{Zr}+^{124}\text{Sn}$  central collisions at different energies [Ave09]. The long contact time at  $E_{c.m.} = 240$  MeV is interpreted as a capture trajectory leading to fusion.

Similar calculations have been performed for other systems with  $Z_1 Z_2 > 1600$  [29]. The TDHF fusion thresholds are shown in the right panel of Fig. 3.19. A comparison with the interaction barriers predicted by the proximity model<sup>23</sup> [BRST77] shows that dynamical effects included in TDHF induce a strong increase of the fusion threshold, in particular for the more heavy and symmetric systems. The order of magnitude of the additional energy needed to fuse is similar to that of the extra-push phenomenological model [Swi82].

These results motivate a deeper study of fusion hindrance. In particular, the quasi-fission mechanism which is mostly responsible of this hindrance is studied in subsection 3.5.4 with the TDHF approach.

<sup>22</sup>These calculations are performed by A. Wakhle in the framework of his PhD at the Australian National University.

<sup>23</sup>A comparison with barriers obtained from the FROZEN code is planned, however the latter are time consuming. Indeed, the translation of the wave-functions using a Lagrange mesh technique is computationally heavy.

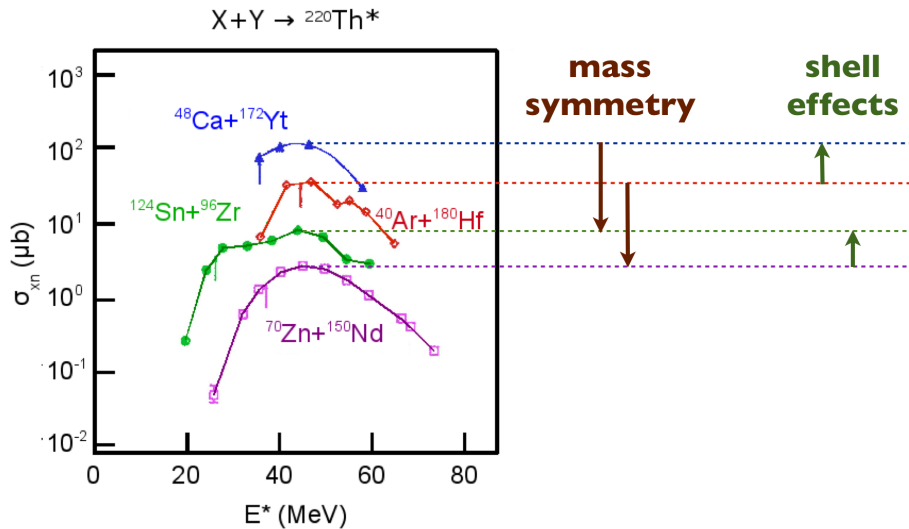


Figure 3.20: Experimental fusion-evaporation cross-sections in reactions forming  $^{220}\text{Th}^*$ . Adapted from [Sto98].

### 3.5.2 Search for fusion-evaporation events in the $^{124}\text{Sn}+^{136}\text{Xe}$ reaction

Fusion reactions forming very heavy nuclei may show a strong dependence of the entrance channel [HM00]. This is illustrated in Fig. 3.20 for reactions forming  $^{220}\text{Th}^*$  [Sto98]. We can see that fusion-evaporation cross-sections decrease when the mass asymmetry increases. On the contrary, these cross-sections increase when shell effects are present in the entrance channel<sup>24</sup>. Spherical shells may indeed result in so-called “cold valleys” in the potential energy surface, which lead to the compact CN configuration [SGSG76, FGM<sup>+</sup>05, Ari06]. Fusion through these valleys may also be favoured because energy dissipation should be weaker, allowing greater interpenetration before the initial kinetic energy is dissipated [HD05, Arm00]. These effects may be vital in the recent successful synthesis of SHE [HM00, Mor07, Oga06].

In Ref. [2], we present the results of an experiment where we searched for the fusion-evaporation residues in the  $^{124}\text{Sn}+^{136}\text{Xe}$  system at  $E^* \simeq 20$  MeV. Although this system is quasi-symmetric, it contains two magic numbers ( $^{124}\text{Sn}$  with  $Z = 50$  and  $^{136}\text{Xe}$  with  $N = 82$ ). In addition, fusion-evaporation cross sections should be maximum for relatively small excitation energies (between 15 and 30 MeV). The choice of this system was also motivated by the possibility to use high intensity exotic xenon beams ( $\sim 10^{10}$  pps for ) with the upcoming SPIRAL2 facility. Such beams could be used for the synthesis of more neutron-rich SHE (see discussion in section 3.1.2).

<sup>24</sup> $^{248}\text{Ca}$  is doubly magic and  $^{124}\text{Sn}$  has a magic proton number.

Table 3.1: Smallest upper limit of the cross-sections in pb, with a confidence level of 68.2%.

residue	$^{257}\text{Rf}$	$^{258}\text{Rf}$	$^{259}\text{Rf}$
cross-section (upper limit) in pb	172.4	80.8	235.1

The experiment was performed at GANIL with the FULIS setup for the detection of SHE. The residues were separated from the beam with a Wien filter and implanted in a double-sided silicon-stripped detector (DSSD) (see Ref. [2] for more details). The rejection of the beam<sup>25</sup> ( $5 \times 10^8$ ) was not sufficient for a clear identification of the residues. The residues were then identified in the off-line analysis from their  $\alpha$ -decay and spontaneous fission using the genetic-correlation method.

The result of this analysis showed that no fusion-evaporation residues could be unambiguously identified. A detailed statistical analysis was performed to estimate upper limits of the cross-sections of the  $1n$ ,  $2n$ , and  $3n$  evaporation channels [2]. The resulting cross-sections are given in table 3.1. Comparing these upper limits with the maximum cross-sections for the  $^{50}\text{Ti}+^{208}\text{Pb}$  reaction which are of the order of 10 nb for the  $1n$  and  $2n$  channels [Heß97], we see that the mass symmetry of the entrance channel induces a strong fusion hindrance. This conclusion is in agreement with other measurements in similar symmetric systems [Oga09].

To conclude, if there is no drastical (and surprising) increase of the fusion cross-section with the number of neutrons in the projectile, fusion with neutron-rich radioactive beams will not be sufficient to form neutron-rich SHE with the present detection setup<sup>26</sup>. The quasi-fission reaction mechanism which is responsible for the observed fusion hindrance in heavy quasi-symmetric system needs also a detailed investigation in order to increase the predictive power of the fusion-evaporation theoretical models.

### 3.5.3 Quasi-fission: interplay between shells and isospin

A series of experiments to investigate the quasi-fission process have been performed recently at the Australian National University in Canberra [14, dRHD<sup>+</sup>11, LdRH<sup>+</sup>12, 15, 39].

In Ref. [15], the role of the shell structure of the outgoing fragments has been

<sup>25</sup>The rejection coefficient is smaller than in asymmetric reactions in normal kinematics due to a smaller difference between the beam and residue velocities.

<sup>26</sup>Another possibility, using multi-nucleon transfer in actinide collisions, will be discussed in section 3.6.

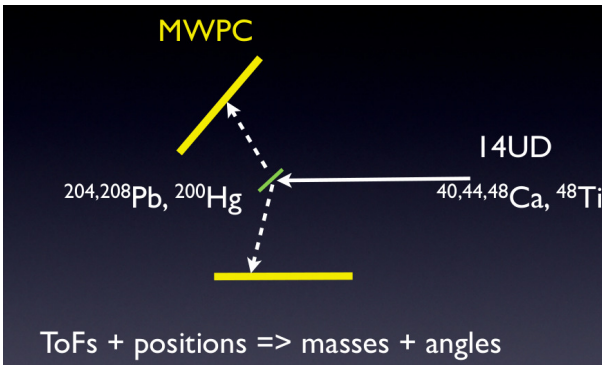


Figure 3.21: Experimental setup for the measurement of MAD.

studied in a series of measurements with  $^{48}\text{Ti}$  beams on target nuclei from  $^{144}\text{Sm}$  to  $^{208}\text{Pb}$  at sub-barrier energies. The main result is that quasi-fission mass distributions show extra yields for asymmetric exit channels similar to those observed in low energy fission. This systematic study confirmed the important role of shell effects in quasi-fission observed with other systems [Chi03].

In Ref. [39], we showed that shell effects in the entrance channel may also affect the quasi-fission process. This was done by measuring mass-angle distributions (MAD) of the fragments in several reactions at sub-barrier energies <sup>27</sup>. The experimental setup is shown in Fig. 3.21. The beams were produced by the 14UD electrostatic accelerator. Two Multi-Wire Proportional Chambers (MWPC) were used to measure time and positions of both fission fragments in coincidence (see Ref. [39] for more details on the geometry of the setup). Time of flight (ToF) and positions were converted into fragment masses and angles using two-body kinematics.

Fig. 3.22 shows the resulting MAD (up) and the projections on the mass-ratio axis (bottom). The mass ratio is defined as  $M_R = m_2/(m_1 + m_2)$  where  $m_2$  (resp.  $m_1$ ) is the mass of the fragment in the back (front) detector. Fission and quasi-fission fragments are located between the bands at extreme  $M_R$  corresponding to (quasi)-elastic and deep-inelastic events. Fig. 3.23 sketches the "trajectory" of the fragments in the MAD. In particular, short scission times induce correlations, i.e. the distribution forms a finite angle with the  $M_R = 0.5$  axis.

Correlations between mass and angle of the fission fragments can be seen on some spectra of Fig. 3.22 (see, e.g., the case of  $^{44}\text{Ca}+^{208}\text{Pb}$  which has the highest statistics). Such correlations increase the width of the mass ratio distribution (lower panels). We then use the width of the fission fragment mass distribution to quantify the amount of "fast re-separation" which could be associated to quasi-fission events. In particular, the  $^{16}\text{O}+^{238}\text{U}$  reaction, which is known to exhibit only a small amount of quasi-fission [HDL<sup>+</sup>96], gives a width which can be considered as an upper limit

<sup>27</sup>The off-line analysis of these reactions was performed by David Hinde and myself.

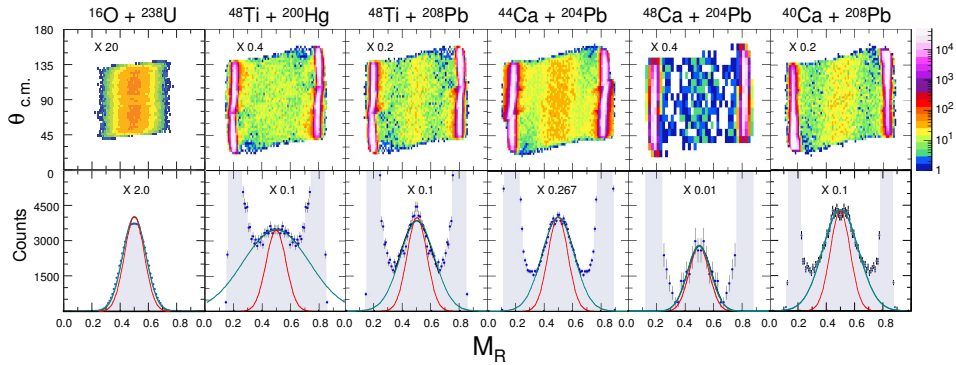


Figure 3.22: (upper panels) Measured MAD. (lower panels) Projected mass ratio spectra. Gaussian fits to the region around  $M_R=0.5$  are shown (turquoise lines). Gaussian functions with  $\sigma_{M_R} = 0.07$  (thin red lines) are shown for reference.

for pure fusion-fission events.

The left panel of Fig. 3.24 shows the width of the fission-like fragment mass distributions as a function of the number of magic numbers in the entrance channel. We see that, apart for the  $^{40}\text{Ca}+^{208}\text{Pb}$  case which is discussed below, there is a clear link between the two quantities, i.e., the more the magicity, the smaller the width. This is interpreted as a hindrance of the quasi-fission process due to shell-effects in the entrance channel. This is consistent with what is observed in Fig. 3.20, i.e., an increase of fusion due to shell effects.

We see in Fig. 3.24(left) that the  $^{40}\text{Ca}+^{208}\text{Pb}$  does not lie on the global trend. In Ref. [39], we interpreted this apparent discrepancy as an effect of charge equilibration occurring in the early stage of the collision. This equilibration process is indeed very rapid as shown by the TDHF calculations reported in the right panel of Fig. 3.24. The latter are performed at the experimental energy  $E_{c.m.} = 179.1$  MeV, and varying  $L$  to obtain different collision times.  $\Delta(N/Z)_f$  is the difference between the  $N/Z$

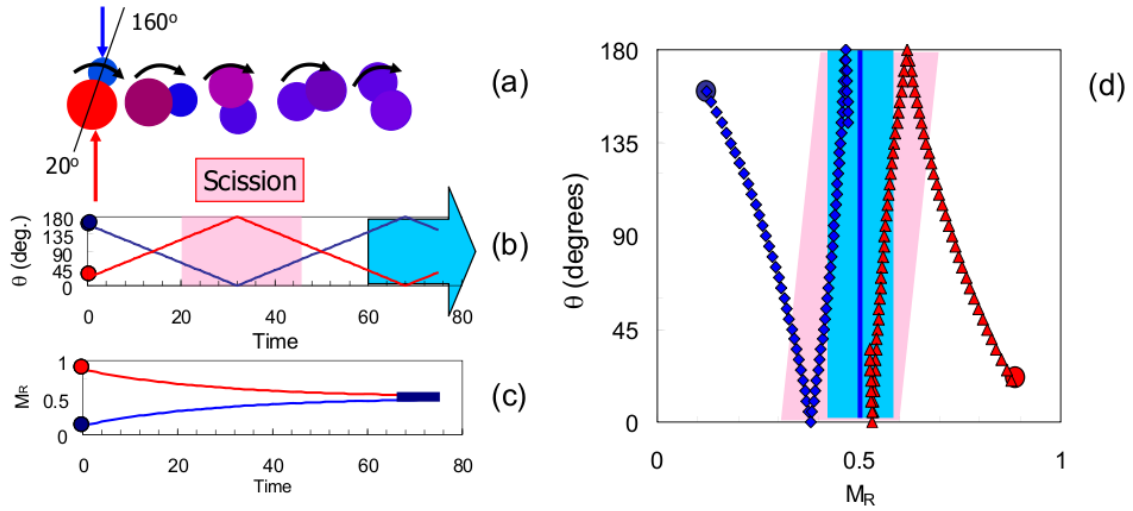


Figure 3.23: Qualitative illustration of the distribution of quasi-fission fragments in the MAD. (a) Non-central collisions induce a rotation of the di-nuclear system. During the rotation, nucleon transfer occurs toward symmetry. (b) Evolution of the angle as a function of time. The two colored area corresponds to two different scission times. (c) Time evolution of the fragment masses toward symmetry. (d) "trajectory" of the fragments in the MAD. Short scission times (pink area) lead to an angle in the MAD, whereas for longer times (blue area) such correlations disappear. Courtesy of D. Hinde [14].

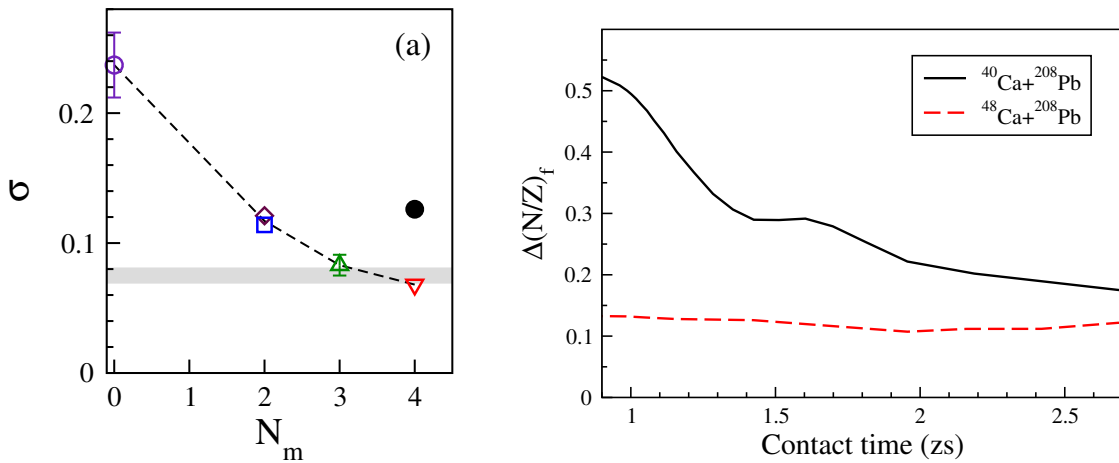


Figure 3.24: (left) Widths of the mass distributions of the fission-like events as a function of the magicity (quantified by the number of magic numbers  $N_m$ ) in the entrance channel. (right) TDHF calculations of charge equilibration: the difference between final and initial  $N/Z$  of the fragments is shown as a function of the contact time. Adapted from [39].

ratio of the fragments after the collision. We observe a (partial) equilibration<sup>28</sup> (i.e., a reduction of  $\Delta(N/Z)_f$ ) within  $\sim 2$  zs. This time is short as compared to the quasi-fission time which, according to simple simulations based on the model of Ref. [dRHD<sup>+</sup>11], is longer than 10 zs. This means that the collision partners change their  $N$  and  $Z$  at contact and, as far as quasi-fission is concerned, behave like a non-magical system. This effect is not present in  $^{48}\text{Ca}+^{208}\text{Pb}$  which is less  $N/Z$  asymmetric and does not encounter a charge equilibration (see dashed line in the right panel of Fig. 3.24). Fusion is then more probable in this reaction which preserves its magic nature in the di-nuclear system.

We conclude that shell effects in the entrance channel hinder quasi-fission (and then, favour fusion) only for systems with small  $N/Z$  asymmetry.

### 3.5.4 TDHF calculations of the $^{40}\text{Ca}+^{238}\text{U}$ reaction

The previous studies showed the importance of the quasi-fission process as a mechanism in competition with fusion, hindering the formation of heavy systems. A quantum and microscopic theoretical framework able to describe properly the quasi-fission properties would be of great importance to get a deep insight into the interplay between structure properties and this mechanism.

Here, our goals are to show that quasi-fission may appear in the outgoing channel within the TDHF approximation, and that TDHF calculations can then be used to predict quasi-fission properties. As a mean-field approach, however, the TDHF theory may be used to study a reaction mechanism only if the latter is close to the mean-field trajectory. In fact, the previous TDHF calculations of the  $^{40,48}\text{Ca}+^{208}\text{Pb}$  systems at sub-barrier energies did not show any quasi-fission. In these cases, the mean-field trajectories were dominated either by quasi-elastic scattering or by fusion.

However, recent TDHF calculations performed by Aditya Wakhle<sup>29</sup>, show that heavier systems such as  $^{40}\text{Ca}+^{238}\text{U}$  around the barrier could lead to quasi-fission at the mean-field level. Examples of density evolutions obtained with the TDHF3D code are shown in Fig. 3.25. All these configurations lead to quasi-fission, i.e., a important multi-nucleon transfer from the heavy fragment toward the light one. We also see that the mass equilibration (i.e., the formation of two fragments with symmetric masses) is not complete and may depend on the initial conditions.

Fig. 3.26 presents a summary of our preliminary results for central collisions. We see that all the calculations with the  $^{238}\text{U}$  deformation axis aligned with the

---

<sup>28</sup>The equilibration is expected to be complete, i.e., with  $\Delta(N/Z)_f \simeq 0$ , only in mass symmetric reactions.

<sup>29</sup>A. Wakhle is doing an PhD at Canberra on experimental studies of quasi-fission under the supervision of D. Hinde.

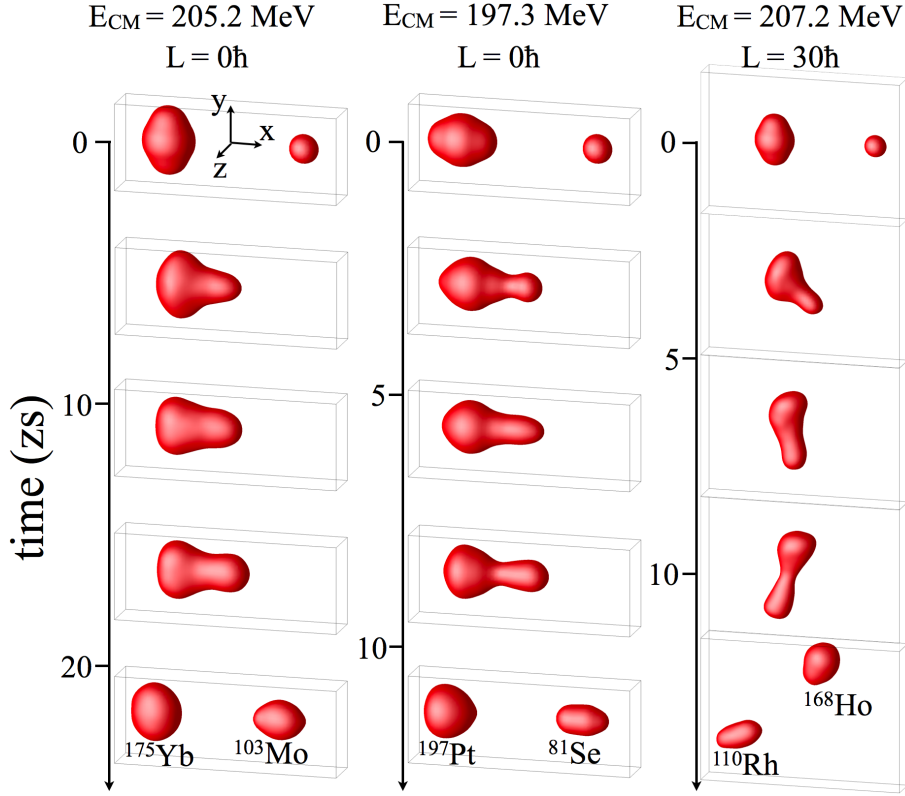


Figure 3.25: Snapshots of the TDHF isodensity at half the saturation density in the  $^{40}\text{Ca}+^{238}\text{U}$  system for different initial orientations,  $L$  and  $E_{c.m.}$ .

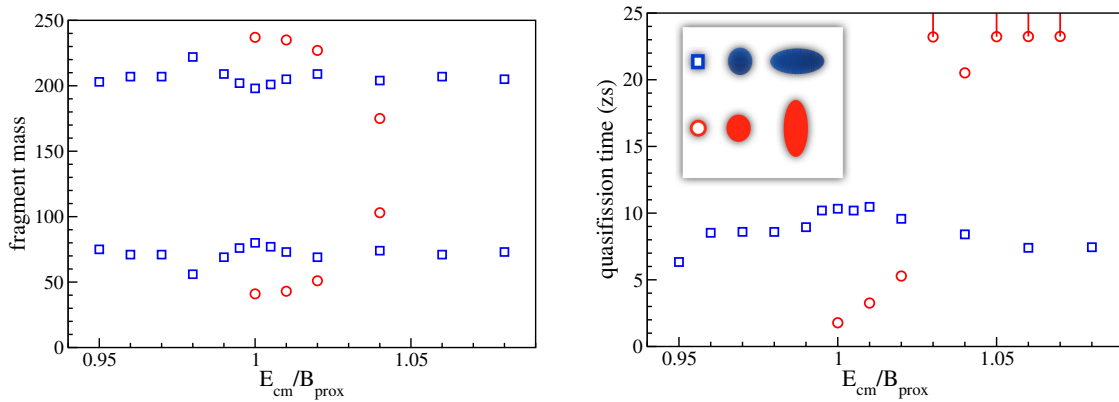


Figure 3.26: TDHF calculations of the mass of the fragments (left) and of the quasi-fission time (right) in  $^{40}\text{Ca}+^{238}\text{U}$  central collisions as a function of the center of mass energy (divided by the proximity barrier [BRST77]). For quasi-fission times larger than 23 zs, only a lower limit is given. Two different orientations of the  $^{238}\text{U}$  are considered (see inset).

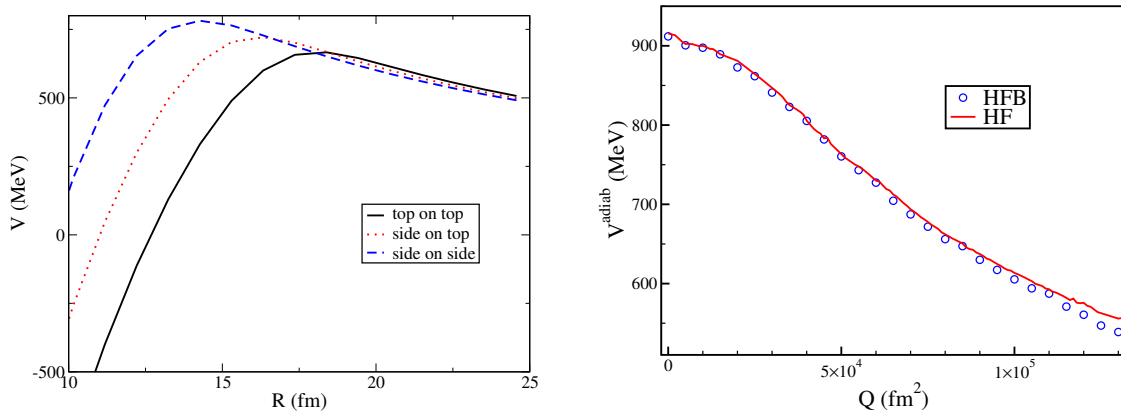


Figure 3.27: (left) Nucleus-nucleus potentials of the  $^{238}\text{U}+^{238}\text{U}$  system obtained with the FROZEN code for different orientations of the actinides as a function of their distance. (right) The adiabatic potential is computed with the EV8 code as a function of the total quadrupole moment. Calculations are performed with (HFB) and without (HF) pairing.

collision axis lead to a quasi-fission with partial mass equilibration and quasi-fission times smaller than 10 zs. In particular, this orientation never leads to fusion, while the other orientation produces long contact time above the barrier which may be associated to fusion. We also see that longer quasi-fission times lead to larger mass equilibration. Calculations of non-central  $^{48}\text{Ca}+^{238}\text{U}$  collisions are ongoing in order to compare with experimental data of [Tök85] and to relate the angle of the outgoing fragments with quasi-fission times.

### 3.6 Actinide collisions

The collision of actinides form, during few zs, the heaviest nuclear systems available on Earth. In one hand, such systems are interesting to study the stability of the QED vacuum under strong electric fields [RMG81, AH08, 13]. In the other hand, they might be used to form neutron-rich heavy and super-heavy elements via multi-nucleon transfer reactions, as discussed in section 3.1.2.

As we saw in section 3.5, there is a clear link between the collision time and the amount of transferred nucleons. It is then important to optimize collision times in order to favour the formation of heavy systems. It was initially believed that the potential between two actinides have a barrier (and then a pocket) [SGP85], leading to possible long contact times at energies close to the barrier. Such barriers are predicted by frozen models (see the left panel of Fig. 3.27 where the potentials have been computed with the FROZEN code). However, Berger and collaborators showed with constrained HFB calculations of the composite system that there was, in fact,

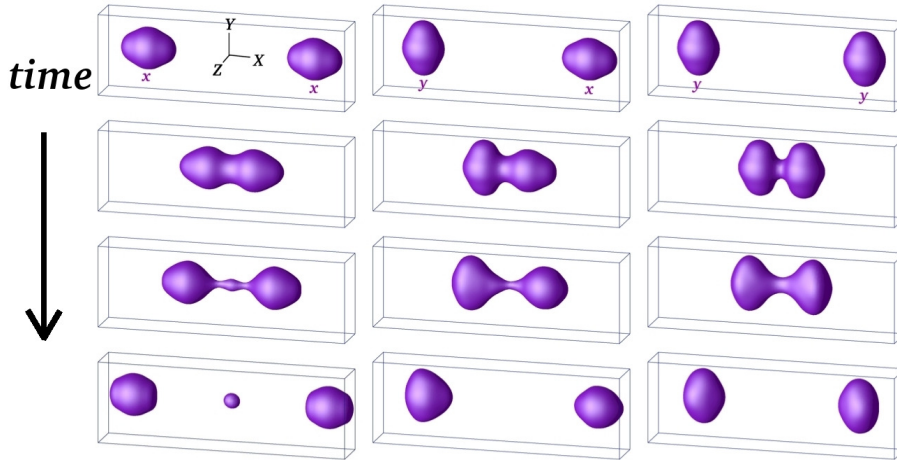


Figure 3.28: Snapshots of the isodensity at half the saturation density in  $^{238}\text{U}+^{238}\text{U}$  central collisions at  $E_{c.m.} = 900$  MeV from TDHF calculations. Snapshots are given at times  $t = 0, 1.5, 2.7,$  and  $4.2$  zs from top to bottom. From Ref. [13].

no barrier in the (adiabatic) potential [BABW90]. We confirmed this result with the EV8 code, as shown in the right panel of Fig. 3.27 [29].

The use of microscopic approaches is then improving the description of the reaction mechanisms in actinide collisions. We studied such collisions<sup>30</sup> with the TDHF3D code in Refs. [13, 29, 18, 38]. Fig. 3.28 shows zeptosecond snapshots of the density in  $^{238}\text{U}+^{238}\text{U}$  central collisions at  $E_{c.m.} = 900$  MeV. We see that the initial orientation of the nuclei plays a crucial role on the reaction mechanism [13]. For instance, we observe the formation of a third fragment in the left column. A net transfer is also observed in the middle column. Indeed, integration of proton and neutron densities in each reactant indicates an average transfer of  $\sim 6$  protons and  $\sim 11$  neutrons from the right to the left nucleus. In this case, transfer occurs from the tip of the aligned nucleus to the side of the other. This configuration is then expected to favor the formation of nuclei heavier than  $^{238}\text{U}$ .

We pursued this idea in Ref. [18] and identified a new "inverse quasi-fission" mechanism. The inverse process of quasi-fission corresponds to a transfer of nucleons from the light collision partner to the heavy one. Such a mechanism may occur in actinide collisions due to shell effects in the  $^{208}\text{Pb}$  region [Vol78, ZOIG06]. The mechanism we propose in Ref. [18] is different (but may be complementary). It occurs for specific orientations of the actinides, where the tip of the lighter one is in contact with the side of the heavier one.

An example of inverse quasi-fission reaction is shown in the left panel of Fig. 3.29,

<sup>30</sup>The study of the  $^{238}\text{U}+^{238}\text{U}$  reaction was part of the experimental PhD of Cédric Golabek [13, Gol09]. David Kedziora studied the  $^{232}\text{Th}+^{250}\text{Cf}$  system during a summer training session at Canberra at the end of his 3rd year (BSc).

where a  $^{232}\text{Th}+^{250}\text{Cf}$  collision produces a  $^{265}\text{Lr}$  fragment at the end of the calculation<sup>31</sup>. The  $^{265}\text{Lr}$  heavy fragment indicates the average  $N$  and  $Z$  of a distribution. The fluctuations and correlations of these distributions have been computed with the BV prescriptions (Eqs. 1.39 and 1.37) in Ref. [38]. Fig. 3.29(left) shows the resulting probabilities assuming Gaussian distributions of the form given in Eq. 3.3.

We see that many  $\beta$ -stable and neutron-rich transfermium *primary* fragments could be produced thanks to this inverse quasi-fission mechanism. In particular, these nuclei are more neutron-rich than those formed in fusion-evaporation reactions.

This inverse quasi-fission process needs further studies to determine the role of the shape, orientation, shell closures, mass and charge asymmetries, beam energy, and angular momentum on the transfermium production yields. Associated cross-sections need to be determined to estimate the experimental possibility of neutron-rich transfermium and SHE productions.

Only few early experimental data exist on heavy element production in actinide collisions, with chemical identification techniques leading to limited sensitivity in terms of cross-section measurements. For example, the smallest cross-sections obtained for the production of transfermiums (in this case, mendeleevium isotopes with  $Z = 101$ ) were of the order of  $\sim 20$  nb in the  $^{238}\text{U}+^{248}\text{Cm}$  reaction [Sch82], while modern fusion experiments using spectrometers for the fragment separation have reached 30 fb [Mor07], i.e.  $\sim 6$  orders of magnitude smaller. The use of modern experimental techniques and equipments, such as the dedicated Inelastic Reaction Isotope Separator (IRiS) [DBD<sup>+</sup>11] for multi-nucleon transfer products which will be installed at GSI, with actinide collisions is then expected to be very fruitful in terms of transfermium identification.

A non exhaustive list of relevant heavy nuclei to be searched for is given below:

- SHE in the island of stability (e.g.,  $^{298}114$ ).
- $^{261-263}\text{Fm}$  which have a predicted  $\beta$ -decay. If observed, they would be the heaviest nuclei with this decay mode.
- $^{264}\text{Fm}$  could undergo symmetric spontaneous fission to form two doubly magic  $^{132}\text{Sn}$ .
- From  $^{271}\text{Rf}_{104}$  to  $^{284}\text{Mt}_{109}$ ,  $\beta$ -stable nuclei and their neighbors are predicted to decay by spontaneous fission. Verifying this prediction would constrain the models predicting a spontaneous decay region in the decay path of r-process

---

<sup>31</sup>This fragment is not exactly a primary fragment as at the final time of the calculation, about 3 neutrons have been emitted in the entire system (see Fig. 4 of [18]). However, it is still excited (its excitation energy may be estimated from the TKE) and may cool down by the emission of 1-2 additional neutrons or, of course, by fission.

progenitors with mass  $\sim 300$  [LMPPT11]. The existence of the latter is crucial to determine if long-lived SHE can be produced in the r-process.

- $^{264}\text{No}_{102}$  has 162 neutrons which corresponds to a deformed shell gap in the  $Z = 108$  region. The question of the robustness of the  $N=162$  shell gap away from  $Z=108$  could be answered by measuring the mass and life-time of  $^{264}\text{No}_{102}$  and its neighbors.
- $^{266}\text{Rf}_{104}$  and its neighbors should be studied to "fill in" the blank spot between cold and hot fusion decay chains.
- $^{290}\text{114}$ ,  $^{287}\text{113}$ ,  $^{286}\text{112}$  should be produced to confirm the increase of life time with neutron number attributed to the closeness of the island of stability<sup>32</sup>.
- Elements  $Z = 109 - 111$  still need chemical characterization [Gäg11]. Present chemical techniques tag the isotope thanks to their  $\alpha$ -decay and  $T_{1/2} > 0.5$  s is required.  $^{278}\text{Mt}_{109}$  and  $^{282}\text{Rg}_{111}$  are good candidates. Ds ( $Z = 110$ ) element is more problematic as no isotope decaying by  $\alpha$ -emission with  $T_{1/2} > 0.5$  s is known. Decay modes of  $^{280}\text{Ds}_{110}$  should then be measured. If the latter does not match experimental requirements for chemistry studies, isotopes on the other side of the spontaneous fission region (see Ref. [LMPPT11]), i.e.  $^{287}\text{Ds}$  and its neighbors, might be considered as they are expected to decay by  $\alpha$  or  $\beta^-$  emission.
- $^{290}\text{115}$ , which has  $T_{1/2} = 0.7$  s is the next milestone in chemical studies of SHE.

### 3.7 Conclusion and perspectives

This chapter was devoted to the study of heavy-ion reaction mechanisms in order to study quantum dynamical effects in complex systems and to investigate the formation of new nuclei.

The TDHF theory was shown to reproduce energy thresholds for fusion for systems spanning the entire nuclear chart. The effect of deformation and transfer on fusion barriers is well treated. The competition with quasi-fission leading to a fusion hindrance in heavy systems is also included. The possibility to study the quasi-fission mechanism with a fully microscopic quantum approach is promising. It will help us to understand the strong fusion hindrance we observed experimentally in a quasi-symmetric heavy reaction. In another experiment, we observed a hindrance

---

<sup>32</sup> $^{227}\text{112}$  and  $^{285}\text{112}$  have  $T_{1/2} = 0.7$  ms and 34 s measured half-lives, respectively. A gain of 8 neutrons increases the life-time by 5 orders of magnitude!

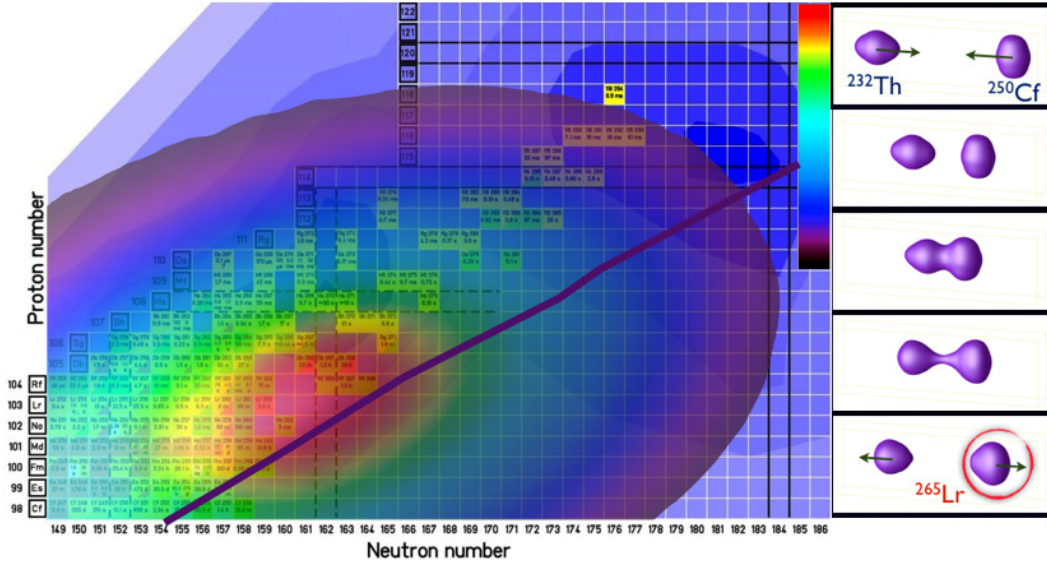


Figure 3.29: (right) Snapshots of the isodensity at half the saturation density in  $^{232}\text{Th}+^{250}\text{Cf}$  central collisions at  $E_{c.m.} = 916$  MeV. (left) Gaussian distributions of  $N$  and  $Z$  with widths and correlations computed with the BV prescription (linear color scale).

of quasi-fission in magic systems. This effect remains to be studied with the TDHF approach.

It was also shown that the charge equilibration process in  $N/Z$  asymmetric collision affects the reaction mechanism: excitation of a preequilibrium GDR in the compound system (which can be used to study the path to fusion), enhancement of proton stripping and neutron pickup, correlations between fragment  $N$  and  $Z$  distributions in DIC (which should be sensitive to the symmetry energy), and the breaking of shell effects in the early stage of the collision. The latter effect was invoked to explain our experimental observation of an increase of quasi-fission in the  $^{40}\text{Ca}+^{208}\text{Pb}$  system as compared to the  $^{48}\text{Ca}+^{208}\text{Pb}$  one.

Actinide collisions have been investigated both within the TDHF approach and with the BV prescription. A new inverse quasi-fission mechanism associated to specific orientations is found in our numerical simulations. This mechanism might produce  $\beta$ -stable and neutron-rich heavy and super-heavy nuclei. A systematic investigation of this effect (cross-sections, angular and energy distributions) is mandatory to help the design of future experimental equipments dedicated to the study of fragments produced in actinide collisions. The importance of isospin asymmetry in the entrance channel should be considered in planning fusion experiments with exotic beams to form and study new heavy nuclei.

Quantum effects at the single-particle level are well treated in the TDHF ap-

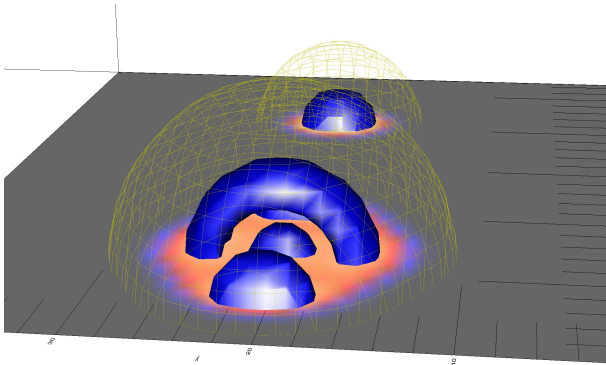


Figure 3.30: Initial condition of a  $^{40}\text{Ca}+^{238}\text{U}$  collision visualised with the SDVision code. Two isodensities are shown (yellow grid and blue area). A projection of the density is also shown on the  $z = 0$  plane.

proach, allowing for realistic predictions of independent particle transfer probabilities using a particle-number projection technique. A comparison with experimental data shows the importance of pairing correlations on transfer. The latter could be studied with 3D TDHFB codes in the future. In particular, one could answer the question on the origin of these pairing correlations: Are they present in the ground-states or are they generated dynamically during the collision?

A strong limitation of the TDHF approach is that it does not allow for quantum tunnelling of the many-body wave function. As a result, sub-barrier fusion cannot be studied. Recently, suppression of tunnelling was observed at deep sub-barrier energies, which could not be reproduced by standard coupled channel calculations [Jia04, DHDT<sup>+</sup>07, EJS10]. This is one of the biggest puzzles in low-energy heavy ion collision physics, attracting the interest of physicists from various fields including astrophysics, where changed quantum tunnelling rates can have drastic effects [GBC<sup>+</sup>07]. In the future, microscopic models should be developed to study such low-energy reactions including the tunnelling of the many-body wave-function. A possible approach is to use an extension of the TDHF theory based on a path integral technique and on the stationary phase approximation [Neg82] (see discussion in section 1.6).

Finally, it is worth mentioning the collaborative work with Daniel Pomarede and Bruno Thooris from CEA/Sedi on the visualisation of TDHF simulations of heavy-ion collisions with their SDVision code initially developed for astrophysical simulations (<http://irfu.cea.fr/Projets/COAST/>). It will allow a better analysis of the interplay between specific structures generated by quantum effects and the reaction mechanisms. An example of initial condition of the  $^{40}\text{Ca}+^{238}\text{U}$  collision is shown in Fig. 3.30 where we can clearly see internal structures in the  $^{238}\text{U}$  nucleus.

# Conclusion

Nuclei are ideal to investigate fundamental aspects of the quantum many-body problem. They exhibit collective motions built from coherent superpositions of the states of their constituents. Examples range from collective vibrations to the formation of a compound system in collisions. These features are common to other composite systems (atomic clusters, molecules, Bose-Einstein condensates...). Their study in nuclear systems is obviously part of a wider physics field.

Different studies of nuclear dynamics, from collective vibrations to heavy-ion collisions have been presented in this report. A particular attention was devoted to the interplay between collective motions and internal degrees of freedom within a unified theoretical description.

We showed that strongly interacting systems such as nuclei could exhibit collective vibrations in the continuum, and that their direct decay could be used to infer their microscopic structure. We also questioned the harmonic nature of these vibrations. In particular, we identified a source of anharmonicity from the coupling between different vibrational modes. Nuclei are known to exhibit superfluidity due to pairing residual interaction and it is natural to wonder if the pairing field could also vibrate. We then extended the theoretical approach to study such pairing vibrations.

Large amplitude collective motions were investigated in the framework of heavy-ion collisions. We described the mechanism of the formation of a compound system. In particular we discussed how fusion is affected by the internal structure of the collision partners. We then investigated the other mechanisms in competition with fusion, and responsible for the formation of fragments which differ from the entrance channel: transfer reactions, deep-inelastic collisions, and quasi-fission. We finally studied actinide collisions forming, during very short times of few zeptoseconds, the heaviest nuclear systems available on Earth. In particular, we identified a new reaction mechanism occurring in these collisions which could be used to study the upper part of the nuclear chart.

We started this report with a desire to investigate fundamental quantum dynamics in complex systems. Let me close the discussion by introducing a key question

in this research area which I plan to address in the future within the framework of heavy-ion collisions, in particular at sub-barrier energies: How does the composite nature of complex systems affect the tunnelling of the many-body wave function?

This question has been investigated within coupled channel approaches for many years, allowing for a good understanding and description of important phenomena, such as sub-barrier fusion enhancement due to the coupling between relative motion and low-lying collective modes.

I believe that microscopic approaches will bring similar major advances in this field. For instance, they would allow for an understanding of the role of dissipation (possibly inducing decoherence) on deep-sub-barrier fusion. In particular, this question is crucial to predict the asymptotic behaviour of fusion probabilities at extremely low (astrophysical) energies.

Future is shining for nuclear dynamics.

# Appendix A

## TDHF approach from the standard variational principle

Consider a state of  $N$  independent particles described by the Slater determinant  $|\phi\rangle$ . The action defined in Eq. 1.2 reads

$$S \equiv S_{t_0, t_1}[\phi] = \int_{t_0}^{t_1} dt \langle \phi(t) | \left( i\hbar \frac{d}{dt} - \hat{H} \right) | \phi(t) \rangle \quad (\text{A.1})$$

where  $\hat{H}$  is the Hamiltonian.

In such a state, every  $M$ -body density matrix ( $1 \leq M \leq N$ ) is simply expressed as a function of the one-body density matrix  $\rho$  (see appendix C of Ref. [40]). Then, all the information on the system is contained in  $\rho$ . The expectation value of the Hamiltonian on the state  $|\phi\rangle$  may then be written as a functional of  $\rho$ :  $E[\rho] = \langle \phi | \hat{H} | \phi \rangle$ .

In addition, we have

$$\langle \phi | \frac{d}{dt} | \phi \rangle = \sum_{i=1}^N \langle \varphi_i | \frac{d}{dt} | \varphi_i \rangle \quad (\text{A.2})$$

and then

$$\begin{aligned} S &= \int_{t_0}^{t_1} dt \left( i\hbar \sum_{i=1}^N \langle \varphi_i | \frac{d}{dt} | \varphi_i \rangle - E[\rho(t)] \right) \\ &= \int_{t_0}^{t_1} dt \left( i\hbar \sum_{i=1}^N \int dx \varphi_i^*(x, t) \frac{d}{dt} \varphi_i(x, t) - E[\rho(t)] \right) \end{aligned} \quad (\text{A.3})$$

where  $x \equiv (\mathbf{r}s\tau)$  describes all the single-particle degrees of freedom (position  $\mathbf{r}$ , spin  $s$  and isospin  $\tau$ ). We introduced the notation  $\int dx = \sum_{\tau s} \int d\mathbf{r}$ .

The variational principle reads  $\delta S = 0$ . The variation must be done on each independent variable. Here, these variables are the real part  $\varphi_\alpha^{\text{Re}}$  and the imaginary part  $\varphi_\alpha^{\text{Im}}$  of each occupied single particle state  $\varphi_\alpha$ .

We must then consider

$$\frac{\delta S}{\delta \varphi_\alpha^{\text{Re}}(x, t)} = 0 \quad \text{and} \quad \frac{\delta S}{\delta \varphi_\alpha^{\text{Im}}(x, t)} = 0 \quad (\text{A.4})$$

for each  $\alpha \in \{1 \dots N\}$ , for all  $t$  such as  $t_0 \leq t \leq t_1$ , and for all  $x$ .

However, the calculation is more straightforward if we use  $\varphi_\alpha$  and  $\varphi_\alpha^*$  as *independent* variables instead of  $\varphi_\alpha^{\text{Re}}$  and  $\varphi_\alpha^{\text{Im}}$ . Indeed, noting

$$\frac{\delta}{\delta f^{\text{Re}}} = \frac{\delta}{\delta f} + \frac{\delta}{\delta f^*} \quad \text{et} \quad \frac{\delta}{\delta f^{\text{Im}}} = i \left( \frac{\delta}{\delta f} - \frac{\delta}{\delta f^*} \right), \quad (\text{A.5})$$

we see that the two choices are equivalent. We can then consider the variations over  $\varphi$  and over  $\varphi^*$  independently<sup>1</sup>.

Equations (A.4) become

$$\frac{\delta S}{\delta \varphi_\alpha(x, t)} = 0 \quad \text{and} \quad \frac{\delta S}{\delta \varphi_\alpha^*(x, t)} = 0. \quad (\text{A.6})$$

The variation over  $\varphi^*$  gives

$$\frac{\delta S}{\delta \varphi_\alpha^*(x, t)} = i\hbar \frac{d}{dt} \varphi_\alpha(x, t) - \int_{t_0}^{t_1} dt' \frac{\delta E[\rho(t')]}{\delta \varphi_\alpha^*(x, t)}. \quad (\text{A.7})$$

The functional derivative of  $E$  can be re-written thanks to a change of variable

$$\frac{\delta E[\rho(t')]}{\delta \varphi_\alpha^*(x, t)} = \int dy dy' \frac{\delta E[\rho(t')]}{\delta \rho(y, y'; t')} \frac{\delta \rho(y, y'; t')}{\delta \varphi_\alpha^*(x, t)}. \quad (\text{A.8})$$

Using

$$\frac{\delta \rho(y, y'; t')}{\delta \varphi_\alpha^*(x, t)} = \varphi_\alpha(y, t') \delta(y' - x) \delta(t - t') \quad (\text{A.9})$$

and noting the single-particle Hartree-Fock Hamiltonian  $h$  with matrix elements

$$h(x, y; t) = \frac{\delta E[\rho(t)]}{\delta \rho(y, x; t)}, \quad (\text{A.10})$$

we get the TDHF equation for the set of occupied states

$$\boxed{i\hbar \frac{d}{dt} \varphi_\alpha(x, t) = \int dy h(x, y; t) \varphi_\alpha(y, t)}. \quad (\text{A.11})$$

The variation over  $\varphi$  gives, after integrating by part the term with the time derivative,

$$\begin{aligned} \frac{\delta S}{\delta \varphi_\alpha(x, t)} = & \frac{\delta}{\delta \varphi_\alpha(x, t)} \int_{t_0}^{t_1} dt' \left[ i\hbar \frac{d}{dt'} \left( \sum_\beta \int dy \varphi_\beta^*(y, t') \varphi_\beta(y, t') \right) \right. \\ & \left. - i\hbar \sum_\beta \int dy \left( \frac{d}{dt'} \varphi_\beta^*(y, t') \right) \varphi_\beta(y, t') - E[\rho(t')] \right]. \quad (\text{A.12}) \end{aligned}$$

---

<sup>1</sup>Note that we loose the property " $\varphi^*$  being complex conjugated of  $\varphi$ " that we should restore later.

The first term in the r.h.s. cannot be replaced by  $\text{Tr}[\rho] = N$  because we considered  $\varphi$  and  $\varphi^*$  as independent variables. Let us note the variation of  $\varphi$  at a specific "point" of the Hilbert space at time  $t$

$$\delta_{\alpha x t} \varphi_{\beta}(y, t') = \Delta\varphi f(t) \delta(t - t') \delta(x - y) \delta_{\alpha\beta}. \quad (\text{A.13})$$

Using the definition of the functional derivative, we may write

$$\begin{aligned} & \frac{\delta}{\delta\varphi_{\alpha}(x, t)} \int_{t_0}^{t_1} dt' \frac{d}{dt'} \left( \sum_{\beta} \int dy \varphi_{\beta}^*(y, t') \varphi_{\beta}(y, t') \right) \\ &= \lim_{\Delta\varphi \rightarrow 0} \int_{t_0}^{t_1} dt' \frac{d}{dt'} \frac{1}{\Delta\varphi} \left( \sum_{\beta} \int dy \varphi_{\beta}^*(y, t') \delta_{\alpha x t} \varphi_{\beta}(y, t') \right) \\ &= [f(t) \delta(t - t') \varphi_{\alpha}^*(x, t')]_{t'=t_1}^{t_2}. \end{aligned} \quad (\text{A.14})$$

We have to choose  $f(t_1) = f(t_2) = 0$  in order to cancel this term at  $t = t_1$  or  $t = t_2$ . It is equivalent to forbid variations of  $\varphi$  at  $t_0$  and  $t_1$ . As a result, Eq. A.12 leads to the complex conjugated of the TDHF equation A.11, imposing that  $\varphi$  and  $\varphi^*$  are complex conjugated. This last property ensures energy and particle number conservations.

# Appendix B

## Galilean invariance of the TDHF equation

In this appendix, we study the conditions for the Galilean invariance of the TDHF equation 1.5. In particular, we study the link between momentum and velocity. We first revisit the Thouless and Valatin work [TV62] and show that a system in translational motion with a velocity  $v$  and a total momentum  $Ap$  is solution of the TDHF equation only if its density is constant in space *or* if  $p = mv$ . Then we study the particular case of a Skyrme EDF. Again, the TDHF equation, applied on a boosted Slater determinant, imposes the same unambiguous link between momentum and velocity.

### B.1 Revisiting the Thouless-Valatin demonstration

#### Notations

- We take  $\hbar = 1$ .
- $\tilde{f}$  : matrix in the  $r$ -space associated to the one-body operator  $\hat{f}$  with elements  $\tilde{f}(x, y) = \langle x | \hat{f} | y \rangle$
- We consider only scalar-isoscalar operators. Consequently spin and isospin degrees of freedom are implicit and omitted in the notation.
- we consider a 1D-problem.
- position matrix  $\tilde{x}$  with matrix elements  $\tilde{x}(x, y) = \delta(x - y) x$
- momentum matrix  $\tilde{p}$  with matrix elements  $\tilde{p}(x, y) = \delta(x - y) i dx$
- occupied single particle wave functions  $\varphi_\alpha(x) = \langle x | \alpha \rangle$
- density matrix  $\tilde{\rho}$  with matrix elements  $\tilde{\rho}(x, y) = \sum_\alpha \varphi_\alpha(x) \varphi_\alpha^*(y)$

## Galilean motion of a Hartree-Fock state

We want to describe a Hartree-Fock (HF) one-body density with a constant velocity  $v$ . The system is made of  $A$  nucleons of mass  $m$ .

### Momentum

The system has a constant momentum

$$\langle \hat{P} \rangle = \sum_{\alpha} \langle \alpha | \hat{p} | \alpha \rangle = Ap. \quad (\text{B.1})$$

We do not *a priori* make any link between  $p$  and  $v$ . We are looking for  $\tilde{\rho}_p$  such that

$$\text{Tr} (\tilde{\rho}_p \tilde{p}) = Ap. \quad (\text{B.2})$$

We start from the solution of the HF equation  $\tilde{\rho}_0$  for which  $\text{Tr} (\tilde{\rho}_0 \tilde{p}) = 0$ . The transformation to get the good momentum is obtained from a translation in momentum space

$$e^{ip\hat{x}} |p'\rangle = |p' + p\rangle. \quad (\text{B.3})$$

Applied on the HF static density matrix, this transformation leads to

$$\tilde{\rho}_p = e^{ip\hat{x}} \tilde{\rho}_0 e^{-ip\hat{x}}. \quad (\text{B.4})$$

We, indeed, get a system of momentum  $Ap$ :

$$\begin{aligned} \text{Tr} (\tilde{\rho}_p \tilde{p}) &= \text{Tr} (e^{ip\hat{x}} \tilde{\rho}_0 e^{-ip\hat{x}} \tilde{p}) \\ &= \text{Tr} (\tilde{\rho}_0 e^{-ip\hat{x}} \tilde{p} e^{ip\hat{x}}) \\ &= \text{Tr} (\tilde{\rho}_0 e^{-ip\hat{x}} (e^{ip\hat{x}} (\tilde{p} + p))) \\ &= \text{Tr} (\tilde{\rho}_0 \tilde{p}) + p \text{Tr} (\tilde{\rho}_0) \\ &= Ap. \end{aligned} \quad (\text{B.5})$$

### Velocity

We want a system of velocity  $v$ , so that at time  $t$ , the system at the initial time has been translated by  $vt$ . If we consider that, at  $t = 0$ , the density matrix is  $\tilde{\rho}_p$ , then its matrix elements must follow

$$\tilde{\rho}(x + vt, y + vt; t) = \tilde{\rho}(x, y; 0) = \tilde{\rho}_p(x, y)$$

or equivalently

$$\begin{aligned} \tilde{\rho}(x, y; t) &= \tilde{\rho}(x - vt, y - vt; 0) \\ &= \tilde{\rho}_p(x - vt, y - vt) \\ &= e^{ip(x-y)} \tilde{\rho}_0(x - vt, y - vt) \end{aligned} \quad (\text{B.6})$$

where we have used Eq. B.4 to express the matrix elements of  $\tilde{\rho}_p$  as function of those of  $\tilde{\rho}_0$ . A translation of  $-vt$  in coordinate space is given by the transformation

$$e^{ivt\hat{p}} |x\rangle = |x - vt\rangle. \quad (\text{B.7})$$

The density at time  $t$  is then reads

$$\begin{aligned} \tilde{\rho}(t) &= e^{-ivt\hat{p}} \tilde{\rho}_p e^{ivt\hat{p}} \\ &= e^{-ivt\hat{p}} e^{ip\hat{x}} \tilde{\rho}_0 e^{-ip\hat{x}} e^{ivt\hat{p}}. \end{aligned} \quad (\text{B.8})$$

## Is $\tilde{\rho}(t)$ a solution of the TDHF equation ?

We now verify if  $\tilde{\rho}(t)$  is a solution of the TDHF equation, and if yes, under what conditions. We first consider a problem involving a true Hamiltonian

$$\hat{H} = \hat{T} + \hat{V} \quad (\text{B.9})$$

as in the Thouless and Valatin original work. This implies that the interaction is not density dependent. In fact, this statement is not necessary, *i.e.* density dependent interactions like the Skyrme or the Gogny ones will give the same properties if one explicitly take into account the rearrangement term. However the expressions become much more complicated.

### Interaction

The two-body interaction  $\hat{V}_{12}$  is represented by a rank-2 antisymmetrized tensor in coordinate space  $\tilde{V}_{12}$  of matrix elements

$$\tilde{V}(x_1 x_2, y_1 y_2) = \langle x_1 x_2 | \hat{V}_{12} | y_1 y_2 \rangle - \langle x_1 x_2 | \hat{V}_{12} | y_2 y_1 \rangle. \quad (\text{B.10})$$

It is invariant by translation in coordinate space,

$$\tilde{V}(x_1+\lambda \ x_2+\lambda, y_1+\lambda \ y_2+\lambda) = \tilde{V}(x_1 x_2, y_1 y_2) \quad (\text{B.11})$$

and in momentum space (Galilean invariance),

$$\tilde{V}(x_1 x_2, y_1 y_2) \propto \delta(x_1 + x_2 - y_1 - y_2). \quad (\text{B.12})$$

### TDHF equation

TDHF is optimized to describe the evolution of one-body densities. We now verify if the density matrix expressed in Eq. B.8 is solution of the TDHF equation

$$i \frac{d}{dt} \tilde{\rho}(t) \stackrel{?}{=} [\tilde{h}[\tilde{\rho}(t)], \tilde{\rho}(t)] \quad (\text{B.13})$$

where the question mark indicates that the equality has to be demonstrated. The one-body HF Hamiltonian  $\tilde{h}$  is expressed by

$$\tilde{h}[\tilde{\rho}(t)] = \frac{\tilde{p}^2}{2m} + \tilde{U}[\tilde{\rho}(t)] \quad (\text{B.14})$$

where  $\tilde{U}$  is the self-consistent mean field

$$\tilde{U}_1[\tilde{\rho}(t)] = \text{Tr}_2 \left[ \tilde{V}_{12} \tilde{\rho}_2(t) \right]. \quad (\text{B.15})$$

Using the expression of  $\tilde{\rho}(t)$  (Eq. B.8), the left-hand side term of Eq. B.13 reads

$$i \frac{d}{dt} \tilde{\rho}(t) = v [\tilde{p}, \tilde{\rho}(t)]. \quad (\text{B.16})$$

The TDHF equation for  $\tilde{\rho}(t)$  then becomes

$$\left[ \frac{\tilde{p}^2}{2m} - v \tilde{p} + \tilde{U}[\tilde{\rho}(t)] \quad , \quad \tilde{\rho}(t) \right] \stackrel{?}{=} 0 \quad (\text{B.17})$$

We make the HF density  $\tilde{\rho}_0$  appear explicitly

$$\begin{aligned} & \left[ e^{-ip\tilde{x}} e^{ivt\tilde{p}} \left( \frac{\tilde{p}^2}{2m} - v \tilde{p} + \tilde{U}[\tilde{\rho}(t)] \right) e^{-ivt\tilde{p}} e^{ip\tilde{x}} \quad , \quad \tilde{\rho}_0 \right] \stackrel{?}{=} 0 \\ & \left[ e^{-ip\tilde{x}} \left( \frac{\tilde{p}^2}{2m} - v \tilde{p} \right) e^{ip\tilde{x}} + e^{-ip\tilde{x}} e^{ivt\tilde{p}} \tilde{U}[\tilde{\rho}(t)] e^{-ivt\tilde{p}} e^{ip\tilde{x}} \quad , \quad \tilde{\rho}_0 \right] \stackrel{?}{=} 0. \end{aligned} \quad (\text{B.18})$$

Using

$$e^{-ip\tilde{x}} \tilde{p} e^{ip\tilde{x}} = p + \tilde{p} \quad (\text{B.19})$$

and

$$e^{-ip\tilde{x}} \frac{\tilde{p}^2}{2m} e^{ip\tilde{x}} = \frac{(\tilde{p} + p)^2}{2m} \quad (\text{B.20})$$

we get

$$\left[ \frac{\tilde{p}^2}{2m} + \left( \frac{p}{m} - v \right) \tilde{p} + e^{-ip\tilde{x}} e^{ivt\tilde{p}} \tilde{U}[\tilde{\rho}(t)] e^{-ivt\tilde{p}} e^{ip\tilde{x}} , \tilde{\rho}_0 \right] = ? 0. \quad (\text{B.21})$$

Using the expression of the HF field in Eq. B.15, its matrix elements become

$$\begin{aligned} \tilde{U}[\tilde{\rho}(t)](x, x') &= \int dy dy' \tilde{V}(xy, x'y') \tilde{\rho}(y', y; t) \\ &= \int dy dy' \tilde{V}(xy, x'y') e^{ip(y'-y)} \tilde{\rho}_0(y'-vt, y-vt) \\ &= \int dy dy' \tilde{V}(xy, x'y') e^{ip(x-x')} \tilde{\rho}_0(y'-vt, y-vt). \end{aligned} \quad (\text{B.22})$$

We have used Eq. B.6 in the second line and the Galilean invariance (Eq. B.12) in the last line. The mean field part in Eq. B.21 becomes

$$\begin{aligned} \left( e^{-ip\tilde{x}} e^{ivt\tilde{p}} \tilde{U}[\tilde{\rho}(t)] e^{-ivt\tilde{p}} e^{ip\tilde{x}} \right) (x, x') &= e^{-ip(x-x')} \tilde{U}(x+vt, x'+vt) \\ &= \int dy dy' \tilde{V}(x+vt y, x'+vt y') \tilde{\rho}_0(y'-vt, y-vt) \\ &= \int dy dy' \tilde{V}(x y-vt, x' y'-vt) \tilde{\rho}_0(y'-vt, y-vt) \\ &= \int dy dy' \tilde{V}(xy, x'y') \tilde{\rho}_0(y', y) \\ &= \tilde{U}[\tilde{\rho}_0](x, x') \end{aligned} \quad (\text{B.23})$$

where we have used the translational invariance (Eq. B.11). Injecting the last relation in the commutator of Eq. B.21, we get

$$\begin{aligned} \left[ \frac{\tilde{p}^2}{2m} + \left( \frac{p}{m} - v \right) \tilde{p} + \tilde{U}[\tilde{\rho}_0] , \tilde{\rho}_0 \right] &= ? 0 \\ \left( \frac{p}{m} - v \right) [ \tilde{p} , \tilde{\rho}_0 ] &= ? 0 \end{aligned} \quad (\text{B.24})$$

where we have used the HF equation

$$\left[ \tilde{h}[\tilde{\rho}_0] , \tilde{\rho}_0 \right] = 0. \quad (\text{B.25})$$

Eq. B.24 is verified if  $\tilde{\rho}_0$  is a constant in the laboratory frame, or if the relation between momentum and velocity follows

$$p = mv. \quad (\text{B.26})$$

## B.2 Case of a full Skyrme field

### Notation

We now study a 3D problem and write  $\hbar$  explicitly. We will use isovector and vector operators, so the spin and isospin degrees of freedom are needed. However, when there is no ambiguity, the

spin and isospin indices, as well as the indice  $\alpha$  denoting single-particle states will be omitted in the notation for clarity. All operators in the HF Hamiltonian being isospin diagonal, the single-particle wave functions can be labeled with an isospin  $t_\alpha$ :

$$\varphi_\alpha(\mathbf{r}, s) = \langle \mathbf{r}, s, t_\alpha | \alpha \rangle. \quad (\text{B.27})$$

## Skyrme mean-field

In this section, we study the particular case of a Skyrme-HF field without time reversal symmetry, as it is used in the TDHF3D code [KOB97]. The action of this field on single-particle wave functions is given by [BFH87]

$$\begin{aligned} (\tilde{h}[\rho] \varphi_\alpha)(\mathbf{r}, s) = & \\ \sum_{s'} & \left[ \left( -\nabla \frac{\hbar^2}{2m_{t_\alpha}^*} \nabla + U_{t_\alpha}^R(\mathbf{r}) + i U_{t_\alpha}^I(\mathbf{r}) + i \mathbf{C}_{t_\alpha}(\mathbf{r}) \cdot \nabla \right) \delta_{ss'} \right. \\ & \left. + \mathbf{V}_{t_\alpha}(\mathbf{r}) \cdot \langle s | \boldsymbol{\sigma} | s' \rangle + i \mathbf{W}_{t_\alpha}(\mathbf{r}) \cdot (\langle s | \boldsymbol{\sigma} | s' \rangle \times \nabla) \right] \varphi_\alpha(\mathbf{r}, s'). \end{aligned}$$

The derivatives act on each term sitting on their right, including the wave function. All the fields (functions of  $\mathbf{r}$ ) are real.

## Galilean boost

Let us consider the transformation applied on the HF density (see Eq. B.4) which gives a momentum  $Ap$  to the system. Applied on the single particle wave functions, this transformation is nothing but a Galilean boost

$$\varphi(\mathbf{r}, s) = e^{ik\mathbf{r} \cdot \mathbf{u}_x} \varphi_0(\mathbf{r}, s) \quad (\text{B.28})$$

where  $k = p/\hbar$ .

We now look at how this boost transforms some local densities (the relevant ones for the next):

$$\rho(\mathbf{r}) = \sum_{\alpha s} \varphi_\alpha^*(\mathbf{r}, s) \varphi_\alpha(\mathbf{r}, s) \equiv \sum_{\alpha s} \varphi^* \varphi = \rho_0(\mathbf{r}) \quad (\text{B.29})$$

$$\mathbf{S}(\mathbf{r}) = \sum_{\alpha s s'} \varphi^*(\mathbf{r}, s) \varphi(\mathbf{r}, s') \langle s | \boldsymbol{\sigma} | s' \rangle = \mathbf{S}_0(\mathbf{r}) \quad (\text{B.30})$$

$$\mathbf{j}(\mathbf{r}) = \frac{1}{2i} \sum_{\alpha s} \varphi^* \nabla \varphi + c.c. = \mathbf{j}_0(\mathbf{r}) + k \rho_0(\mathbf{r}) \mathbf{u}_x \quad (\text{B.31})$$

where *c.c.* means "complex conjugated". Again, we look at the transformation of some parts of the field which are relevant for the next:

$$\frac{\hbar^2}{2m_t^*} = \frac{\hbar^2}{2m} + B_3 \rho + B_4 \rho_t = \frac{\hbar^2}{2m_{0_t}^*} \quad (\text{B.32})$$

$$\mathbf{W}_t = -B_9 \nabla (\rho + \rho_t) = \mathbf{W}_{0_t} \quad (\text{B.33})$$

$$\begin{aligned} \mathbf{C}_t &= 2B_3 \mathbf{j} + 2B_4 \mathbf{j}_t - B_9 \nabla \times (\mathbf{S} + \mathbf{S}_t) \\ &= \mathbf{C}_{0_t} + 2k \mathbf{u}_x (B_3 \rho_0 + B_4 \rho_{0_t}) \\ &= \mathbf{C}_{0_t} + \hbar^2 k \mathbf{u}_x \left( \frac{1}{m_t^*} - \frac{1}{m} \right) \end{aligned} \quad (\text{B.34})$$

$$\begin{aligned} U_t^I &= \nabla \cdot (B_3 \mathbf{j} + B_4 \mathbf{j}_t) \\ &= U_{0_t}^I + k \frac{\partial}{\partial x} (B_3 \rho_0 + B_4 \rho_{0_t}) \\ &= U_{0_t}^I + \frac{\hbar^2 k^2}{2} \frac{\partial}{\partial x} \frac{1}{m^*} \end{aligned} \quad (\text{B.35})$$

where the coefficients  $B_i$  are the usual Skyrme functional coefficients (combinations of the  $t_k$  and  $x_k$ ) [BFH87]. All the derivatives in the fields expressions act only inside their field.

## Velocity

The TDHF evolution of the single particle wave functions is given by a set of  $A$  non-linear Schrödinger equations

$$\frac{d}{dt} \varphi = -\frac{i}{\hbar} \tilde{h}[\tilde{\rho}(t)] \varphi. \quad (\text{B.36})$$

The position of the nucleus is given by

$$\begin{aligned} \langle \hat{X} \rangle &= \frac{1}{A} \sum_{\alpha=1}^A \langle \alpha | \hat{x} | \alpha \rangle \\ &= \frac{1}{A} \sum_{\alpha,s} \int d\mathbf{r} \ x \varphi^* \varphi. \end{aligned} \quad (\text{B.37})$$

The velocity of the nucleus is defined by

$$\frac{d}{dt} \langle \hat{X} \rangle = \frac{-i}{A\hbar} \sum_{\alpha,s} \int d\mathbf{r} \ x \varphi^* (\tilde{h} \varphi) + c.c.. \quad (\text{B.38})$$

Inserting Eq. B.28 into Eq. B.38 and noting that the real local part vanishes because of the *c.c.*, we get

$$\begin{aligned} \frac{d}{dt} \langle \hat{X} \rangle &= \frac{-i}{A\hbar} \sum_{\alpha,s} \int d\mathbf{r} \ x \varphi^* \left[ -\nabla \frac{\hbar^2}{2m^*} \nabla \varphi + i U^I \varphi + i \mathbf{C} \cdot \nabla \varphi \right. \\ &\quad \left. + \sum_{s'} i \mathbf{W} \cdot \langle s | \boldsymbol{\sigma} | s' \rangle \times \nabla \varphi(\mathbf{r}, s') \right] + c.c.. \end{aligned} \quad (\text{B.39})$$

We want to express this quantity at time  $t = 0$  just after the boost using the single particle wave functions of Eq. B.28. Using the transformation of the fields in Eqs. B.32, B.33 and B.34, we get

$$\begin{aligned} \frac{d}{dt} \langle \hat{X} \rangle &= \left( \frac{-i}{A\hbar} \sum_{\alpha,s} \int d\mathbf{r} \ x \varphi_0^* \left[ -\nabla \frac{\hbar^2}{2m^*} \nabla \varphi_0 + i U_0^I \varphi_0 + i \mathbf{C}_0 \cdot \nabla \varphi_0 \right. \right. \\ &\quad \left. \left. + \sum_{s'} i \mathbf{W} \cdot \langle s | \boldsymbol{\sigma} | s' \rangle \times \nabla \varphi_0(\mathbf{r}, s') \right] + c.c. \right) \\ &+ \left( \frac{-i}{A\hbar} \sum_{\alpha,s} \int d\mathbf{r} \ x \varphi_0^* \left[ \frac{\hbar^2 k^2}{2m^*} \varphi_0 - k \mathbf{C} \cdot \mathbf{u}_x \varphi_0 \right. \right. \\ &\quad \left. \left. - k \sum_{s'} \mathbf{W} \cdot \langle s | \boldsymbol{\sigma} | s' \rangle \times \mathbf{u}_x \varphi_0(\mathbf{r}, s') \right] + c.c. \right) \\ &+ \left( \frac{-i}{A\hbar} \sum_{\alpha,s} \int d\mathbf{r} \ x \varphi_0^* \left[ \frac{-ik\hbar^2}{2} \left( \frac{1}{m^*} \frac{\partial}{\partial x} + \frac{\partial}{\partial x} \frac{1}{m^*} \right) \varphi_0 \right. \right. \\ &\quad \left. \left. + \frac{ik\hbar^2}{2} \varphi_0 \frac{\partial}{\partial x} \frac{1}{m^*} + ik\hbar^2 \left( \frac{1}{m^*} - \frac{1}{m} \right) \frac{\partial}{\partial x} \varphi_0 \right] + c.c. \right). \end{aligned} \quad (\text{B.40})$$

The first term vanishes because it is the static HF velocity  $\frac{d}{dt}\langle\hat{X}\rangle_0 = 0$ . The second term vanishes because of the *c.c.*. Only the last term is left:

$$\begin{aligned}
\frac{d}{dt}\langle\hat{X}\rangle &= -\frac{\hbar k}{2A} \sum_{\alpha,s} \int d\mathbf{r} x \varphi_0^* \left[ \frac{1}{m^*} \frac{\partial}{\partial x} \varphi_0 + \frac{\partial}{\partial x} \frac{1}{m^*} \varphi_0 - \varphi_0 \frac{\partial}{\partial x} \frac{1}{m^*} \right. \\
&\quad \left. - 2 \left( \frac{1}{m^*} - \frac{1}{m} \right) \frac{\partial}{\partial x} \varphi_0 \right] + c.c. \\
&= -\frac{\hbar k}{Am} \sum_{\alpha,s} \int d\mathbf{r} x \left( \varphi_0^* \frac{\partial}{\partial x} \varphi_0 + \varphi_0 \frac{\partial}{\partial x} \varphi_0^* \right). \tag{B.41}
\end{aligned}$$

Using Integration by part on the first term in the bracket, we get

$$\begin{aligned}
\frac{d}{dt}\langle\hat{X}\rangle &= \frac{\hbar k}{Am} \sum_{\alpha,s} \int d\mathbf{r} \varphi_0^* \varphi_0 \\
&= \frac{p}{m}. \tag{B.42}
\end{aligned}$$

The condition of Eq. B.26 is then fulfilled.

# List of publications

- [1] B. Avez, Ph. Chomaz, T. Duguet, and C. Simenel. Pairing vibrations study using a time-dependent energy-density-functional approach. *Mod. Phys. Lett. A*, 25:1997, 2010.
- [2] B. Avez, A. Drouart, Ch. Stodel, and C. Simenel *et al.* Study of  $^{124}\text{Sn} + ^{136}\text{Xe}$  fusion-evaporation: analysis of a rare-event experiment. submitted, arXiv:1111.2913.
- [3] B. Avez and C. Simenel. Structure and direct decay of giant monopole resonances. submitted, arXiv:1105.5217.
- [4] B. Avez, C. Simenel, and Ph. Chomaz. Pairing vibrations study with the time-dependent hartree-fock-bogoliubov theory. *Phys. Rev. C*, 78:044318, 2008.
- [5] B. Avez, C. Simenel, and Ph. Chomaz. Pairing vibrations study from time-dependent hartree-fock-bogoliubov formalism. *Int. J. Mod. Phys. E*, 18:2103, 2009.
- [6] A. Chatillon *et al.* Spectroscopy of the odd transfermium  $^{251}\text{Md}$  and  $^{255}\text{Lr}$  nuclei using gamma, electron and alpha spectroscopy. In *International Symposium on Exotic Nuclei (EXON 2004)*, 2005.
- [7] A. Chatillon *et al.* Spectroscopy and single-particle structure of the odd-z heavy elements  $^{255}\text{Lr}$ ,  $^{251}\text{Md}$  and  $^{247}\text{Es}$ . *Eur. Phys. J. A*, 30:397, 2006.
- [8] A. Chatterjee *et al.*  $1n$  and  $2n$  transfer with the borromean nucleus  $^6\text{He}$  near the coulomb barrier. *Phys. Rev. Lett.*, 101:032701, 2008.
- [9] Ph. Chomaz and C. Simenel. Coupled collective motion in nuclear reactions. *Nucl. Phys. A*, 731:188, 2004.
- [10] F. Delaunay *et al.* Excited states of  $^{11}\text{Be}$  studied via the  $^{10}\text{Be}(d,p)^{11}\text{Be}$  reaction. In *41st International Winter Meeting on Nuclear Physics (BORMIO)*, 2003.

- [11] M. Evers, M. Dasgupta, D. J. Hinde, D. H. Luong, R. Rafiei, R. du Rietz, and C. Simenel. Cluster transfer in the reaction  $^{16}\text{O} + ^{208}\text{Pb}$  at energies well below the fusion barrier: A possible doorway to energy dissipation. *Phys. Rev. C*, 84:054614, 2011.
- [12] Evers, M., Dasgupta, M., Hinde, D.J., and Simenel, C. (multi-)nucleon transfer in the reactions  $^{16}\text{O}, ^{32}\text{S} + ^{208}\text{Pb}$ . *EPJ Web of Conferences*, 17:08003, 2011.
- [13] C. Golabek and C. Simenel. Collision dynamics of two  $^{238}\text{U}$  atomic nuclei. *Phys. Rev. Lett.*, 103:042701, 2009.
- [14] D. J. Hinde, R. du Rietz, C. Simenel, M. Dasgupta, A. Wakhle, M. Evers, and D. H. Luong. Effects of nuclear structure in heavy elements formation dynamics. *AIP Conf. Proc.*, 1423:65, 2012.
- [15] D. J. Hinde, R. du Rietz, R. G. Thomas, M. Dasgupta, C. Simenel, M. L. Brown, M. Evers, D. H. Luong, L. R. Gasques, R. Rafiei, and A. Wakhle. Investigation of the role of shell structure in quasi-fission mass distributions. submitted, arXiv:1111.4790.
- [16] G.W. Hitt *et al.* Development of a secondary triton beam from primary  $^{16,18}\text{O}$  beams for ( $t, ^3\text{He}$ ) experiments at intermediate energies. *Nucl. Instr. Meth. A*, 566:264, 2006.
- [17] M. E. Howard *et al.* Gamow-teller strengths in  $^{24}\text{Na}$  using the  $^{24}\text{Mg}(t, ^3\text{He})$  reaction at 115A MeV. *Phys. Rev. C*, 78:047302, 2008.
- [18] D.J. Kedziora and C. Simenel. New inverse quasifission mechanism to produce neutron-rich transfermium nuclei. *Phys. Rev. C*, 81:044613, 2010.
- [19] V. Lapoux *et al.* New resonant states in the exotic halo nucleus  $^6\text{He}$  below 6 MeV. To appear in *Phys. Lett. B*.
- [20] V. Lapoux *et al.* Resonances of  $^6\text{He}$  via the  $^8\text{He}(p, t)^6\text{He}$  reaction. In *12th International Conference on Nuclear Reaction Mechanisms, Italy*, 2009.
- [21] D. Lebhertz, S. Courtin, F. Haas, D. G. Jenkins, C. Simenel, M.-D. Salsac, D. A. Hutcheon, C. Beck, J. Cseh, J. Darai, C. Davis, R. G. Glover, A. Goasduff, P. E. Kent, G. Levai, P. L. Marley, A. Michalon, J. E. Pearson, M. Rousseau, N. Rowley, and C. Ruiz.  $^{12}\text{C}(^{16}\text{O}, \gamma)^{28}\text{Si}$  radiative capture: Structural and statistical aspects of the  $\gamma$  decay. *Phys. Rev. C*, 85:034333, Mar 2012.
- [22] A. Lemasson *et al.* Reactions with the double-borromean nucleus  $^8\text{He}$ . *Phys. Rev. C*, 82:044617, 2010.

- [23] A. Lemasson *et al.* Pair and single neutron transfer with borromean  $^8\text{He}$ . *Phys. Lett. B*, 697:454, 2011.
- [24] A. Navin, V. Tripathi, Y. Blumenfeld, V. Nanal, C. Simenel, J. M. Casandjian, G. de France, and R. Raabe *et al.* Direct and compound reactions induced by unstable helium beams near the coulomb barrier. *Phys. Rev. C*, 70:044601, 2004.
- [25] C. Simenel. *Dynamique Nucléaire autour de la Barrière : de la fusion à évaporation*. PhD thesis, University of Caen, 2003.
- [26] C. Simenel. Particle transfer reactions with the time-dependent hartree-fock theory using a particle number projection technique. *Phys. Rev. Lett.*, 105:192701, 2010.
- [27] C. Simenel. Particle-number fluctuations and correlations in transfer reactions obtained using the balian-vénéroni variational principle. *Phys. Rev. Lett.*, 106:112502, 2011.
- [28] C. Simenel and B. Avez. Time-dependent hartree-fock description of heavy-ion fusion. *Int. J. Mod. Phys. E*, 17:31, 2008.
- [29] C. Simenel, B. Avez, and C. Golabek. Microscopic description of heavy ion collisions around the barrier. Proceeding of the KERNZ08 conference, arXiv:0904.2653.
- [30] C. Simenel, M. Bender, Ph. Chomaz, T. Duguet, and G. de France. Quantum calculation of coulomb reorientation and near-barrier fusion. In *FUSION06*, volume 853. AIP Conf. Proc., 2006.
- [31] C. Simenel, M. Bender, Ph. Chomaz, T. Duguet, and G. de France. Quantum calculation of coulomb reorientation: Applications to near-barrier fusion. In *11th International Conference on Nuclear Reaction Mechanisms, Italy*, 2006.
- [32] C. Simenel and Ph. Chomaz. Nonlinear vibrations in nuclei. *Phys. Rev. C*, 68:024302, 2003.
- [33] C. Simenel and Ph. Chomaz. Couplings between dipole and quadrupole vibrations in tin isotopes. *Phys. Rev. C*, 80:064309, 2009.
- [34] C. Simenel, Ph. Chomaz, and G. de France. Quantum calculation of the dipole excitation in fusion reactions. *Phys. Rev. Lett.*, 86:2971, 2001.

- [35] C. Simenel, Ph. Chomaz, and G. de France. Quantum calculations of coulomb reorientation for sub-barrier fusion. *Phys. Rev. Lett.*, 93:102701, 2004.
- [36] C. Simenel, Ph. Chomaz, and G. de France. Fusion process studied with a preequilibrium giant dipole resonance in time-dependent hartree-fock theory. *Phys. Rev. C*, 76:024609, 2007.
- [37] C. Simenel, Ph. Chomaz, and T. Duguet. Isospin coupling in time-dependent-mean-field theories and decay of isovector excitations. arXiv:nucl-th/0504050.
- [38] C. Simenel, C. Golabek, and D. J. Kedziora. Actinide collisions for qed and superheavy elements with the time-dependent hartree-fock theory and the balian-v  roni variational principle. *EPJ Web of Conferences*, 17:09002, 2011.
- [39] C. Simenel, D. J. Hinde, R. du Rietz, M. Dasgupta, M. Evers, C. J. Lin, D. H. Luong, and A. Wakhle. Influence of entrance-channel magicity and isospin on quasi-fission. *Phys. Lett. B*, 710:607, 2012.
- [40] C. Simenel, D. Lacroix, and B. Avez. *Quantum Many-Body Dynamics: Applications to Nuclear Reactions*. VDM Verlag, Sarrebruck, Germany, 2010.
- [41] A. Wakhle, C. Simenel, D.J. Hinde, and M. Dasgupta. Microscopic quantum calculations of quasi-fission reactions. in preparation.
- [42] R. G. T. Zegers *et al.* Extraction of weak transition strengths via the ( $^3\text{He}$ ,  $t$ ) reaction at 420 MeV. *Phys. Rev. Lett.*, 99:202501, 2007.

# Bibliography

- [ABE98] T. Aumann, P. F. Bortignon, and H. Emling. Multiphonon giant resonances in nuclei. *Ann. Rev. Nucl. Part. Sci.*, 48:351, 1998.
- [AH08] E. Ackad and M. Horbatsch. Calculation of electron-positron production in supercritical uranium-uranium collisions near the Coulomb barrier. *Phys. Rev. A*, 78:062711, 2008.
- [AL09] M. Assie and D. Lacroix. Probing neutron correlations through nuclear breakup. *Phys. Rev. Lett.*, 102:202501, 2009.
- [Ari06] Y. Aritomo. Fusion hindrance and roles of shell effects in superheavy mass region. *Nucl. Phys. A*, 780:222, 2006.
- [Arm00] P. Armbruster. On the production of superheavy elements. *Ann. Rev. Nucl. Part. Sci.*, 50:411, 2000.
- [AS05] D. Almeded and P. D. Stevenson. Isovector giant monopole resonances in spherical nuclei. *J. Phys. G*, 31:S1819, 2005.
- [Ave09] B. Avez. *Mouvements Collectifs dans les Noyaux: des Vibrations à la Fusion*. PhD thesis, University of Paris XI, 2009.
- [AWL09] S. Ayik, K. Washiyama, and D. Lacroix. Fluctuation and dissipation dynamics in fusion reactions from a stochastic mean-field approach. *Phys. Rev. C*, 79:054606, 2009.
- [Ayi08] S. Ayik. A stochastic mean-field approach for nuclear dynamics. *Phys. Lett. B*, 658:174, 2008.
- [BABW90] J. F. Berger, J. D. Anderson, P. Bonche, and M. S. Weiss. Microscopic study of the  $^{238}\text{U}-^{238}\text{U}$  system and anomalous pair production. *Phys. Rev. C*, 41:R2483, 1990.
- [Bas77] R. Bass. Nucleus-nucleus potential deduced from experimental fusion cross sections. *Phys. Rev. Lett.*, 39:265, 1977.

- [Bas80] R. Bass. *Nuclear Reactions with Heavy-Ions*. Springer-Verlag, 1980.
- [BB66] D.R. Bès and R.A. Broglia. Pairing vibrations. *Nucl. Phys.*, 80:289, 1966.
- [BB10] A. Boudjemâa and M. Benarous. Variational self-consistent theory for trapped bose gases at finite temperature. *Eur. Phys. J. D*, 59:427, 2010.
- [BBB98] P. F. Bortignon, A. Bracco, and R. A. Broglia. *Giant Resonances: Nuclear Structure at Finite Temperature*. Harwood Academic Publishers, Amsterdam, 1998.
- [BBCDT01] V. Baran, D. M. Brink, M. Colonna, and M. Di Toro. Collective dipole bremsstrahlung in fusion reactions. *Phys. Rev. Lett.*, 87:182501, 2001.
- [BCS57] J. Bardeen, L. N. Cooper, and J. R. Schrieffer. Theory of superconductivity. *Phys. Rev.*, 108:1175, 1957.
- [BD97] P. F. Bortignon and C. H. Dasso. Anharmonic effects in the excitation of double-giant dipole modes in relativistic heavy-ion collisions. *Phys. Rev. C*, 56:574, 1997.
- [BF79] J. Blocki and H. Flocard. Calculations of giant resonances with time-dependent Hartree-Fock. *Phys. Lett. B*, 85:163, 1979.
- [BF85] P. Bonche and H. Flocard. Dispersion of one-body operators with the Balian-Vénéroni variational principle. *Nucl. Phys. A*, 437:189, 1985.
- [BF99] M. Benarous and H. Flocard. Time-dependent variational approach for boson systems. *Ann. Phys.*, 273:242, 1999.
- [BFH87] P. Bonche, H. Flocard, and P.H. Heenen. Self-consistent calculation of nuclear rotations: The complete yrast line of  $^{24}\text{Mg}$ . *Nucl. Phys. A*, 467:115, 1987.
- [BFH05] P. Bonche, H. Flocard, and P.H. Heenen. Solution of the Skyrme HF+BCS equation on a 3D mesh. *Comp. Phys. Com.*, 171:49, 2005.
- [BGK78] P. Bonche, B. Grammaticos, and S. Koonin. Three-dimensional time-dependent Hartree-Fock calculations of  $^{16}\text{O} + ^{16}\text{O}$  and  $^{40}\text{Ca} + ^{40}\text{Ca}$  fusion cross sections. *Phys. Rev. C*, 17:1700, 1978.
- [BK47] G. C. Baldwin and G. S. Klaiber. Photo-fission in heavy elements. *Phys. Rev.*, 71:3, 1947.

- [BKN76] P. Bonche, S. Koonin, and J. W. Negele. One-dimensional nuclear dynamics in the time-dependent Hartree-Fock approximation. *Phys. Rev. C*, 13:1226, 1976.
- [Bla54] J. S. Blair. Theory of elastic scattering of alpha particles by heavy nuclei. *Phys. Rev.*, 95:1218, 1954.
- [BLV84] P. Bonche, S. Levit, and D. Vautherin. Mean-field description of nuclei at high temperature. *Nucl. Phys. A*, 428:95, 1984.
- [BM75] A. Bohr and B.R. Mottelson. *Nuclear Structure*. 2 vol., W.A. Benjamin, Inc., 1975.
- [BN81] P. Bonche and N. Ngô. Time-dependent Hartree-Fock description of charge equilibration in heavy-ion collisions. *Phys. Lett. B*, 105:17, 1981.
- [Boc82] R. Bock *et al.* Dynamics of the fusion process. *Nucl. Phys. A*, 388:334, 1982.
- [BR81] J.P. Blaizot and G. Ripka. A variational principle for the calculation of transition amplitudes. *Phys. Lett. B*, 105:1, 1981.
- [BR86] J.-P. Blaizot and G. Ripka. *Quantum Theory of Finite Systems*. MIT Press, 1986.
- [Bro09] J. M. A. Broomfield. *Calculations of Mass Distributions using the Balian-Vénéroni Variational Approach*. PhD thesis, University of Surrey, 2009.
- [BRR<sup>+</sup>99] M. Bender, K. Rutz, P.-G. Reinhard, J. A. Maruhn, and W. Greiner. Shell structure of superheavy nuclei in self-consistent mean-field models. *Phys. Rev. C*, 60:034304, 1999.
- [BRST77] J. Blocki, J. Randrup, W.J. Swiatecki, and C.F. Tsang. Proximity forces. *Ann. Phys.*, 105:427, 1977.
- [BS08] J. M. A. Broomfield and P. D. Stevenson. Mass dispersions from giant dipole resonances using the Balian-Vénéroni variational approach. *J. Phys. G*, 35:095102, 2008.
- [BV81] R. Balian and M. Vénéroni. Time-dependent variational principle for predicting the expectation value of an observable. *Phys. Rev. Lett.*, 47:1353, 1981.

- [BV84] R. Balian and M. Vénéroni. Fluctuations in a time-dependent mean-field approach. *Phys. Lett. B*, 136:301, 1984.
- [BV85] R. Balian and M. Vénéroni. Time-dependent variational principle for the expectation value of an observable: Mean-field applications. *Ann. Phys.*, 164:334, 1985.
- [BV92] R. Balian and M. Vénéroni. Correlations and fluctuations in static and dynamic mean-field approaches. *Ann. Phys.*, 216:351, 1992.
- [BW91] R. A. Broglia and Aage Winther. *Heavy Ion Reactions: Lecture Notes the Elementary Processes (Frontiers in Physics)*. Addison Wesley Publishing Company, New-York, 1991.
- [CBH<sup>+</sup>98] E. Chabanat, P. Bonche, P. Haensel, J. Meyer, and R. Schaeffer. A Skyrme parametrization from subnuclear to neutron star densities Part II. nuclei far from stabilities. *Nucl. Phys. A*, 635:231, 1998.
- [CF95] Ph. Chomaz and N. Frascaria. Multiple phonon excitation in nuclei: experimental results and theoretical descriptions. *Phys. Rep.*, 252:275, 1995.
- [CGS87] Ph. Chomaz, N. V. Giai, and S. Stringari. Lifetimes of monopole resonances in time-dependent Hartree-Fock theory. *Phys. Lett. B*, 189:375, 1987.
- [Chi03] A. Yu. Chizhov *et al.* Unexpected entrance-channel effect in the fission of  $^{216}\text{Ra}^*$ . *Phys. Rev. C*, 67:011603, 2003.
- [CPS09] L. Corradi, G. Pollarolo, and S. Szilner. Multinucleon transfer processes in heavy-ion reactions. *J. Phys. G*, 36:113101, 2009.
- [CTS93] Ph. Chomaz, M. Di Toro, and A Smerzi. Pre-equilibrium effects on properties of hot giant dipole resonances. *Nucl. Phys. A*, 563:509, 1993.
- [CUS96] M. V. C. R. Chinn, A. S. Umar, and M. R. Strayer. Mean field studies of exotic nuclei. *Phys. Rep.*, 264:107, 1996.
- [DBD<sup>+</sup>11] J. Dvorak, M. Block, Ch.E. Düllmann, S. Heinz, R.-D. Herzberg, and M. Schädel. Iris: Exploring new frontiers in neutron-rich isotopes of the heaviest elements with a new inelastic reaction isotope separator. *Nucl. Instr. Meth. A*, 652:687, 2011.

- [DDP79] C. H. Dasso, T. Døssing, and H. C. Pauli. On the mass distribution in time-dependent Hartree-Fock calculations of heavy-ion collisions. *Z. Phys. A*, 289:395, 1979.
- [DHDT<sup>+</sup>07] M. Dasgupta, D. J. Hinde, A. Diaz-Torres, B. Bouriquet, Catherine I. Low, G. J. Milburn, and J. O. Newton. Beyond the coherent coupled channels description of nuclear fusion. *Phys. Rev. Lett.*, 99:192701, 2007.
- [DHJ03] D. J. Dean and M. Hjorth-Jensen. Pairing in nuclear systems: from neutron stars to finite nuclei. *Rev. Mod. Phys.*, 75:607, 2003.
- [DHRS98] M. Dasgupta, D. J. Hinde, N. Rowley, and A. M. Stefanini. Measuring barriers to fusion. *Ann. Rev. Nucl. Part. Sci.*, 48:401, 1998.
- [Dir30] P. A. M. Dirac. Note on exchange phenomena in the Thomas atom. *Proc. Camb. Phil. Soc.*, 26:376, 1930.
- [DMRKN78] K. T. R. Davies, V. Maruhn-Rezwani, S. E. Koonin, and J. W. Negele. Test of the time-dependent mean-field theory in kr-induced strongly damped collisions. *Phys. Rev. Lett.*, 41:632, 1978.
- [DNSW90] S. Drożdż, S. Nishizaki, J. Speth, and J. Wambach. The nuclear response within extended RPA theories. *Phys. Rep.*, 197:1, 1990.
- [dRHD<sup>+</sup>11] R. du Rietz, D. J. Hinde, M. Dasgupta, R. G. Thomas, L. R. Gasques, M. Evers, N. Lobanov, and A. Wakhle. Predominant time scales in fission processes in reactions of S, Ti and Ni with W: Zeptosecond versus attosecond. *Phys. Rev. Lett.*, 106:052701, 2011.
- [EBD<sup>+</sup>99] J. Engel, M. Bender, J. Dobaczewski, W. Nazarewicz, and R. Surman.  $\beta$  decay rates of r-process waiting-point nuclei in a self-consistent approach. *Phys. Rev. C*, 60:014302, 1999.
- [Eic07] R. Eichler *et al.* Chemical characterization of element 112. *Nature*, 447:72, 2007.
- [EJS10] H. Esbensen, C. L. Jiang, and A. M. Stefanini. Hindrance in the fusion of  $^{48}\text{Ca}+^{48}\text{Ca}$ . *Phys. Rev. C*, 82:054621, 2010.
- [ENI<sup>+</sup>10] S. Ebata, T. Nakatsukasa, T. Inakura, K. Yoshida, Y. Hashimoto, and K. Yabana. Canonical-basis time-dependent Hartree-Fock-Bogoliubov theory and linear-response calculations. *Phys. Rev. C*, 82:034306, 2010.

- [FC05] S. Fracasso and G. Colò. Fully self-consistent charge-exchange quasi-particle random-phase approximation and its application to isobaric analog resonances. *Phys. Rev. C*, 72:064310, 2005.
- [FCA<sup>+</sup>03] M. Fallot, Ph. Chomaz, M. V. Andrés, F. Catara, E. G. Lanza, and J. A. Scarpaci. Anharmonic vibrations in nuclei. *Nucl. Phys. A*, 729:699, 2003.
- [FGM<sup>+</sup>05] G. Fazio, G. Giardina, G. Mandaglio, R. Ruggeri, A. I. Muminov, A. K. Nasirov, Yu. Ts. Oganessian, A. G. Popeko, R. N. Sagaidak, A. V. Yeremin, S. Hofmann, F. Hanappe, and C. Stodel. Strong influence of the entrance channel on the formation of compound nuclei  $^{216,222}\text{Th}^*$  and their evaporation residues. *Phys. Rev. C*, 72:064614, 2005.
- [FHG<sup>+</sup>10] T. Furuta, K. H. O. Hasnaoui, F. Gulminelli, C. Leclercq, and A. Ono. Monopole oscillations in light nuclei with a molecular dynamics approach. *Phys. Rev. C*, 82:034307, 2010.
- [Fli96] S. Flibotte *et al.* Pre-equilibrium effects in the population of giant dipole resonances. *Phys. Rev. Lett.*, 77:1448, 1996.
- [Flo82] H. Flocard. In K. Goeke and P. G. Reinhard, editors, *Time-Dependent Hartree-Fock and Beyond*. Springer-Verlag, Berlin/New York, 1982.
- [FT72] S. Fukuda and Y. Torizuka. Giant multipole resonances in  $^{90}\text{Zr}$  observed by inelastic electron scattering. *Phys. Rev. Lett.*, 29:1109, 1972.
- [Gäg11] H. W. Gäggeler. Gas chemical properties of heaviest elements. *Radiochimica Acta*, 99:503, 2011.
- [GBC<sup>+</sup>07] L. R. Gasques, E. F. Brown, A. Chieffi, C. L. Jiang, M. Limongi, C. Rolfs, M. Wiescher, and D. G. Yakovlev. Implications of low-energy fusion hindrance on stellar burning and nucleosynthesis. *Phys. Rev. C*, 76:035802, 2007.
- [GLV] M. Grasso, D. Lacroix, and A. Vitturi. Pair-transfer probability in open- and closed-shell sn isotopes. submitted, arXiv:1202.2974.
- [GMR07] Lu Guo, J. A. Maruhn, and P.-G. Reinhard. Boost-invariant mean field approximation and the nuclear landau-zener effect. *Phys. Rev. C*, 76:014601, 2007.

- [GMRH08] Lu Guo, J. A. Maruhn, P.-G. Reinhard, and Y. Hashimoto. Conservation properties in the time-dependent Hartree Fock theory. *Phys. Rev. C*, 77:041301, 2008.
- [Gol09] C. Golabek. *A la recherche d'une signature de la formation et décroissance du système géant  $Z = 184$* . PhD thesis, University of Caen, 2009.
- [GT48] M. Goldhaber and E. Teller. On nuclear dipole vibrations. *Phys. Rev.*, 74:1046, 1948.
- [HD05] D.J. Hinde and M. Dasgupta. A new framework to investigate the systematics of fusion probabilities in heavy element formation: Application to Th isotopes. *Phys. Lett. B*, 622:23, 2005.
- [HDL<sup>+</sup>96] D. J. Hinde, M. Dasgupta, J. R. Leigh, J. C. Mein, C. R. Morton, J. O. Newton, and H. Timmers. Conclusive evidence for the influence of nuclear orientation on quasifission. *Phys. Rev. C*, 53:1290, 1996.
- [Heß97] F.P. Heßberger *et al.* Spontaneous fission and alpha-decay properties of neutron deficient isotopes  $^{257-253}104$  and  $^{258}106$ . *Z. Phys. A*, 359:415, 1997.
- [HHB12] V. Hellemans, P.-H. Heenen, and M. Bender. Tensor part of the Skyrme energy density functional. III. time-odd terms at high spin. *Phys. Rev. C*, 85:014326, 2012.
- [HM00] S. Hofmann and G. Münzenberg. The discovery of the heaviest elements. *Rev. Mod. Phys.*, 72:733, 2000.
- [HRK99] K. Hagino, N. Rowley, and A.T. Kruppa. A program for coupled-channel calculations with all order couplings for heavy-ion fusion reactions. *Comp. Phys. Com.*, 123:143, 1999.
- [HS01] K. Hagino and H. Sagawa. Continuum QRPA in the coordinate space representation. *Nucl. Phys. A*, 695:82, 2001.
- [HvdBI<sup>+</sup>77] M. N. Harakeh, K. van der Borg, T. Ishimatsu, H. P. Morsch, A. van der Woude, and F. E. Bertrand. Direct evidence for a new giant resonance at  $80A - 13$  MeV in the lead region. *Phys. Rev. Lett.*, 38:676, 1977.

- [HvdW01] M. N. Harakeh and A. van der Woude. *Giant Resonances: Fundamental High-Frequency Modes of Nuclear Excitations*. Oxford University Press, New York, 2001.
- [IM11] Y. Iwata and J. A. Maruhn. Enhanced spin-current tensor contribution in collision dynamics. *Phys. Rev. C*, 84:014616, 2011.
- [IOMI09] Y. Iwata, T. Otsuka, J. A. Maruhn, and N. Itagaki. Synthesis of exotic nuclei in heavy-ion collisions at higher energies. *Eur. Phys. J. A*, 42:613, 2009.
- [IOMI10a] Y. Iwata, T. Otsuka, J. A. Maruhn, and N. Itagaki. Suppression of charge equilibration leading to the synthesis of exotic nuclei. *Phys. Rev. Lett.*, 104:252501, 2010.
- [IOMI10b] Y. Iwata, T. Otsuka, J.A. Maruhn, and N. Itagaki. Geometric classification of nucleon transfer at moderate low-energies. *Nucl. Phys. A*, 836:108, 2010.
- [Itk11] I. M. Itkis *et al.* Fission and quasifission modes in heavy-ion-induced reactions leading to the formation of Hs\*. *Phys. Rev. C*, 83:064613, 2011.
- [JC02] O. Juillet and Ph. Chomaz. Exact stochastic mean-field approach to the fermionic many-body problem. *Phys. Rev. Lett.*, 88:142503, 2002.
- [Jia04] C. L. Jiang *et al.* Influence of nuclear structure on sub-barrier hindrance in Ni + Ni fusion. *Phys. Rev. Lett.*, 93:012701, 2004.
- [JZK<sup>+</sup>03] E. Joos, H. D. Zeh, C. Kiefer, D. Giulini, J. Kupsch, and I.-O. Stamatescu. *Decoherence and the appearance of a classical world in quantum theory*. second Ed., Springer, Berlin, 2003.
- [KBFS74] S. Krewald, J. Birkholz, Amand Faessler, and J. Speth. Continuum random-phase-approximation calculations of higher multipole giant resonances in <sup>16</sup>O and <sup>40</sup>Ca. *Phys. Rev. Lett.*, 33:1386, 1974.
- [KDMR<sup>+</sup>77] S. E. Koonin, K. T. R. Davies, V. Maruhn-Rezwani, H. Feldmeier, S. J. Krieger, and J. W. Negele. Time-dependent Hartree-Fock calculations for <sup>16</sup>O + <sup>16</sup>O and <sup>40</sup>Ca + <sup>40</sup>Ca reactions. *Phys. Rev. C*, 15:1359, 1977.
- [KLLT98] S. Kamerdzhiev, R. J. Liotta, E. Litvinova, and V. Tselyaev. Continuum quasiparticle random-phase approximation description of isovector E1 giant resonances. *Phys. Rev. C*, 58:172, 1998.

- [KOB97] K.-H. Kim, T. Otsuka, and P. Bonche. Three-dimensional TDHF calculations for reactions of unstable nuclei. *J. Phys. G*, 23:1267, 1997.
- [KSGVG02] E. Khan, N. Sandulescu, M. Grasso, and Nguyen Van Giai. Continuum quasiparticle random phase approximation and the time-dependent Hartree-Fock-Bogoliubov approach. *Phys. Rev. C*, 66:024309, 2002.
- [KSVG04] E. Khan, N. Sandulescu, Nguyen Van Giai, and M. Grasso. Two-neutron transfer in nuclei close to the drip line. *Phys. Rev. C*, 69:014314, 2004.
- [LAC01] D. Lacroix, S. Ayik, and Ph. Chomaz. Collective response of nuclei: Comparison between experiments and extended mean-field calculations. *Phys. Rev. C*, 63:064305, 2001.
- [LAC04] D. Lacroix, S. Ayik, and Ph. Chomaz. Nuclear collective vibrations in extended mean-field theory. *Prog. Part. Nucl. Phys.*, 52:497, 2004.
- [LBDM06] T. Lesinski, K. Bennaceur, T. Duguet, and J. Meyer. Isovector splitting of nucleon effective masses, *ab initio* benchmarks and extended stability criteria for Skyrme energy functionals. *Phys. Rev. C*, 74:044315, 2006.
- [LCA98] D. Lacroix, P. Chomaz, and S. Ayik. Finite temperature nuclear response in the extended random phase approximation. *Phys. Rev. C*, 58:2154, 1998.
- [LCA<sup>+</sup>06] E. G. Lanza, F. Catara, M. V. Andrés, Ph. Chomaz, M. Fallot, and J. A. Scarpaci. Microscopic calculations of double and triple giant resonance excitations in heavy ion collisions. *Phys. Rev. C*, 74:064614, 2006.
- [LCG<sup>+</sup>09] E. G. Lanza, F. Catara, D. Gambacurta, M. V. Andrés, and Ph. Chomaz. Multiphonon excitations and pygmy resonances in tin isotopes. *Phys. Rev. C*, 79:054615, 2009.
- [LDH<sup>+</sup>95] J. R. Leigh, M. Dasgupta, D. J. Hinde, J. C. Mein, C. R. Morton, R. C. Lemmon, J. P. Lestone, J. O. Newton, H. Timmers, J. X. Wei, and N. Rowley. Barrier distributions from the fusion of oxygen ions with  $^{144,148,154}\text{Sm}$  and  $^{186}\text{W}$ . *Phys. Rev. C*, 52:3151, 1995.

- [LdRH<sup>+</sup>12] C. J. Lin, R. du Rietz, D. J. Hinde, M. Dasgupta, R. G. Thomas, M. L. Brown, M. Evers, L. R. Gasques, and M. D. Rodriguez. Systematic behavior of mass distributions in <sup>48</sup>Ti-induced fission at near-barrier energies. *Phys. Rev. C*, 85:014611, 2012.
- [Lem09] A. Lemasson *et al.* Modern rutherford experiment: Tunneling of the most neutron-rich nucleus. *Phys. Rev. Lett.*, 103:232701, 2009.
- [LG76] K.F. Liu and Nguyen Van Giai. A self-consistent microscopic description of the giant resonances including the particle continuum. *Phys. Lett. B*, 65:23, 1976.
- [LMPPT11] K. Langanke, G. Martı́nez-Pinedo, I. Petermann, and F.K. Thielemann. Nuclear quests for supernova dynamics and nucleosynthesis. *Prog. Part. Nucl. Phys.*, 66:319, 2011.
- [LMR11] N. Loebl, J. A. Maruhn, and P.-G. Reinhard. Equilibration in the time-dependent Hartree-Fock approach probed with the Wigner distribution function. *Phys. Rev. C*, 84:034608, 2011.
- [LMvNC<sup>+</sup>00] D. Lacroix, A. Mai, P. von Neumann-Cosel, A. Richter, and J. Wambach. Multiple scales in the fine structure of the isoscalar giant quadrupole resonance in <sup>208</sup>Pb. *Phys. Lett. B*, 479:15, 2000.
- [Mar95] C. Martin. Variational approximation for two-time correlation functions in  $\phi^4$  theory: Optimization of the dynamics. *Phys. Rev. D*, 52:7121, 1995.
- [Mar99] C. Martin. Variational approximations for correlation functions in quantum field theories. *Ann. Phys.*, 278:202, 1999.
- [Mat01] M. Matsuo. Continuum linear response in coordinate space Hartree-Fock-Bogoliubov formalism for collective excitations in drip-line nuclei. *Nucl. Phys. A*, 696:371, 2001.
- [May50] M. Goeppert Mayer. Nuclear configurations in the spin-orbit coupling model. II. theoretical considerations. *Phys. Rev.*, 78:22, 1950.
- [MBD<sup>+</sup>99] C. R. Morton, A. C. Berriman, M. Dasgupta, D. J. Hinde, J. O. Newton, K. Hagino, and I. J. Thompson. Coupled-channels analysis of the <sup>16</sup>O+<sup>208</sup>Pb fusion barrier distribution. *Phys. Rev. C*, 60:044608, 1999.

- [MK85] J. B. Marston and S. E. Koonin. Mean-field calculations of fluctuations in nuclear collisions. *Phys. Rev. Lett.*, 54:1139, 1985.
- [Mor07] K. Morita *et al.* Experiment on synthesis of an isotope  $^{277}112$  by  $^{208}\text{Pb} + ^{70}\text{Zn}$  reaction. *J. Phys. Soc. Jap.*, 76:043201, 2007.
- [MRS<sup>+</sup>05] J. A. Maruhn, P. G. Reinhard, P. D. Stevenson, J. Rikovska Stone, and M. R. Strayer. Dipole giant resonances in deformed heavy nuclei. *Phys. Rev. C*, 71:064328, 2005.
- [MRSS06] J. A. Maruhn, P. G. Reinhard, P. D. Stevenson, and M. R. Strayer. Spin-excitation mechanisms in Skyrme-force time-dependent Hartree-Fock calculations. *Phys. Rev. C*, 74:027601, 2006.
- [MV91] C. Martin and D. Vautherin. A variational derivation of semiclassical mean-field evolution equations for a hot Fermi gas. *Phys. Lett. B*, 260:1, 1991.
- [MWC<sup>+</sup>76] N. Marty, A. Willis, V. Comparat, R. Frascaria, and M. Morlet. *Orsay report IPNO76-03*, 1976.
- [NCS<sup>+</sup>07] B. K. Nayak, R. K. Choudhury, A. Saxena, P. K. Sahu, R. G. Thomas, D. C. Biswas, B. V. John, E. T. Mirgule, Y. K. Gupta, M. Bhike, and H. G. Rajprakash. Evidence for Coulomb effects on the fusion barrier distribution for deformed projectile nuclei. *Phys. Rev. C*, 75:054615, 2007.
- [Neg82] J. W. Negele. The mean-field theory of nuclear structure and dynamics. *Rev. Mod. Phys.*, 54:913, 1982.
- [NMU<sup>+</sup>07] A. Nasirov, A. Muminov, R. Utamuratov, G. Fazio, G. Giardina, F. Hanappe, G. Mandaglio, M. Manganaro, and W. Scheid. Angular anisotropy of the fusion-fission and quasifission fragments. *Eur. Phys. J. A*, 34:325, 2007.
- [NY05] T. Nakatsukasa and K. Yabana. Linear response theory in the continuum for deformed nuclei: Green's function vs time-dependent Hartree-Fock with the absorbing boundary condition. *Phys. Rev. C*, 71:024301, 2005.
- [Oga06] Yu. Ts. Oganessian *et al.* Synthesis of the isotopes of elements 118 and 116 in the  $^{249}\text{Cf}$  and  $^{245}\text{Cm} + ^{48}\text{Ca}$  fusion reactions. *Phys. Rev. C*, 74:044602, 2006.

- [Oga09] Yu. Ts. Oganessian *et al.* Attempt to produce the isotopes of element 108 in the fusion reaction  $^{136}\text{Xe} + ^{136}\text{Xe}$ . *Phys. Rev. C*, 79:024608, 2009.
- [OUMR10] V. E. Oberacker, A. S. Umar, J. A. Maruhn, and P. G. Reinhard. Microscopic study of the  $^{132,124}\text{Sn} + ^{96}\text{Zr}$  reactions: Dynamic excitation energy, energy-dependent heavy-ion potential, and capture cross section. *Phys. Rev. C*, 82:034603, 2010.
- [PG08] S. Péru and H. Goutte. Role of deformation on giant resonances within the quasiparticle random-phase approximation and the Gogny force. *Phys. Rev. C*, 77:044313, 2008.
- [PGB<sup>+</sup>11] E. Plumbi, M. Grasso, D. Beaumel, E. Khan, J. Margueron, and J. van de Wiele. Probing the pairing interaction through two-neutron transfer reactions. *Phys. Rev. C*, 83:034613, 2011.
- [PMB88] J. M. Pacheco, E. Maglione, and R. A. Broglia. Time-dependent Hartree-Fock calculation of the escape width of the giant monopole resonance in  $^{16}\text{O}$ . *Phys. Rev. C*, 37:2257, 1988.
- [PN66] D. Pines and P. Nozieres. *The Theory of Quantum Liquids*. Benjamin, New York, 1966.
- [RCG83] P. G. Reinhard, R. Y. Cusson, and K. Goeke. Time evolution of coherent ground state correlations and the TDHF approach. *Nucl. Phys. A*, 398:141, 1983.
- [RDF<sup>+</sup>77] J. C. Roynette, H. Doubre, N. Frascaria, J. C. Jacmart, N. Poffé, and M. Riou. On the time scale of  $^{40}\text{Ca} + ^{40}\text{Ca}$  strongly damped reactions. *Phys. Lett. B*, 67:395, 1977.
- [RGM07] P. G. Reinhard, Lu Guo, and J. A. Maruhn. Nuclear giant resonances and linear response. *Eur. Phys. J. A*, 32:19, 2007.
- [RMG81] J. Reinhardt, B. Müller, and W. Greiner. Theory of positron production in heavy-ion collisions. *Phys. Rev. A*, 24:103, 1981.
- [RP69] G. Ripka and R. Padjen. Pairing vibrations of normal systems. *Nucl. Phys. A*, 132:489, 1969.
- [RS80] P. Ring and P. Schuck. *The Nuclear Many-Body Problem*. Springer Verlag, 1980.

- [RS92] P.-G Reinhard and E. Suraud. Stochastic TDHF and the Boltzman-Langevin equation. *Ann. Phys.*, 216:98, 1992.
- [RSA<sup>+</sup>06] P.-G. Reinhard, P. D. Stevenson, D. Almeded, J. A. Maruhn, and M. R. Strayer. Role of boundary conditions in dynamic studies of nuclear giant resonances and collisions. *Phys. Rev. E*, 73:036709, 2006.
- [RSS91] N. Rowley, G.R. Satchler, and P.H. Stelson. On the "distribution of barriers" interpretation of heavy-ion fusion. *Phys. Lett. B*, 254:25, 1991.
- [San97] R. Smolańczuk. Properties of the hypothetical spherical superheavy nuclei. *Phys. Rev. C*, 56:812, 1997.
- [SARM07] P.D. Stevenson, D. Almeded, P.-G. Reinhard, and J.A. Maruhn. Monopole giant resonances and TDHF boundary conditions. *Nucl. Phys. A*, 788:343, 2007.
- [SBMR11] I. Stetcu, A. Bulgac, P. Magierski, and K. J. Roche. Isovector giant dipole resonance from the 3D time-dependent density functional theory for superfluid nuclei. *Phys. Rev. C*, 84:051309, 2011.
- [Sca04] J.-A. Scarpaci. Multiphonon states built with giant resonances. *Nucl. Phys. A*, 731:175, 2004.
- [Sch82] M. Schädel *et al.* Actinide production in collisions of <sup>238</sup>U with <sup>248</sup>Cm. *Phys. Rev. Lett.*, 48:852, 1982.
- [SdlMF11] F. Sébille, V. de la Mota, and S. Figerou. Probing the microscopic nuclear matter self-organization processes in the neutron star crust. *Phys. Rev. C*, 84:055801, 2011.
- [SFdlM09] F. Sébille, S. Figerou, and V. de la Mota. Self-consistent dynamical mean-field investigation of exotic structures in isospin-asymmetric nuclear matter. *Nucl. Phys. A*, 822:51, 2009.
- [SGP85] M. Seiwert, W. Greiner, and W. T. Pinkston. Do heavy-ion potentials have pockets? *J. Phys. G*, 11:L21, 1985.
- [SGSG76] A. Sandulescu, R.K. Gupta, W. Scheid, and W. Greiner. Synthesis of new elements within the fragmentation theory: Application to  $Z = 104$  and  $106$  elements. *Phys. Lett. B*, 60:225, 1976.

- [She87] W. Q. Shen *et al.* Fission and quasifission in U-induced reactions. *Phys. Rev. C*, 36:115, 1987.
- [Sky56] T. Skyrme. The nuclear surface. *Phil. Mag.*, 1:1043, 1956.
- [SLBW] G. Scamps, D. Lacroix, G. F. Bertsch, and K. Washiyama. Pairing dynamics in particle transport. submitted, arXiv:1202.2681.
- [SM11] H. Shimoyama and M. Matsuo. Anomalous pairing vibration in neutron-rich sn isotopes beyond the  $N = 82$  magic number. *Phys. Rev. C*, 84:044317, 2011.
- [SPS89] E. Suraud, M. Pi, and P. Schuck. Giant dipole modes in heavy-ion reactions. *Nucl. Phys. A*, 492:294, 1989.
- [SSRSN04] P. D. Stevenson, M. R. Strayer, J. Rikovska Stone, and W. G. Newton. Giant resonances from TDHF. *Int. J. Mod. Phys. E*, 13:181, 2004.
- [Sto98] Ch. Stodel. *Experimental study of the influence of the structure of partners in the fusion of nearly symmetric systems*. PhD thesis, University of Caen, 1998.
- [SV79] S. Stringari and D. Vautherin. Damping of monopole vibrations in time-dependent Hartree-Fock theory. *Phys. Lett. B*, 88:1, 1979.
- [Swi82] W.J. Swiatecki. The dynamics of the fusion of two nuclei. *Nucl. Phys. A*, 376:275, 1982.
- [TNLS89] I.J. Thompson, M.A. Nagarajan, J.S. Lilley, and M.J. Smithson. The threshold anomaly in  $^{16}\text{O} + ^{208}\text{Pb}$  scattering. *Nucl. Phys. A*, 505:84, 1989.
- [Toh01] M. Tohyama. Collectivity of double giant resonances in extended RPA theories. *Phys. Rev. C*, 64:067304, 2001.
- [Tök85] J. Töke *et al.* Quasi-fission : The mass-drift mode in heavy-ion reactions. *Nucl. Phys. A*, 440:327, 1985.
- [TU02] M. Tohyama and A. S. Umar. Quadrupole resonances in unstable oxygen isotopes in time-dependent density-matrix formalism. *Phys. Lett. B*, 549:72, 2002.
- [TV62] D.J. Thouless and J.G. Valatin. Time-dependent Hartree-Fock equations and rotational states of nuclei. *Nucl. Phys.*, 31:211, 1962.

- [TV85] T. Troudet and D. Vautherin. Mass dispersion through particle emission from a vibrating nucleus. *Phys. Rev. C*, 31:278, 1985.
- [UMIO10] A. S. Umar, J. A. Maruhn, N. Itagaki, and V. E. Oberacker. Microscopic study of the triple- $\alpha$  reaction. *Phys. Rev. Lett.*, 104:212503, 2010.
- [UO05] A. S. Umar and V. E. Oberacker. Time-dependent response calculations of nuclear resonances. *Phys. Rev. C*, 71:034314, 2005.
- [UO06a] A. S. Umar and V. E. Oberacker. Dynamical deformation effects in subbarrier fusion of  $^{64}\text{Ni} + ^{132}\text{Sn}$ . *Phys. Rev. C*, 74:061601, 2006.
- [UO06b] A. S. Umar and V. E. Oberacker. Heavy-ion interaction potential deduced from density-constrained time-dependent Hartree-Fock calculation. *Phys. Rev. C*, 74:021601, 2006.
- [UO06c] A. S. Umar and V. E. Oberacker. Three-dimensional unrestricted time-dependent Hartree-Fock fusion calculations using the full Skyrme interaction. *Phys. Rev. C*, 73:054607, 2006.
- [UO06d] A. S. Umar and V. E. Oberacker. Time dependent Hartree-Fock fusion calculations for spherical, deformed systems. *Phys. Rev. C*, 74:024606, 2006.
- [UO07] A. S. Umar and V. E. Oberacker.  $^{64}\text{Ni} + ^{132}\text{Sn}$  fusion within the density-constrained time-dependent Hartree-Fock formalism. *Phys. Rev. C*, 76:014614, 2007.
- [UO08] A. S. Umar and V. E. Oberacker.  $^{64}\text{Ni} + ^{64}\text{Ni}$  fusion reaction calculated with the density-constrained time-dependent Hartree-Fock formalism. *Phys. Rev. C*, 77:064605, 2008.
- [UO09a] A. Umar and V. Oberacker. Density-constrained time-dependent Hartree-Fock calculation of  $^{16}\text{O} + ^{208}\text{Pb}$  fusion cross-sections. *Eur. Phys. J. A*, 39:243, 2009.
- [UO09b] A. S. Umar and V. E. Oberacker. Center-of-mass motion and cross-channel coupling in the time-dependent Hartree-Fock theory. *J. Phys. G*, 36:025101, 2009.
- [UOM08] A. Umar, V. Oberacker, and J. Maruhn. Neutron transfer dynamics and doorway to fusion in time-dependent Hartree-Fock theory. *Eur. Phys. J. A*, 37:245–250, 2008.

- [UOMR09] A. S. Umar, V. E. Oberacker, J. A. Maruhn, and P. G. Reinhard. Microscopic calculation of precompound excitation energies for heavy-ion collisions. *Phys. Rev. C*, 80:041601, 2009.
- [UOMR10] A. S. Umar, V. E. Oberacker, J. A. Maruhn, and P. G. Reinhard. Entrance channel dynamics of hot and cold fusion reactions leading to superheavy elements. *Phys. Rev. C*, 81:064607, 2010.
- [UOMR12] A. S. Umar, V. E. Oberacker, J. A. Maruhn, and P.-G. Reinhard. Microscopic composition of ion-ion interaction potentials. *Phys. Rev. C*, 85:017602, Jan 2012.
- [USR86] A. S. Umar, M. R. Strayer, and P. G. Reinhard. Resolution of the fusion window anomaly in heavy-ion collisions. *Phys. Rev. Lett.*, 56:2793, 1986.
- [VCC<sup>+</sup>95] C. Volpe, F. Catara, Ph. Chomaz, M. V. Andrés, and E. G. Lanza. Anharmonicities and non-linearities in the excitation of double giant resonances. *Nucl. Phys. A*, 589:521, 1995.
- [VGG<sup>+</sup>77] F. Videbæk, R. B. Goldstein, L. Grodzins, S. G. Steadman, T. A. Belote, and J. D. Garrett. Elastic scattering, transfer reactions, and fission induced by  $^{16}\text{O}$  ions on  $^{181}\text{Ta}$  and  $^{208}\text{Pb}$ . *Phys. Rev. C*, 15:954, 1977.
- [VHB00] A. Valor, P.-H. Heenen, and P. Bonche. Configuration mixing of mean-field wave functions projected on angular momentum and particle number: Application to  $^{24}\text{Mg}$ . *Nucl. Phys. A*, 671:145, 2000.
- [VKW85] V. E. Viola, K. Kwiatkowski, and M. Walker. Systematics of fission fragment total kinetic energy release. *Phys. Rev. C*, 31:1550, 1985.
- [Vol78] V. V. Volkov. Deep inelastic transfer reactions – the new type of reactions between complex nuclei. *Phys. Rep.*, 44:93, 1978.
- [VTV87] D. Vautherin, J. Treiner, and M. Vénéroni. Evolution of hot compressed nuclei in the time-dependent Hartree-Fock approximation. *Phys. Lett. B*, 191:6, 1987.
- [WAL09] K. Washiyama, S. Ayik, and D. Lacroix. Mass dispersion in transfer reactions with a stochastic mean-field theory. *Phys. Rev. C*, 80:031602, 2009.

- [WC85] S. J. Wang and W. Cassing. Explicit treatment of  $N$ -body correlations within a density-matrix formalism. *Ann. Phys.*, 159:328, 1985.
- [WL08] K. Washiyama and D. Lacroix. Energy dependence of the nucleus-nucleus potential close to the Coulomb barrier. *Phys. Rev. C*, 78:024610, 2008.
- [WL09] K. Washiyama and D. Lacroix. Energy dissipation in fusion reactions from dynamical mean-field theory. *Int. J. Mod. Phys. E*, 18:2114, 2009.
- [Won73] C. Y. Wong. Interaction barrier in charged-particle nuclear reactions. *Phys. Rev. Lett.*, 31:766, 1973.
- [YALW11] B. Yilmaz, S. Ayik, D. Lacroix, and K. Washiyama. Nucleon exchange mechanism in heavy-ion collisions at near-barrier energies. *Phys. Rev. C*, 83:064615, 2011.
- [YLC<sup>+</sup>04] D. H. Youngblood, Y.-W. Lui, H. L. Clark, B. John, Y. Tokimoto, and X. Chen. Isoscalar  $e0$ - $e3$  strength in  $^{116}\text{Sn}$ ,  $^{144}\text{Sm}$ ,  $^{154}\text{Sm}$ , and  $^{208}\text{Pb}$ . *Phys. Rev. C*, 69:034315, 2004.
- [YRM<sup>+</sup>77] D. H. Youngblood, C. M. Rozsa, J. M. Moss, D. R. Brown, and J. D. Bronson. Isoscalar breathing-mode state in  $^{144}\text{Sm}$  and  $^{208}\text{Pb}$ . *Phys. Rev. Lett.*, 39:1188, 1977.
- [ZOIG06] V. I. Zagrebaev, Yu. Ts. Oganessian, M. G. Itkis, and Walter Greiner. Superheavy nuclei and quasi-atoms produced in collisions of transuranium ions. *Phys. Rev. C*, 73:031602, 2006.
- [ZPG88] M. Zielinska-Pfabé and C. Grégoire. Dispersions in semiclassical dynamics. *Phys. Rev. C*, 37:2594, 1988.